AD674644

USAAVLABS TECHNICAL REPORT 68-52

INVESTIGATION OF THE DOWNWASH ENVIRONMENT GENERATED BY V/STOL AIRCRAFT OPERATING IN GROUND EFFECT

By

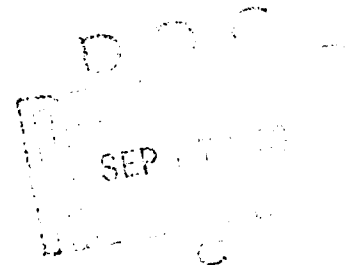M. George

E. Kisielowski

D. S. Douglas

July 1968

U. S. ARMY AVIATION MATERIEL LABORATORIES
FORT EUSTIS, VIRGINIA

Disclaimers

DEPARTMENT OF THE ARMY
U. S. ARMY AVIATION MATERIEL LABORATORIES
FORT EUSTIS, VIRGINIA 23604

This report was prepared by the Dynasciences Corporation under the terms of Contract DA 44-177-AMC-316(T). It reports on the work concluded in an investigation of the dust cloud generated by several types of VTOL aircraft when hovering over a specified terrain.

The results of the analytical investigation were compared with experimental results gathered under Contract DA 44-177-AMC-289(T) and with a series of tests conducted by Dynasciences in conjunction with the above program.

This command concurs in the conclusions and recommendations presented herein.

INVESTIGATION OF THE DOWNWASH ENVIRONMENT GENERATED BY V/STOL AIRCRAFT OPERATING IN GROUND EFFECT

Dynasciences Corporation Report DCR-275

By

M. George
E. Kisielowski
D.S. Douglas

Prepared by

Dynasciences Corporation
Blue Bell, Pennsylvania

for

U. S. ARMY AVIATION MATERIEL LABORATORIES
FORT EUSTIS, VIRGINIA

SUMMARY

Analytical methods are developed for determining the down-
wash environment generated by multirotor/propeller V/STOL
aircraft configurations operating in ground proximity.

These methods are utilized to compute rotor flow field and
contaminant dust cloud characteristics (including particle
density and size distributions) for the H-21, XC-142, X-22A,
X-19A, and XV-5A aircraft. The effects of the contaminated
atmosphere on pilot's visibility, ground equipment, and
personnel are also determined for these aircraft.

The theoretically predicted results are generally in good
agreement with the limited test data. Additional full-scale
test data are required to verify further the assumptions
inherent in the theory.

FOREWORD

This report presents the results of an investigation of the downwash environment generated by V/STOL aircraft operating in ground proximity.

The work was performed by the Dynasciences Corporation, Blue Bell, Pennsylvania, for the U. S. Army Aviation Materiel Laboratories (USAAVLABS). Fort Eustis, Virginia, under Contract DA 44-177-AMC-316(T) during the period from August 1965 through March 1968.

The Army technical representative was Mr. Joel Terry, who was assisted by Mr. Blair Poteate and Mr. G. William Hogg. The contributions of the Army personnel to this work are gratefully acknowledged.

The following Dynasciences Corporation personnel participated in this program:

    Mr. M. George - Project Engineer
    Mr. D. S. Douglas - Aeronautical Engineer
    Mr. J. Tang - Aeronautical Engineer
    Mr. S. Mills - Sr. Aeronautical Engineer
    Mr. E. Kisielowski - Manager, Aeronautics
    Dr. A. A. Perlmutter - Senior Vice President

v

CONTENTS

LIST OF ILLUSTRATIONS

x

LIST OF TABLES

SYMBOLS

A.a.B   constants as defined in the text

A_p particle cross-sectional area. $\frac{\pi}{4} D_p^2$. ft^2

C   contrast between sight of object and its background

$C_u \cdot C_y$ wall jet constants

C_1, C_2 constants as defined in text

C_T rotor thrust coefficient out of ground effect

D   diameter of rotor. ft

D_e effective rotor diameter of the contracted slipstream. ft

D_p particle diameter. mm or micron

$\overline{D_p}$ mean particle diameter. mm or microns

D_{p+} mean partic diameter. percent finer by weight

D_S diameter of standard 0.25 mm size particle, mm

D_{pw} max water particle diameter (.50 mm)

D.L.   disc loading. lb/ft^2

d   cloud penetration distance along pilot's line of vision. ft

e_A percent finer by weight of airborne particles of size A

e_G	percent finer by weight of ground particles of size A
$(e_G)_{max}$	percent finer by weight of ground particles of size A_{max}
F_h	correction factor as defined in the text
H	rotor height above the ground, ft
H_c	height of dust cloud, ft
H_w	aircraft wheel height from the ground, ft
h	vertical distance measured from rotor plane, ft
h_o	wall jet height ($u = 0.01\ u_m$), ft
I_o	background light intensity, foot-lambert
I_s	object light intensity, foot-lambert
K	logarithmic constant as defined in the text
k_t	terrain erosion factor
k_g	ground effect factor
X_L, Y_L	half-distance between rotor, along the X or Y axis, ft
ℓ, ϕ	polar coordinates located at the center of vortex spiral
ℓ_v	vertical location of dust cloud boundary from the center of vortex spiral
m	particle mass flow rate per unit area, lb/sec-ft^2
m_o	particle mass flow rate per unit area along the ground, lb/sec-ft^2

xvi

$\dot{m}$ particle mass flow rate per unit width, lb/sec-ft

N number of particles per cubic ft of air

q_N dynamic pressure of a fully developed slipstream, $= \frac{1}{2} \rho U_N^2$, lb/ft^2

q_s surface dynamic pressure along the ground, lb/ft^2

$(q_s)_{eff}$ effective surface dynamic pressure along the ground, lb/ft^2

$q_{s max}$ maximum surface dynamic pressure along the ground, $\frac{1}{2} \rho (U_s)^2_{max}$, lb/ft^2

R rotor radius, ft

R_c radius of dust cloud, ft

R_V radius of vortex spiral in dust cloud, ft

r radial location, ft

S_h horizontal component of distance between pilot and object along pilot's line of sight, ft

S distance from pilot to object along pilot's line of sight, ft

T light transmittance

T_f velocity interference correction factor

t axial distance from jet nozzle exit, ft

u local velocity within the wall jet, ft/sec

$\bar{U}$ average induced velocity at the rotor disc in ground effect, ft/sec

$\bar{U}_M$	mean momentum velocity at the jet nozzle exit, ft/sec
u_m	maximum velocity within the wall jet, ft/sec
U_W	velocity of fully developed slipstream, ft/sec
U_o	momentum value of induced velocity at the rotor disc, ft/sec
U_r	radial velocity component, ft/sec
$(U_s)_{max}$	maximum surface velocity along the ground, ft/sec
U_X	longitudinal velocity component along X axis, ft/sec
U_Y	lateral velocity component along Y axis, ft/sec
U_Z	axial velocity component, ft/sec
U_{IGE}	induced velocity in ground effect, ft/sec
U_{OGE}	induced velocity out of ground effect, ft/sec
v	velocity along a stream tube, ft/sec
v_*	drag velocity as defined in the text, ft/sec
X, Y, Z	right angled coordinate system with origin on the ground
y	height within the wall jet, ft
$\eta_{\frac{1}{2}}$	height within the wall jet where $u/u_m = \frac{1}{2}$, ft
z_v	vertical distance above the ground to vortex spiral center, ft
α, β, γ	angles as defined in the text, degrees
θ	flow angle in the interaction plane, degrees
ρ	air density, slugs/cu ft

ρ_p particle density, lb/cu ft of air

ρ_{pw} water particle density, lb/cu ft

σ rotor solidity, b_c/H_R

τ shearing force or drag per square cm

ϕ polar angle within vortex spiral

ϕ_0 constant as defined in the text

ψ aircraft heading angle relative to sighted object, degrees

I. INTRODUCTION

The downwash environment problems associated with V/STOL aircraft operating in ground proximity have become greatly magnified by the new generation of high-disc-loading multi-lift V/STOL aircraft. Due to the complexity of the flow mechanism in the vicinity of a lifting rotor operating in ground effect, formulation of an exact mathematical model for rotor downwash environment is indeed very difficult. For this reason, the previous work on the subject is limited to extremely specialized analyses covering only a very narrow portion of overall rotor downwash problems. The test information in this field consists of uncoordinated small-scale or full-scale model data without proper definition of pertinent test parameters. Consequently, there exists a need for a simple and reliable analytical method supplemented by test data which can be readily applied for predicting downwash environment of various V/STOL configurations operating in ground proximity.

The objective of this program is to develop a relatively simple mathematical model to predict the relationship which exists between V/STOL lift devices and their orientation on the aircraft as they relate to the generation of the contaminated atmosphere surrounding hovering aircraft. This model is utilized to compute contaminant cloud size and shape, particle density and size distributions within the dust cloud, and the effects of the contaminant atmosphere on pilot's visibility, ground equipment, and personnel.

This mathematical model is based on the available rotor downwash theory for the flow regions where it is considered to be most applicable, on the limited test data for the flow regions where the theory is not considered to be applicable, and on the semiempirical methods for the flow regions where both the available theory and the test data are practically non-existent.

Section II of this report presents the details of the mathematical model developed under this program.

Section III contains the computed results of the contaminant downwash environment for the H-21, XC-142, X-22A, X-19A, and XV-5A aircraft operating in ground effect. Some test data on ground surface mass flow rates obtained during this program for the H-21 helicopter are presented in the appendix. The theory developed herein is correlated with the available test data wherever possible.

II. THEORETICAL ANALYSIS

The downwash signature of a V/STOL aircraft operating over
unprepared landing surfaces is defined as the resultant
operational environment that the aircraft generates less
the natural environment existing prior to the aircraft's
arrival. The downwash signature can be determined by first
defining the flow field in the vicinity of the aircraft
hovering in ground effect and then by determining the
resulting dust cloud size and content associated with this
flow field.

A. FLOW FIELD

The analytical treatment of the flow field in the vicinity
of a lifting rotor in ground effect is a formidable task.
Several investigators have attempted to formulate analyses
for this purpose. However, as indicated in Reference 1,
these analyses are considered to be inadequate. More
rigorous computer methods have recently been developed to
better define the flow mechanism during ground impingement
of uniform jets. However, these methods could not be applied
to the present program.

For this program, existing analyses and experimental data
such as those of Reference 2 were applied to the regions of
the downwash flow field where they were considered to be
most suitable.

An artist's conception of the flow field in the vicinity of
a typical two-rotor/propeller V/STOL aircraft hovering in
ground effect is shown in Figure 1.

In order to facilitate the analysis, the flow field of a
two-propeller/rotor configuration represented in Figure 1
is subdivided into a number of isolated flow regions as
shown in Figure 2. The flow field in each of these regions
is as follows.

3
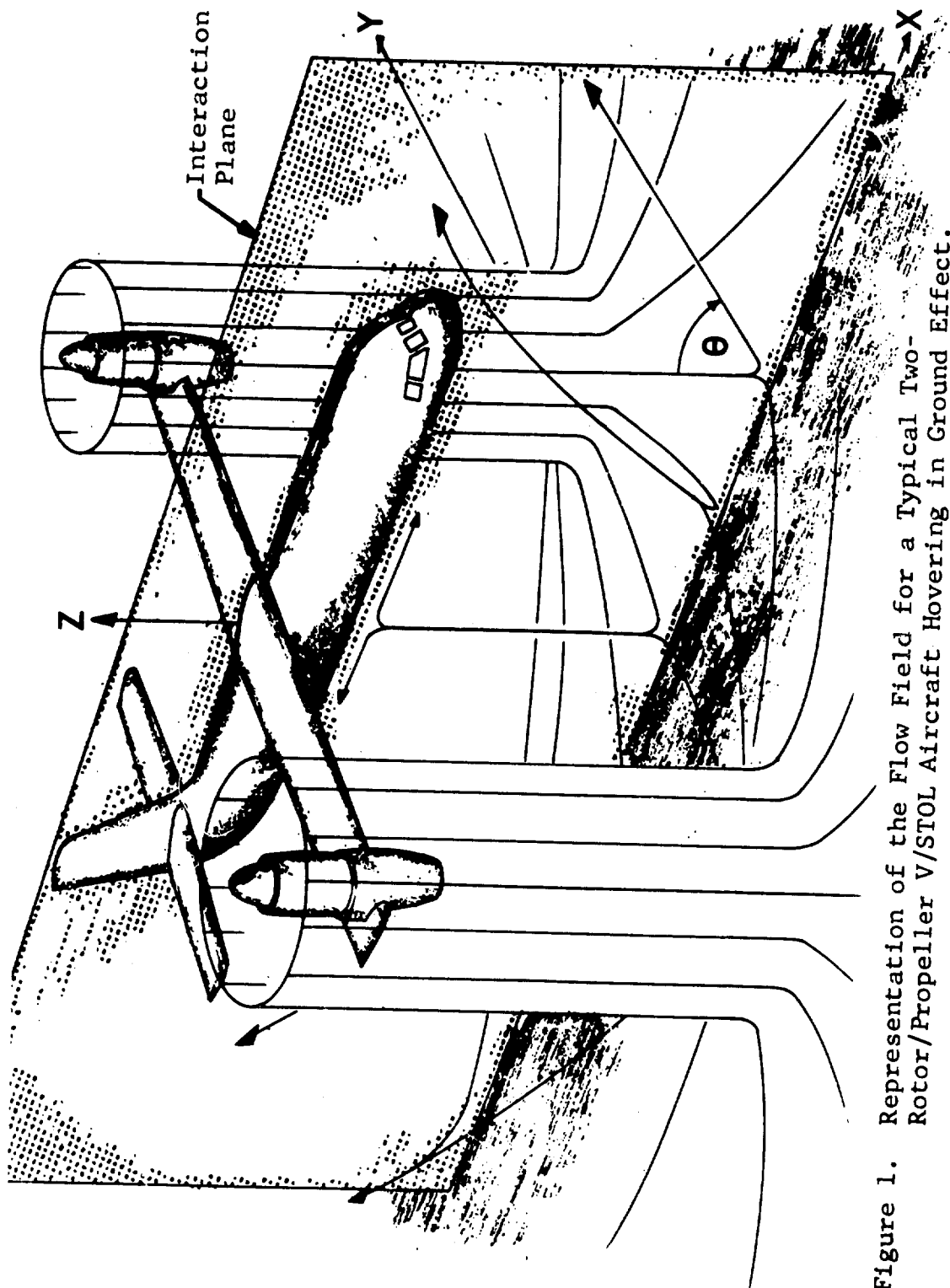
Figure 1. Representation of the Flow Field for a Typical Two-Rotor/Propeller V/STOL Aircraft Hovering in Ground Effect.

4
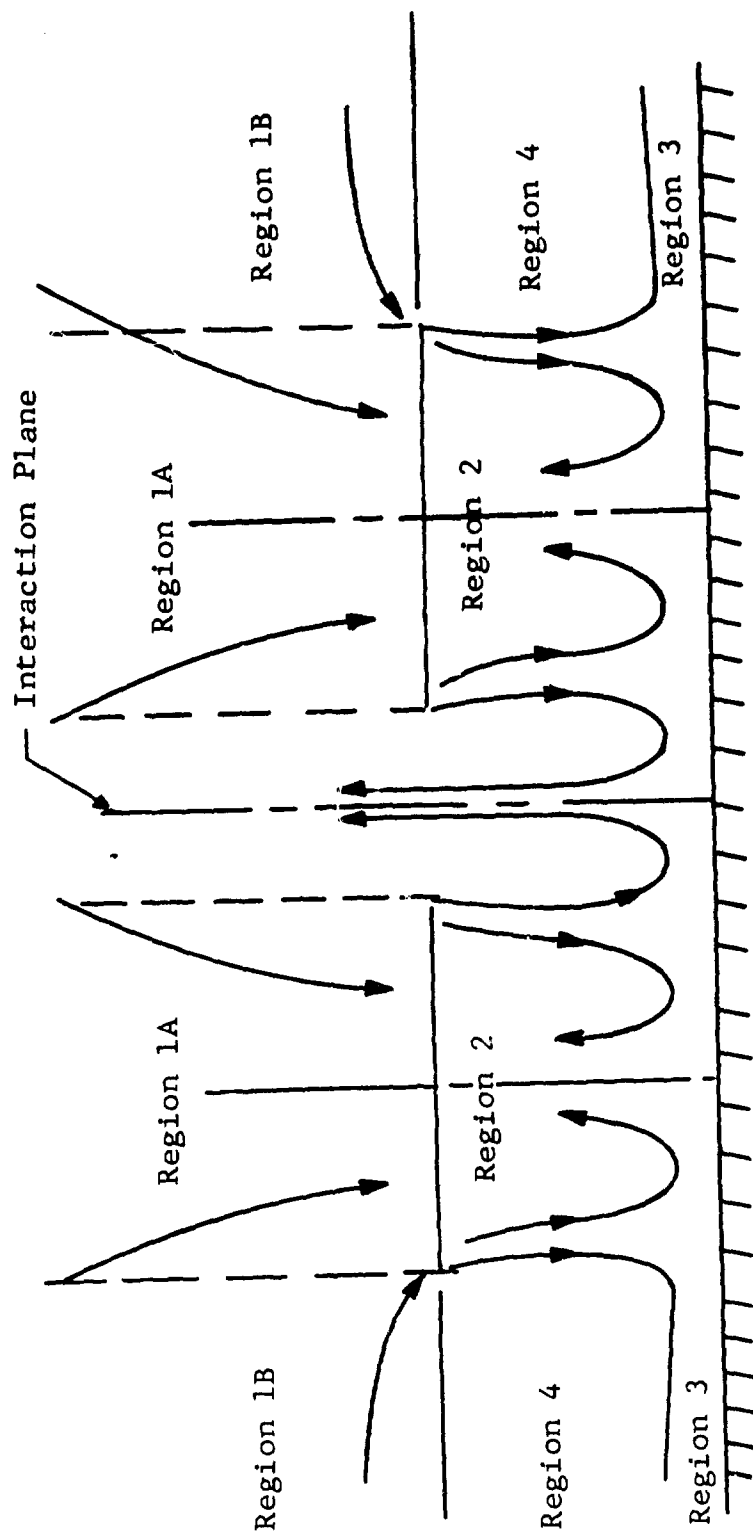
Figure 2. Definition of the Flow Regions in the Vicinity of Mutually Interacting Propellers/Rotors.

1. The Flow Field Above the Rotor Plane (Region 1)

a. Region 1A

The flow field in region (1A) pertains to the flow above the rotor plane and within the vortex cylinder (see Figure 2). It is assumed that within this region the interference of adjacent rotors is negligible; therefore, the flow field in this region can be treated as that of an isolated single rotor.

Thus, using the analytical methods of Reference 3, the following relationships are obtained for the axial and radial velocity components applicable to region (1A) of a two-rotor configuration:

$$\frac{U_z}{U_N} = \frac{3}{4}\left\{ \frac{r}{R} - \frac{(Z-H)}{R}\left[\frac{1}{\sqrt{1-\left(\frac{Z-H}{R}\right)^2}} \right.\right.$$

$$\left.\left. - \ln \frac{\sqrt{1-\left(\frac{Z-H}{R}\right)^2} - 1}{\frac{r}{R} - \sqrt{\left(\frac{r}{R}\right)^2 - \left(\frac{Z-H}{R}\right)^2}} \right]\right\} \quad (1)$$

$$\frac{r}{R}\frac{U_r}{U_N} = \frac{3}{4}\left\{ \frac{3}{4}\left(\frac{Z-H}{R}\right)^2 \ln\left|\frac{Z-H}{R}\right| - \frac{1}{2}\frac{r^2}{R^2}\left[\frac{1}{\left(1-\left(\frac{Z-H}{R}\right)^2\right)^{3/2}} \right.\right.$$

$$- \frac{\left(\frac{Z-H}{R}\right)^2}{\sqrt{1-\left(\frac{Z-H}{R}\right)^2}\left(1-\sqrt{1-\left(\frac{Z-H}{R}\right)^2}\right)}$$

6

$$- 1 - \ln\left(1 - \sqrt{1 - \left(\frac{Z-H}{R}\right)^2} \right) \right] - \frac{3}{4}\frac{r}{R}\sqrt{\frac{r^2}{R^2} - \left(\frac{Z-H}{R}\right)^2}$$

$$- \left(\frac{1}{2}\frac{r^2}{R^2} - \frac{3}{4} \right) \ln\left(\frac{r}{R} - \sqrt{\left(\frac{r}{R}\right)^2 - \left(\frac{Z-H}{R}\right)^2} \right) \Bigg\} \quad (2)$$

As can be seen from Reference 3, the preceding relationships, which yield a closed-form solution for the nonuniform velocity distribution in the vicinity and at the plane of a lifting rotor, correlate well with more complex computer solutions such as those presented in Reference 4.

b. **Region 1B**

This region pertains to the flow above the rotor plane and outside the vortex cylinder. For a two-propeller/rotor configuration the velocity field is obtained by considering two point sinks located at the centers of the two rotors. Thus, using the coordinate system of Figure 1, the velocity components in the X, Y, and Z directions of a two-propeller/rotor configuration are given by

$$\frac{U_X}{U_N} = -\frac{7}{24}\left\{ \frac{\dfrac{X-X_L}{R}}{\left[\left(\dfrac{X-X_L}{R}\right)^2 + \left(\dfrac{Y-Y_L}{R}\right)^2 + \left(\dfrac{Z-H}{R}\right)^2\right]^{3/2}} \right.$$

$$\cdot \frac{\frac{X - X_L}{R}}{\left[\left(\frac{X-X_L}{R}\right)^2 \cdot \left(\frac{Y-Y_L}{R}\right)^2 \cdot \left(\frac{Z-H}{R}\right)^2\right]^{3/2}} \Bigg\} \qquad (3)$$

$$\frac{U_Y}{U_N} = -\frac{7}{24} \Bigg\{ \frac{\frac{Y-Y_L}{R}}{\left[\left(\frac{X-X_L}{R}\right)^2 \cdot \left(\frac{Y-Y_L}{R}\right)^2 \cdot \left(\frac{Z-H}{R}\right)^2\right]^{3/2}}$$

$$\cdot \frac{\frac{Y-Y_L}{R}}{\left[\left(\frac{X-X_L}{R}\right)^2 + \left(\frac{Y-Y_L}{R}\right)^2 + \left(\frac{Z-H}{R}\right)^2\right]^{3/2}} \Bigg\} \qquad (4)$$

$$\frac{U_Z}{U_N} = -\frac{7}{24} \frac{Z-H}{R} \Bigg\{ \frac{1}{\left[\left(\frac{X-X_L}{R}\right)^2 + \left(\frac{Y-Y_L}{R}\right)^2 + \left(\frac{Z-H}{R}\right)^2\right]^{3/2}}$$

$$\cdot \frac{1}{\left[\left(\frac{X-X_L}{R}\right)^2 + \left(\frac{Y-Y_L}{R}\right)^2 + \left(\frac{Z-H}{R}\right)^2\right]^{3/2}} \Bigg\} \qquad (5)$$

Because of the three-dimensional character of the flow field defined by equations (3), (4), and (5), the pictorial presentation of the streamlines is not convenient except for the two planes of symmetry, the X-Z and the Y-Z plane.

In the X-Z plane, equations (3), (4), and (5) yield:

$$\frac{U_Y}{U_N} = \frac{U_Z}{U_N} = 0 \tag{6}$$

and

$$\frac{U_X}{U_N} = -\frac{7}{24}\left\{ \frac{1}{\left(\frac{X-X_L}{R}\right)^2} + \frac{1}{\left(\frac{X+X_L}{R}\right)^2} \right\} \tag{7}$$

At the location corresponding approximately to the leading edge of the front rotor, i.e., $X/R = 2X_L/R$, equation (7) reduces to:

$$\frac{U_X}{U_N} = -\frac{7}{24}\left[\frac{1}{\left(\frac{X_L}{R}\right)^2} + \frac{1}{9\left(\frac{X_L}{R}\right)^2} \right] \tag{8}$$

The second term of equation (8) corresponds to the effect of one rotor on the longitudinal velocity component U_X of the other rotor. Hence, at this location the mutual interference effects between the two rotors amount to approximately 11 percent of the total induced velocity component (U_X) due to an isolated rotor.

Figure 3 shows a comparison of the results obtainable by means of equation (5) with the results of the computerized analysis presented in Reference 4. Again, a good correlation between the two methods is indicated.
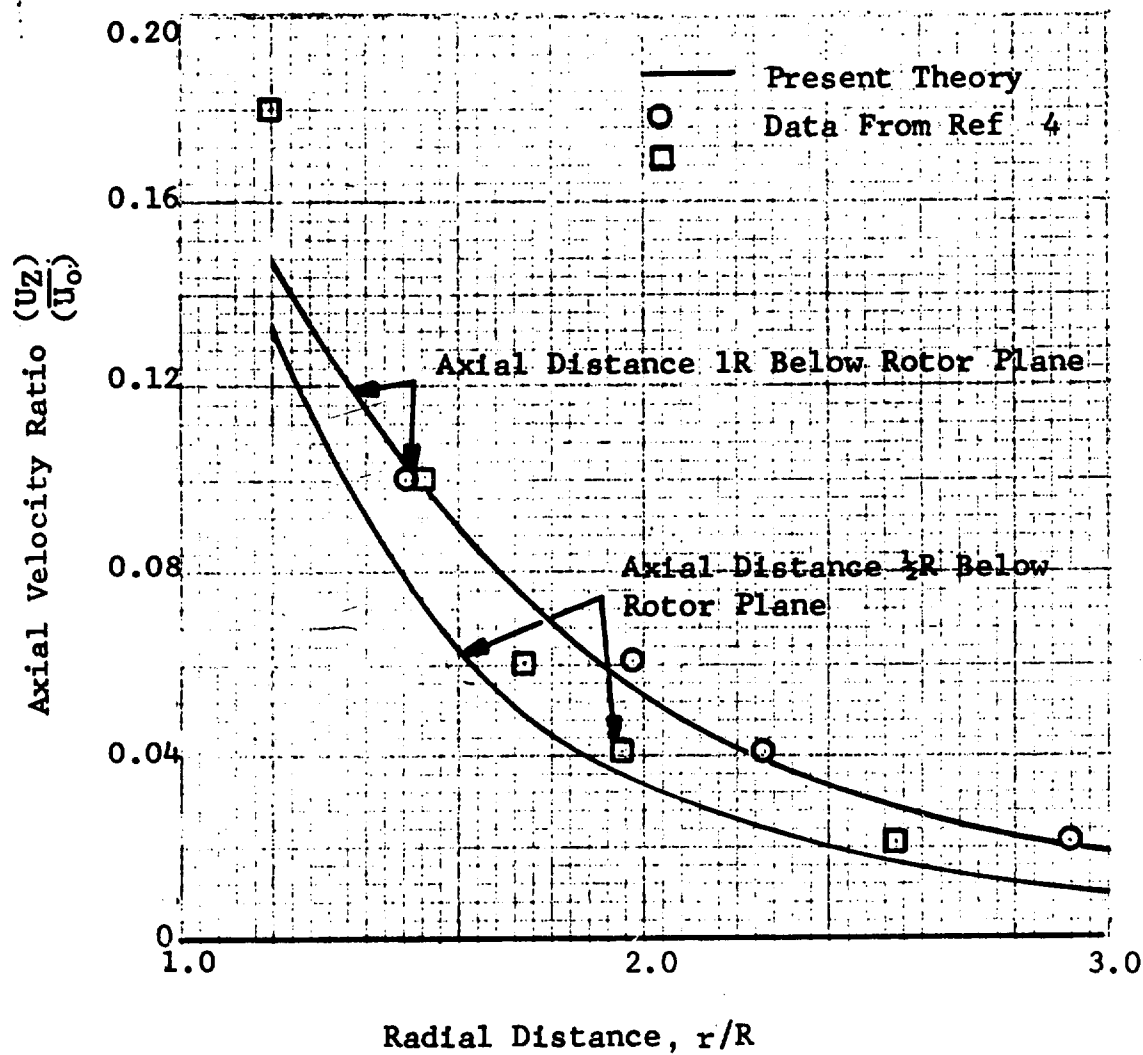
Figure 3. Variation of Axial Velocity Outside Vortex
Cylinder Versus Radial Distance for Axial
Distances of 0.5R and 1R Below the Rotor Plane.

The analysis for predicting the flow field of two mutually interacting rotors, for both inside and outside of the vortex cylinder (Region 1), applies only to out-of-ground-effect (OGE) conditions. A rotor operating in the proximity of the ground experiences a reduction in the induced velocity. This reduction can be accounted for by multiplying the out-of-ground-effect velocities by the ground correction factor, k_g. This factor is determined semiempirically as:

$$k_g = 1.0 - 0.9 \, e^{-2\left(\frac{H}{R}\right)} \tag{9}$$

Hence, the induced in-ground-effect (U_{IGE}) can be expressed as follows:

$$U_{IGE} = k_g \, U_{OGE} \tag{10}$$

The ground effect factor, k_g, given in Figure 4 represents reasonably well the test data of Reference 5. The ground effect correction factor, k_g, given by equation (9) is plotted in Figure 4, where the test data of Reference 5 are superimposed. When this figure is examined, a good correlation can be noted between the semiempirically established k_g factor and that obtained from the test data.

Utilizing the preceding analysis, the flow field above the rotor plane (Region 1) was calculated; the non-dimensionalized results thus obtained are presented in Figure 5 for out-of-ground-effect conditions ($H/R > 2.0$). For in-ground-effect operating conditions and any rotor height $H/R \leq 2.0$ above the ground, the velocity at any point in Region 1 was determined by multiplying the velocity ratio obtained from Figure 5 by the momentum slipstream velocity (U_o) and the appropriate k_g factor obtained from Figure 4.

11
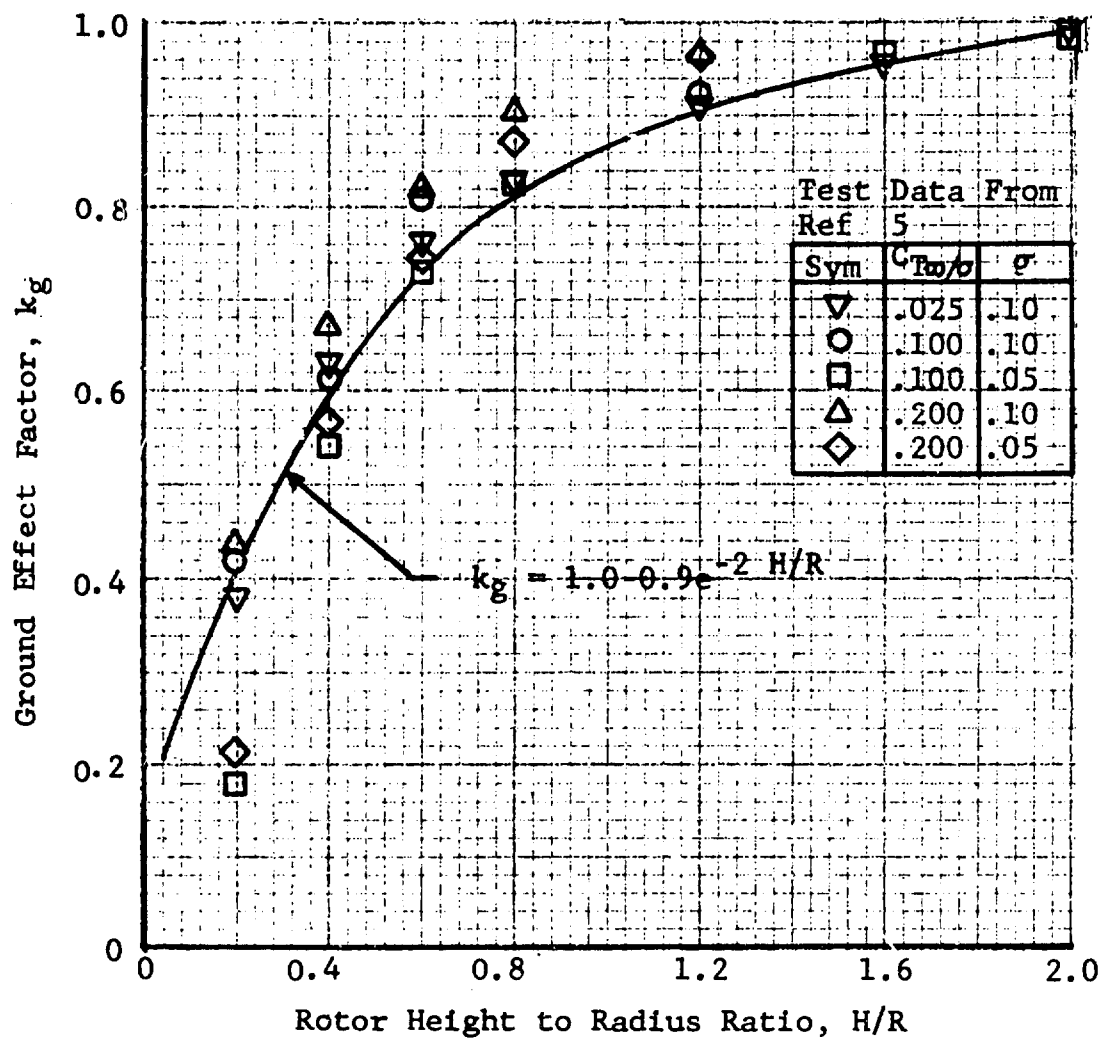
Figure 4. Effect of Thrust Coefficient and Solidity on the Ground Effect Inflow Correction Factor in Hovering.
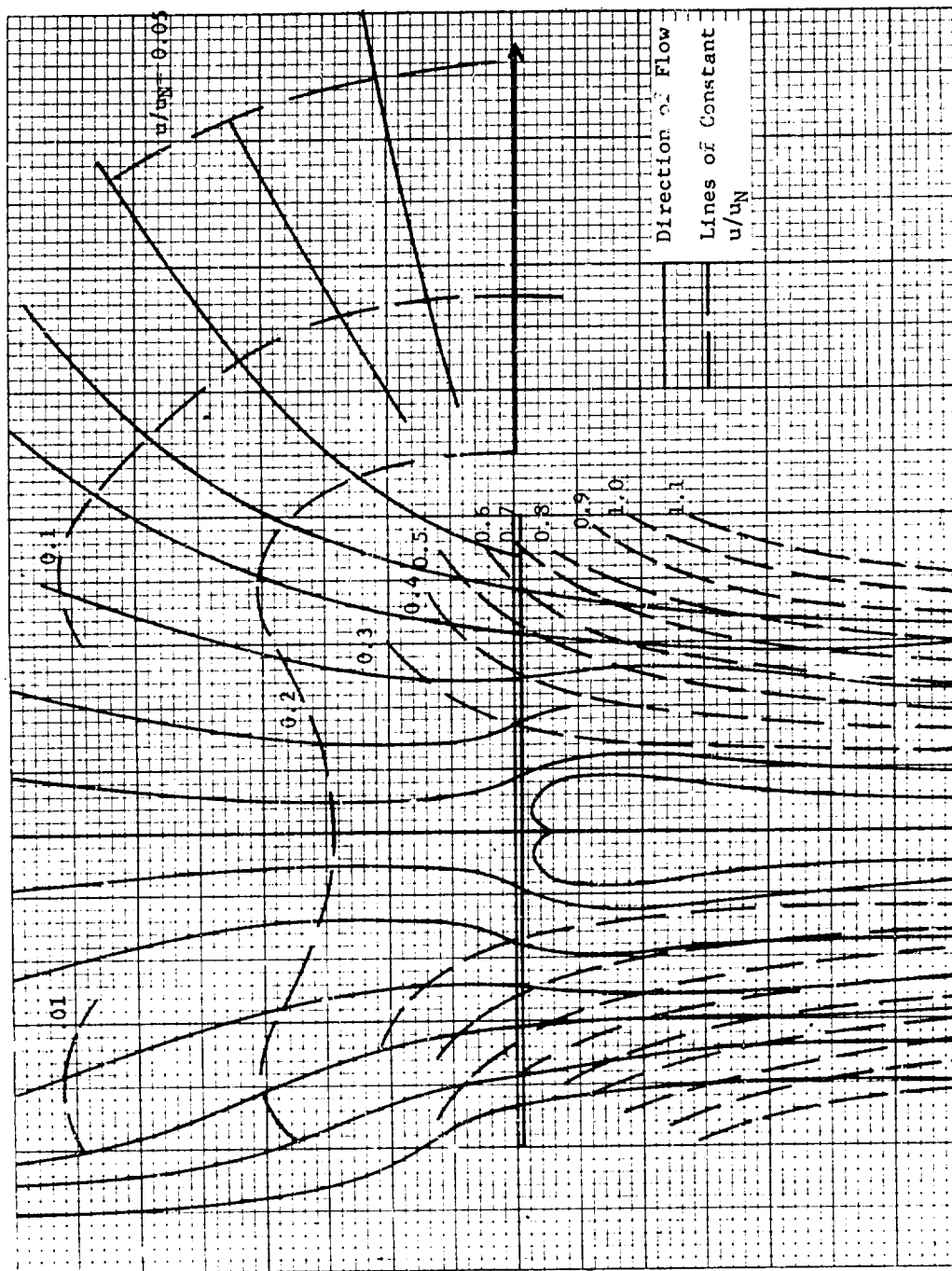
Figure 5. Flow Field in the Vicinity of a Hovering Rotor, Out of Ground Effect.

2. Flow Field Below the Rotor (Region 2)

Region 2 pertains to the flow field below the rotor plane and within the vortex cylinder (see Figure 2). For out-of-ground-effect conditions, this region may also be treated analytically by use of the same method used for Region 1A. In ground effect, however, these analyses are considered to be invalid. Therefore, in order to determine the flow field in this region, experimental data are herein utilized instead. Such data, though limited in quantity, are presented in Reference 2. This reference contains axial velocity profiles for rotor height of $H/D = 0.5$, and the smoke flow visualization data for other rotor heights. These data were utilized to construct velocity contours for other rotor heights using the superposition method of Reference 6.

Figure 6 shows the velocity distribution (contour plots) below the rotor (Region 2) for rotor heights of $H/R = 1$, .5, and .656. This figure can be used to obtain velocity contour plots immediately below the rotor or propeller plane of a VTOL aircraft operating at these heights to radius ratios. It should be noted that although the data presented in Figure 6 specifically apply to straight untwisted rotor blades, they are considered to be adequate for the analysis of the conventional rotor designs with moderate blade twist. For the case of high efflux jets or fans, a uniform velocity distribution at the jet exit may be assumed with the velocity reduced by k_g as in Region 1.

3. Flow Field in the Wall Jet (Region 3)

Region 3, as shown in Figure 2, pertains to the flow along the ground (outside the vortex cylinder) known as the wall jet region.

The behavior of flow along the ground is described in Reference 7. The radial velocity is zero at the rotor axis and increases linearly to a maximum value at a radial distance (r/D_e) approximately equal to 1.0. Then it decreases exponentially as the radial distance increases. The point at which the radial velocity along the ground is maximum (which also corresponds to the point where the pressure is atmospheric) is defined as the beginning of the
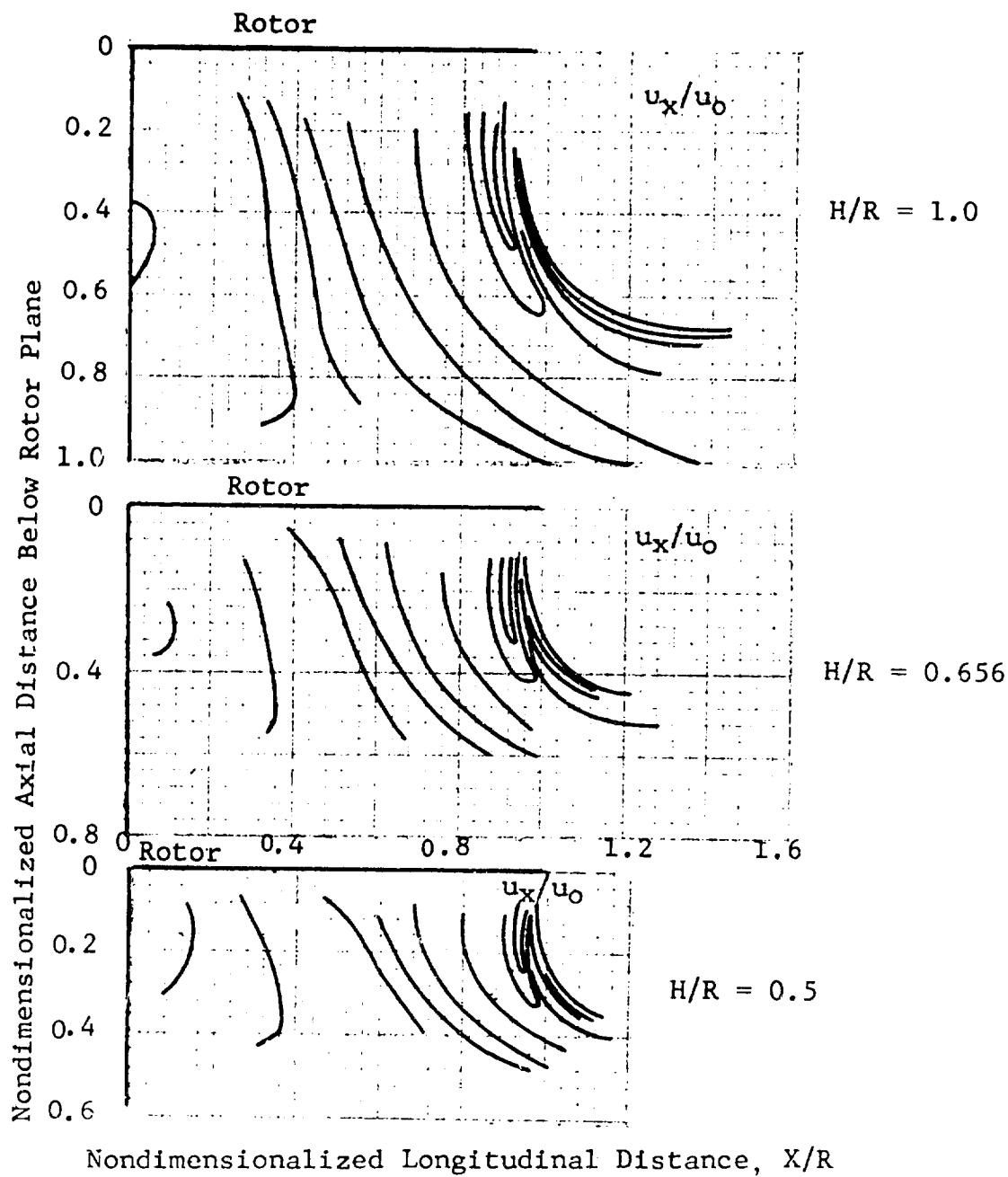
Figure 6. Downwash Velocity Distribution Below the
           Rotor in Ground Effect (Region 2).

well jet. Thus, the wall jet (Region 3) extends radially from there.

Reference 8 shows that the velocity profiles at any radial station along the ground within the wall jet region are affine. The wall jet velocity profile reproduced from Reference 8 and confirmed by experimental data of Reference 7 is herein presented in Figure 7. This figure shows a distribution of the velocity ratio u/u_m as a function of vertical distance ratio $(y/y_{\frac{1}{2}})$ within the wall jet.

Reference 7 also presents an analytical treatment of the flow in the wall jet region. This analysis, however, utilizes a free jet decay which is not representative of the air jet induced velocity produced by a rotor. Therefore, to obtain the decay of the dynamic pressure $(q_{s_{max}}/q_N)$ for a rotor, the data of Reference 9 presented herein as a plot of $q_{s_{max}}/q_N$ in Figure 8 are applied to the present analysis. As indicated in Reference 7, the maximum radial velocity in the wall jet (u_m) at any radial station (r) can be expressed as follows:

$$\frac{u_m}{U_N} = C_u \left(\frac{r}{R}\right)^{-1.143} \tag{11}$$

Also, the distance above the ground where the velocity equals half of the maximum velocity is given by:

$$\frac{y_{\frac{1}{2}}}{R} = C_y \left(\frac{r}{R}\right)^{1.028} \tag{12}$$

The wall jet constants C_u and C_y can be expressed as functions of the parameters $(u_m/U_N)_t$, $(y_{\frac{1}{2}}/R)_t$, and $(r/R)_t$ at the beginning of the wall jet as follows:

16
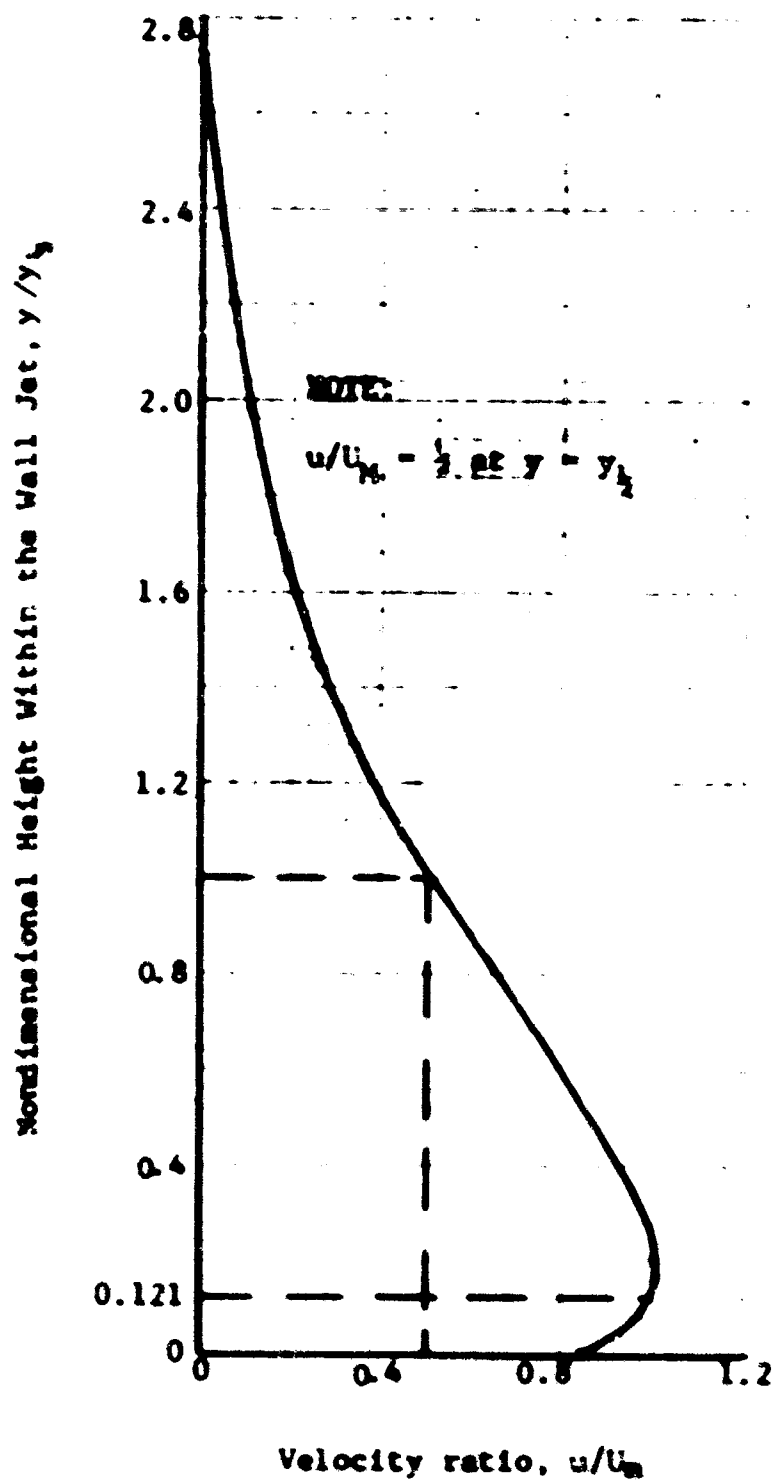
Figure 7. The Wall Jet Velocity Profile.

17
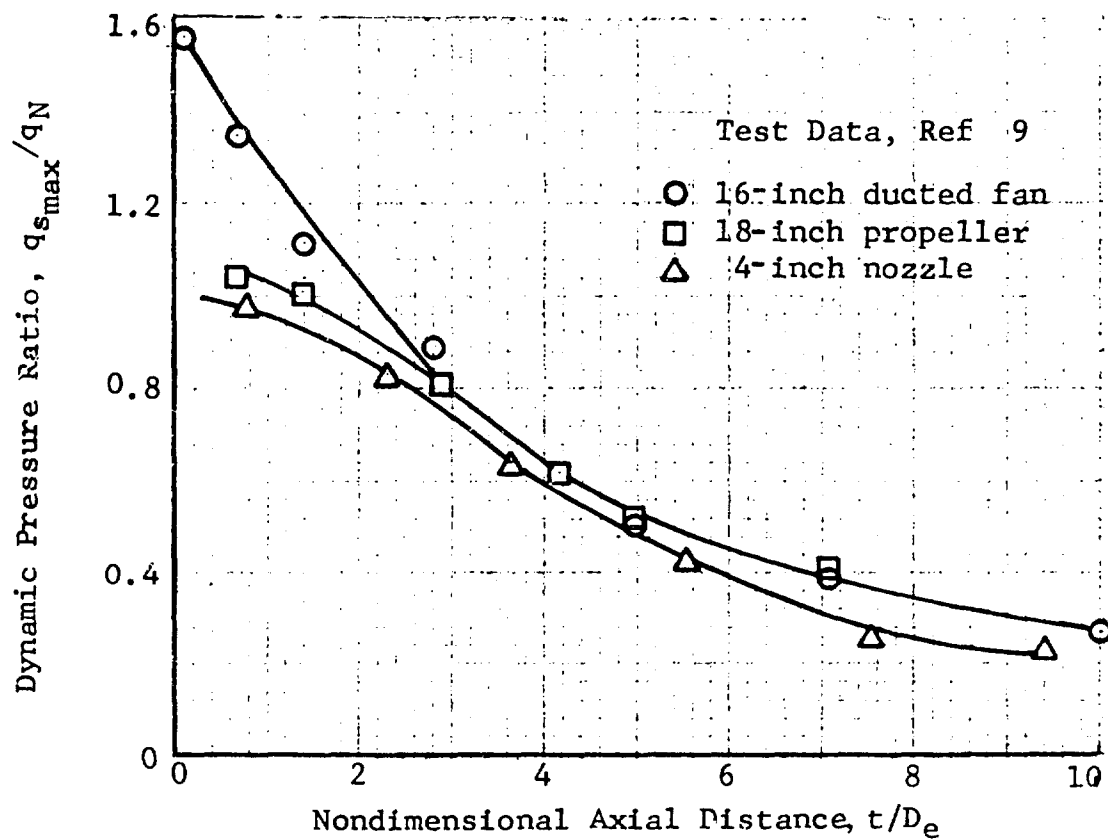
Figure 8.   Test Data on the Decay of Dynamic Pressure
With Axial Distance From the Jet Exit.

$$C_u = \left(\frac{u_m}{U_H}\right)_t \left(\frac{r}{R}\right)_t^{1.143} \qquad (13)$$

$$C_y = \left(\frac{y_{\frac{1}{2}}}{R}\right)_t \left(\frac{r}{R}\right)_t^{-1.028} \qquad (14)$$

The parameter $(y_{\frac{1}{2}}/R)_t$ can be expressed as follows:

$$\left(\frac{y_{\frac{1}{2}}}{R}\right)_t = \frac{0.654}{\left(\frac{u_m}{U_H}\right)_t \left(\frac{r}{R}\right)_t} \qquad (15)$$

In order to establish the wall jet constants C_u, C_y, and $(y_{\frac{1}{2}}/R)_t$ as given by equations (13) through (15), it is first necessary to determine the position of the beginning of the wall jet $(r/R)_t$ and the maximum velocity ratio $(u_m/U_H)_t$ at the wall jet.

This can be accomplished by utilizing the iterative procedure of Reference 7 as follows:

(a) Determine rotor height above the ground (H/R) and assume an initial value of $(r/R)_t \cong 2.0$.

(b) Calculate an equivalent free jet distance t/R using the following relationship:

$$\frac{t}{H} = \frac{H}{R} + \left[\left(\frac{r}{R}\right)_t - 1.0\right] \qquad (16)$$

19

(c) Transform the value of t/R into T/D_e which for open rotors is given by:

$$\frac{t}{D_e} = 0.707 \frac{t}{R} \qquad (17)$$

(d) Using the value of (t/D_e) from step (c), obtain the ratio of $(q_{s_{max}}/q_N)$ from the test data of Figure 8. Then compute

$$\frac{u_m}{U_N} = \sqrt{\frac{q_{s_{max}}}{q_N}} \qquad (18)$$

where U_N is the induced velocity of a fully developed slipstream, and for an open rotor U_N can be expressed as follows:

$$U_N = \sqrt{\frac{2\ DL}{\rho}} \qquad (19)$$

(e) Obtain the value of the average induced velocity at the rotor disc in ground effect ($\bar{U}$) by using U_N from step (d) and the appropriate value of the ground effect factor k_g from Figure 4:

$$\bar{U} = k_g (U_o)_{OGE} = k_g \frac{U_N}{2} \qquad (20)$$

where $(U_o)_{OGE}$ is the average induced velocity at the rotor plane out of ground effect.

20

(f) Compute the radial position at which the wall jet begins:

$$\left(\frac{r}{R}\right) = \frac{(1.45)^{0.486}}{(0.52)^{1.13}}\left(\frac{\overline{U}}{u_m}\right)^{0.486} \tag{21}$$

(g) Repeat steps (b) through (f) until convergence is obtained for the value of the position where the wall jet begins, $(r/R)_t$.

(h) Using the final value of $(r/R)_t$ from step (g), $\overline{U}$ from step (e), and u_m from step (d), calculate $\overline{u}_M$ using the following relationship:

$$\overline{u}_M = \left[0.385\left(\frac{r}{R}\right)_t^{0.885} u_m \overline{U}^{0.14}\right]^{0.88} \tag{22}$$

(i) Using the values of u_m from step (d), $(r/R)_t$ from step (g), and $\overline{u}_M$ from step (h), calculate $(y_\frac{1}{2}/R)_t$ using equation (15).

(j) Finally, compute the wall jet constants C_u and Γ by using equations (13) and (14), respectively.

4. Flow within the Recirculation Region

Region 4, as shown in Figure 2, pertains to the flow field between the wall jet boundary and the plane of the rotor outside the vortex cylinder. The wall jet boundary is herein defined as the height at which the local velocity is equal to 1% of the maximum ground surface velocity (i.e., $u = 0.01 u_{max}$).

The outward radial flow in the wall jet interacts with the inward flow induced by the rotor, and a recirculatory flow in this region results. This flow phenomenon is clearly defined in the experimental work of References 2, 10, and 11. The analytical treatment of the flow in this region is extremely difficult, and no theoretical solutions are available in the existing literature. Some qualitative experimental data pertaining to the flow field in this region are presented in Reference 11 and in Figure 9. These data, however, are not adequate for the application in the present program. Due to shear flow interaction effects and small magnitudes of the velocities in this region, quantitative experimental data are practically nonexistent.

Hence, in the present approach, the analysis of the flow in this region utilizes a number of simplifying assumptions, the validity of which must be determined experimentally.

As defined previously, the external flow along the upper boundary of the wall jet ($u = 0.01 \, u_{max}$) is practically stationary; i.e., the axial and radial velocity components are considered to be zero.

Furthermore, it is herein postulated that the assumptions inherent in equation (10) will also apply to the recirculation region, provided that the required boundary conditions at the wall jet and at the plane of rotor disc are satisfied. One way to achieve this is to multiply equation (10) by a correction factor F_h which varies linearly from $F_h = 1.0$ at the plane of rotor disc to $F_h = 0$ at the boundary of the wall jet.

Thus, equation (10) becomes

$$U_{ICE} = k_g \, U_{OGE} \, F_h \tag{23}$$

Using Figure 10, the correction factor F_h can be obtained as follows:
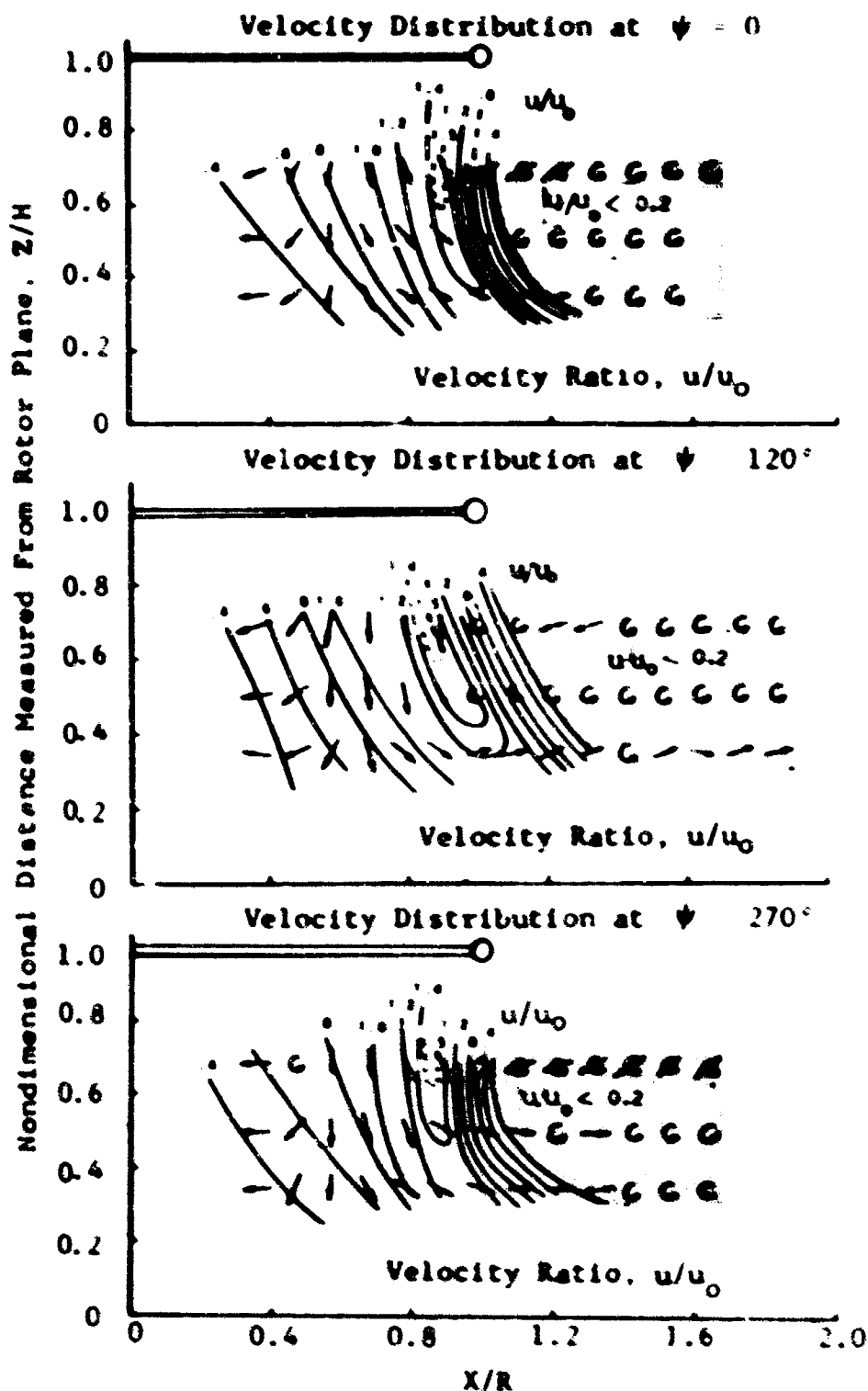
Figure 9. Downwash Velocity in Ground Effect for a 75-Foot Rotor at H/R 0.44.

23
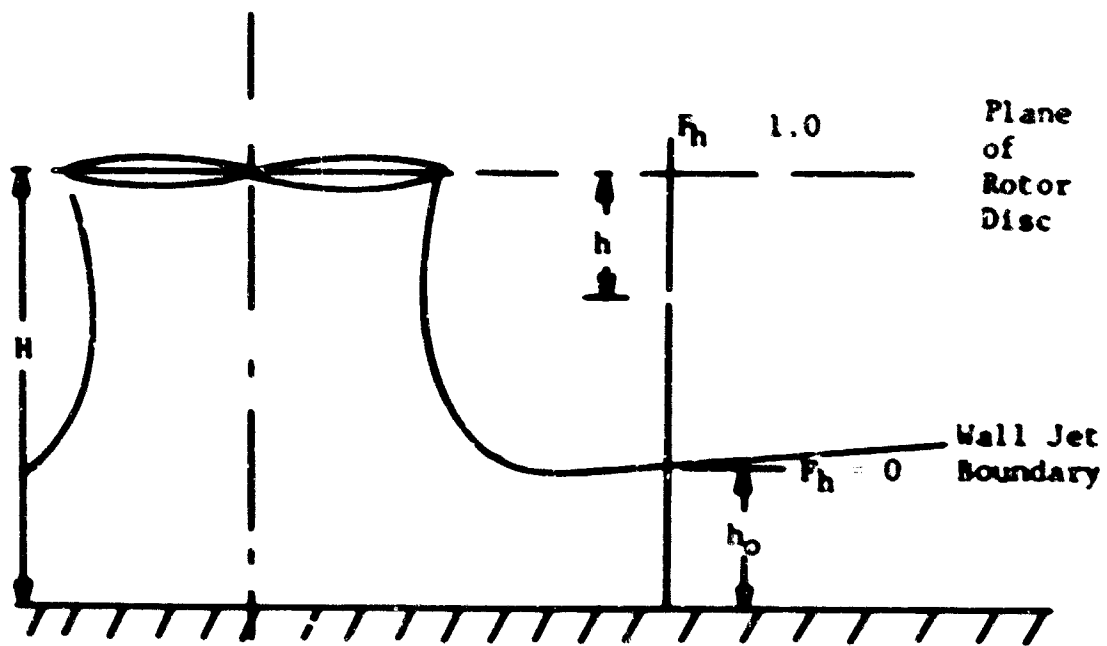
(a)
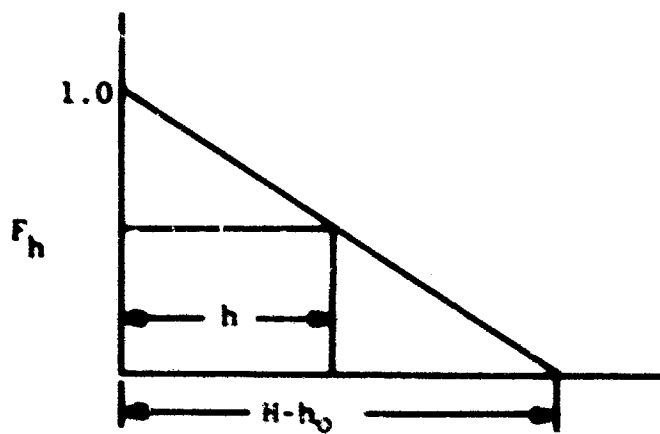
(b)

Figure 10. Schematic Representation of the Flow Field
in the Recirculation Region.

24

$$F_h = \frac{H - h_o - h}{\dot{\gamma} - h_o}$$

(24)

Substituting equation (24) into equation (23), the induced velocity in the recirculation region at any radial station r and at any vertical location (h) below the rotor disc plane can be expressed as follows:

$$U_{IGE} = k_s \, U_{OGE} \left(1 - \frac{h}{H - h_o} \right)$$

(25)

5. Flow in the Interaction Plane (Region 5)

The flow in Region 5, as shown in Figure 2, pertains to the flow in the interaction plane where the downwash from the two rotor/propellers meet. Along this plane, the downwash velocities from the two lift devices interact with each other, and the resultant flow is turned upward. For side-by-side rotor/propeller configurations, this upward flow is restrained by the fuselage and is diverted horizontally along the longitudinal axis of the aircraft. For tandem configurations with no rotor overlap, the interaction plane is along the lateral axis of the aircraft; hence, there is a minimum fuselage restraint, and practically all of the resultant flow will be turned vertically upward.

Conceptually, the interaction plane can be considered as a thin vertical wall (no flow through the wall) at which the radial flow along the ground from each rotor is deflected along the vertical plane at the same angle as if the ground flow continued (see Figure 11). Thus, the dynamic pressure (or the corresponding velocity) at a point in the interaction plane can be considered to be the same as if the flow from the single rotor continued along the ground at the same total distance from the rotor axis.

The test data of Reference 12 show that the resultant velocities along the interaction plane due to two rotors are greater than those for an isolated rotor at the same total

25
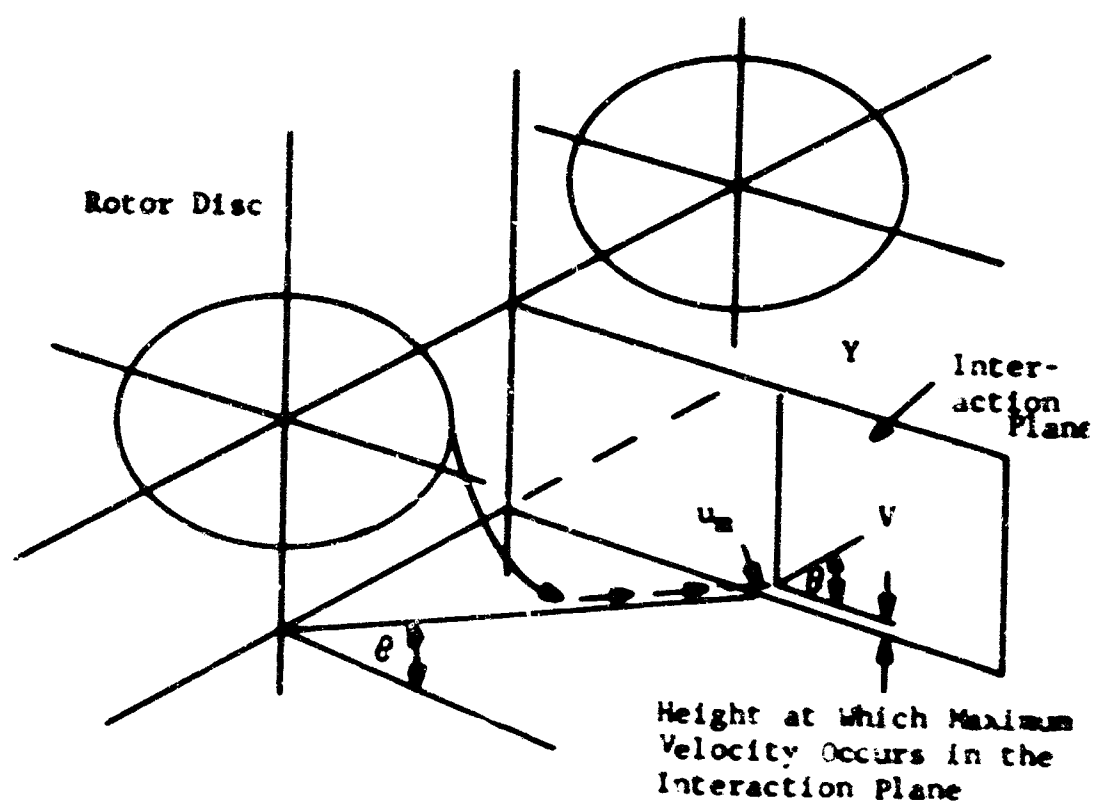
Figure 11. Schematic Representation of the Flow Field Along the Interaction Flow.

radial distance. These data have been utilized to develop a velocity interference correction factor, T_f, which is presented as a function of a total radial distance from a single rotor in Figure 12.

Using the nomenclature of Figure 13, th horizontal and vertical velocity components V_H and V_V can be expressed as follows:

$$V_H = T_f \ u_m(X/R) \qquad (26)$$

$$V_V = T_f \ u_m(Y-Z)/R \qquad (27)$$

B. DOWNWASH SIGNATURES

1. Dust Cloud Size and Shape

As discussed previously, the impingement of rotor downwash on the ground results in a high-velocity flow along the ground and the subsequent erosion and entrainment of ground particles. These particles, once eroded, are transported aloft by the flow field generated by the hovering aircraft and thus form a dust cloud. References 9 and 13 indicate that the particle erosion upon a specific terrain is a function of the maximum dynamic pressure $(q_{s_{max}})$ on the ground and the terrain erosion factor (k_t) which is dependent on the terrain characteristics.

As noted in Reference 9, the parameter which governs the particle terrain erosion is related to the effective surface dynamic pressure which can be expressed as follows:

$$(q_s)_{eff} \ \frac{(q_s)_{max}}{\sqrt{k_t}} \qquad (28)$$
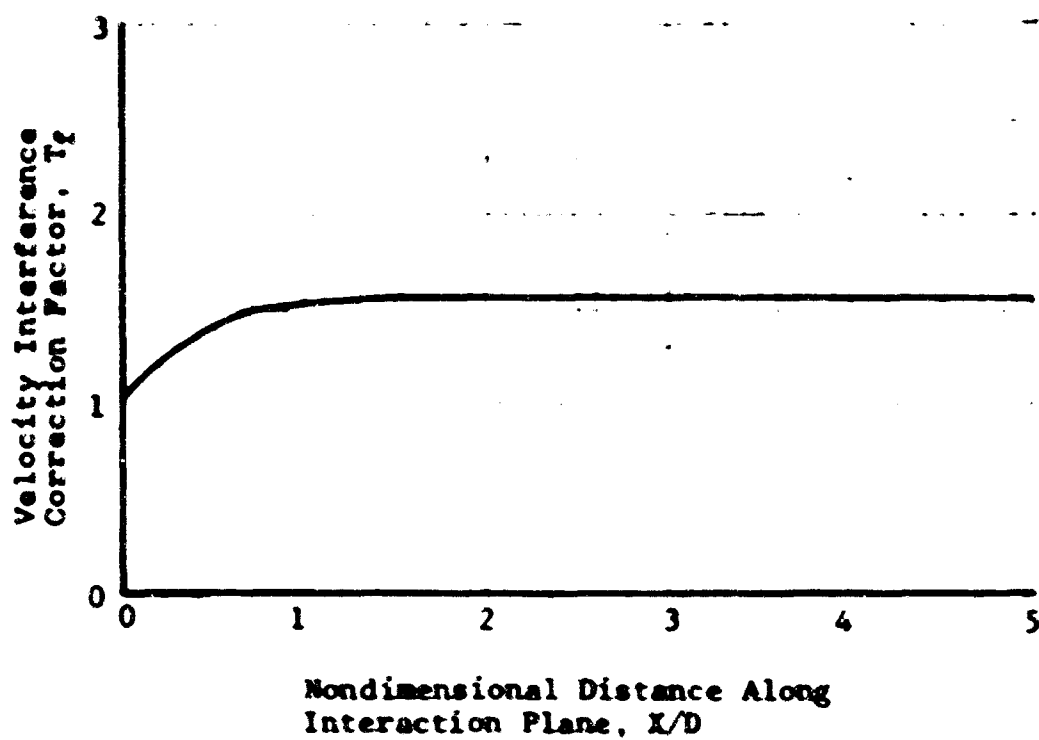
Figure 12. Correction Factor For Determining Velocities Within the Interaction Plane.
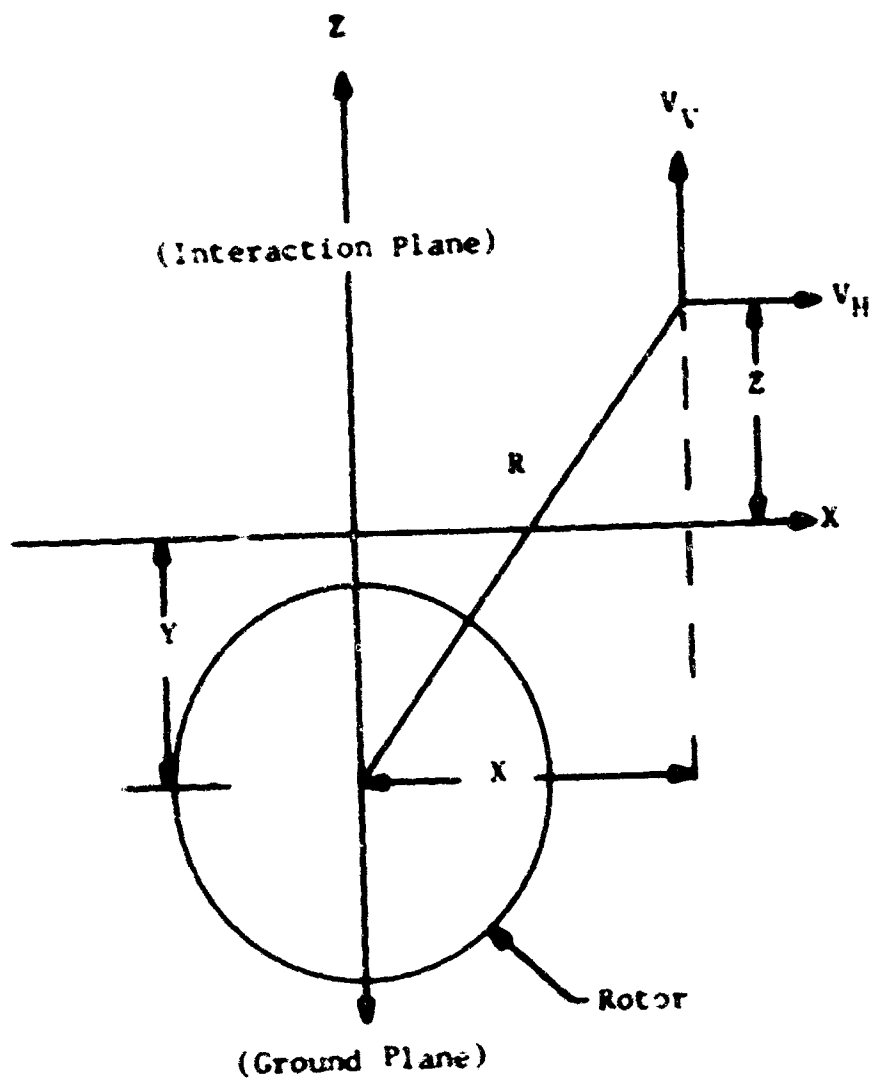
Figure 13. Definition of Parameters Within the Interaction Plane.

The terrain erosion factor, k_t, is given by:

$$k_t = \frac{\overline{D}_p \rho_p}{D_{pw} \rho_{pw}} \tag{29}$$

This terrain factor relates the terrain characteristics, i.e., terrain density and mean particle size, with water droplet size and density. Water droplet size was obtained from Reference 14.

From the film data, which were obtained by the Mine Safety Research Corporation as a part of the test program reported in Reference 15, it is determined that the dust cloud radial boundary can be approximated by the radial distance along the ground at which the surface effective dynamic pressure is approximately equal to 1.0 (i.e., $(q_s)_{eff} = 1.0$). Thus, the radial location of the dust cloud boundary can be readily obtained from equation (28) using the wall jet and the interaction plane analyses presented in Section II. A. The resulting dust cloud radius (boundary) can be expressed as follows:

$$R_c = R \left[\frac{\sqrt{k_t}}{C_1 \rho \, U_m^2 C_u^2} \right]^{-.437} \tag{30}$$

where $C_1 = 0.5$ for regions outside the interaction plane and $C_1 = 1.1$ along the interaction plane.

The height of the dust cloud (maximum vertical location of the cloud boundary) can be approximated by considering the path of the rotor blade tip vortices as they spread along the ground. The ground spreading of the rotor blade tip vortices is believed to be the primary cause for the cloud roll-up observed from the film data.

30

A detailed analysis of the behavior of this vortex system along the ground can be made by replacing the continuous cylindrical vortex sheet with a finite number of discrete wing vortices. A step-by-step iteration procedure could then be applied to compute the motion of each ring vortex as it starts to expand along the ground. However, in lieu of this process, which is complicated, time consuming, and would require a computer solution, an attempt was made to analyze the roll-up process utilizing an analogy of the vortex sheet shed from the trailing edge of a lifting wing as schematically shown in Figure 14.

It can be seen that the vortex pattern behind the lifting wing (Figure 14(b)) exhibits a flow mechanism very similar to that shown along Section A-A (Figure 14(a)) of the ring vortex sheet generated by a lifting rotor. The main difference between the flow mechanism of the cylindrical vortex sheet of a rotor and the vortex sheet of a lifting wing is that the former rolls up and forms a torus ring while the latter rolls up into two line vortices.

Using the above analogy, conventional wing vortex theory such as that presented in Reference 16 is applied to predict the center of the vortex core. Using the nomenclature of Figure 14(a), the coordinates of the center of the vortex core for complete roll-up can be expressed as follows:

$$R_V = 0.785 R_c \qquad (31)$$

$$Z_V = 0.329 R_c \qquad (32)$$

Once the center of the core is defined, the cloud roll-up is approximated by a logarithmic spiral relationship given by:

$$\lambda = e^{a(\phi - \phi_o)} \qquad (33)$$

where a and ϕ_o are constants which can be determined by applying the boundary conditions of $\phi = 0$ when $\lambda = R_c - R_V$

31
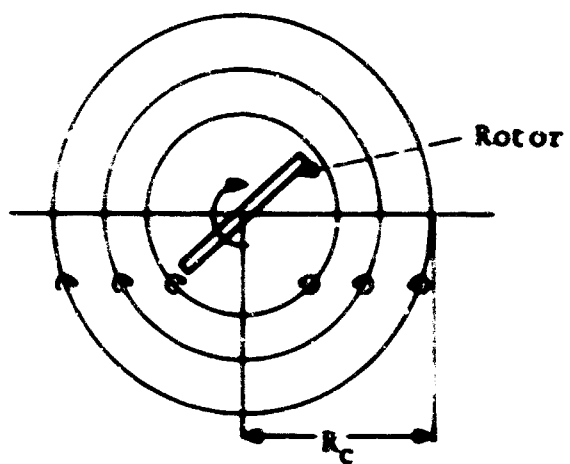
(a) Lifting Rotor Vortex
     Pattern
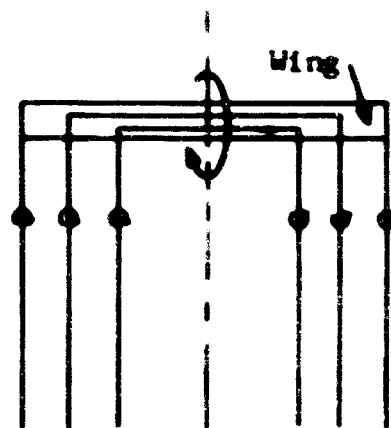
(b) Lifting Wing Vortex
     Pattern
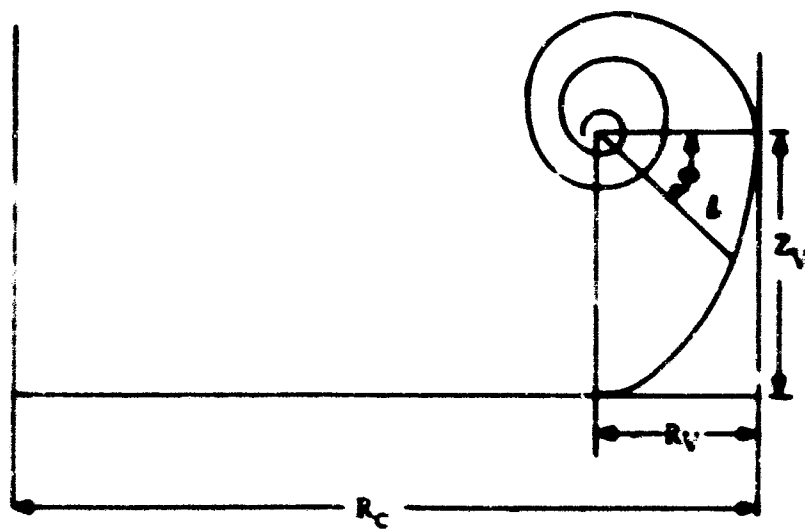
(c) Logarithmic Spiral Representation of
     Vortex Roll-Up

Figure 14. Schematic Representation of a Lifting Rotor
            Vortex System in Ground Effect.

32

and $\phi = \pi/2$ when $\phi \quad Z_V$. Applying these boundary conditions to equation (33), there results:

$$a = \frac{2}{\pi} \log \left(\frac{Z_V}{R_C - R_V} \right) \tag{34}$$

$$\phi_0 = \pi \log \left(\frac{R_C - R_V}{Z_V} \right) \tag{35}$$

Thus, knowing the radial location of the dust cloud boundary (R_C) and the constants a and ϕ_0, the vertical location of the dust cloud boundary measured from the center of the vortex spiral can be computed by substituting $\phi = -\pi/2$ in equation (33). Thus,

$$h_V = e^{a(-\frac{\pi}{2} - \phi_0)} \tag{36}$$

The total dust cloud height measured from the ground is then given by:

$$H_C = h_V + Z_V \tag{37}$$

2. **Cloud Content**

   a. **Particle Density Distribution**

      (1) **Far Field Density Distribution**

          In the far field flow region of VTOL aircraft
          (i.e., the region from the start of the wall jet
          to the boundary of the cloud), the particle
          density distribution within the cloud is derived
          based on the analysis presented in Reference 17.

33

By assuming particle characteristic paths and
by considering the rate of loss of momentum of
the air due to particle movement, a semi -
empirical expression is derived in this
reference which gives the particle mass flow
rate along a lane of unit width for the case of
constant wind blown over desert sand. This
expression is given as:

$$m_* \quad C_2 \; \rho \; V_* \sqrt[3]{\frac{D_{P*}}{D_S}} \tag{38}$$

where the constant C_2 was found experimentally
to be C_2 1.5 for nearly uniform sand, C_2 1.8
for naturally graded sand, and $C_2 = 2.8$ for sand
with a wide range of grain size. The parameter
V_* is given by:

$$V_* = \sqrt{\frac{\tau}{\rho}} \tag{39}$$

Reference 17 defines (τ) as shearing force or
drag per square cm of ground surface parallel
to the wind direction. Also, V_*, which is
merely a mathematical symbol, is defined as the
drag velocity which is directly proportional to
the rate of increase of the wind velocity with
the log-height. Since the velocity and the
log-height have a straight line relationship,
V_* is proportional to the tangent of the angle
which this straight line or velocity ray makes
with the height ordinate. The proportionality
constant is determined experimentally to be
5.75. Furthermore, Reference 17 shows that if
the wind velocity close to the surface is
plotted against the log-height, the zero wind

34

velocity occurs at a certain small but definite height above the ground surface. This height is found to be associated with the size of the irregularities which constitute the surface roughness and is approximately equal to 1/30 the diameter of the grain size on the surface.

In utilizing the results of Reference 17, it is now necessary to relate the mathematical parameter V_* to the parameters in the boundary layer of the rotor wall jet flow. For this purpose the boundary layer thickness (y_m) in the wall jet flow is herein defined as the vertical distance at which the wall jet velocity is a maximum.

Although the velocity in the rotor wall jet flow is nonuniform (see Figure 7) as compared to the uniform (constant) ambient wind velocity assumed in Reference 17, it is believed that the flow in the boundary layer will be analogous for both types of flow. Therefore, the drag velocity V_* within the boundary layer of the wall jet flow can be expressed as follows:

$$ V_* = \frac{u_m}{5.75 \log \left(\dfrac{30 \ y_m}{D p_*} \right)} \tag{40} $$

where y_m, the boundary layer thickness in the wall jet, is obtained from Figure 7 as

$$ \frac{y_m}{y_{\frac{1}{2}}} = 0.121 \tag{41} $$

The particle mass flow rate, m_*, per unit width can now be obtained by substituting equation (40) into equation (38):

35

$$\mathbf{m} = C_2 \, \rho \left[\frac{u_*}{5.75 \, \log \left(\frac{30 \, y_*}{D_{P_*}} \right)} \right]^3 \sqrt{\frac{D_{P_*}}{D_S}} \qquad (42)$$

Also, examining the test data of Reference 14, it can be noted that the particle mass flow rate $\mathbf{m}$ (lb/sec-ft^2), when plotted on a log scale versus height (Z), exhibits linear relationship with height. Furthermore, the integrated value of $\mathbf{m}$ with respect to Z yields the particle mass flow per unit width :

$$\mathbf{m}_* = \int_0^{H_C} \mathbf{m} \, dZ \qquad (43)$$

Using equation (43), the particle mass flow rate per unit area $\mathbf{m}_0$ (lb/sec-ft^2) along the ground can now be expressed in terms of the particle mass flow rate per unit width $\mathbf{m}_*$ (lb/sec-ft) as follows:

$$\mathbf{m}_0 = 10^{-K} + 2.3 \frac{\mathbf{m}_*}{H_C} (K + \log \mathbf{m}_0) \qquad (44)$$

where K is a positive integer chosen such that $\mathbf{m} \approx 0$ when $\mathbf{m}_0 \leq 10^{-K}$.

In performing graphical solutions of equation (44), it was determined that a value of $K \geq 6$ did not affect the numerical values of $\mathbf{m}_0$.

36

Therefore, the value of $K = 6$ was utilized in the subsequent analysis. The parameter 10^{-K} represents the particle mass flow rate at the boundary of the cloud (H_c). In previous theoretical analyses of the cloud constant, that value was assumed to be zero. However, from actual observation of the cloud patterns, it is inferred that certain small particle mass flow will exist even at the cloud boundary. It is therefore believed that the representation of this small mass flow rate by a factor of 10^{-K} is more realistic than the assumption of $m = 0$ at the cloud boundary.

The particle mass flow rate distribution as a function of height within the duct cloud $m(Z)$ can now be obtained graphically by knowing a value of m_0 and drawing a straight line on a log-m scale from m_0 to $m = 10^{-K}$ at the cloud boundary (H_c).

(2) <u>Near Field Density Distributions</u>

The near flow field particle density distribution (at or below the rotor disc) in the region where the rotor induced flow is down through the disc was computed utilizing the flow continuity concept within a given stream tube. In this approach, it is assumed that the dust particles which get entrained from the dust cloud into the rotor plane travel along discrete stream tubes of the flow in which the basic law of mass flow continuity applies. It is further assumed that no particles are added or taken away from each stream tube and that there is no cross flow between the stream tubes.

If this concept of particle flow within a confined stream tube is utilized, it follows that the particle density distribution at points within the rotor plane or in the rotor slip-stream (near flow field) is the same as that at

37

the appropriate locations within the dust cloud
where the stream tube of the rotor induced flow
immerses in the cloud. Hence, the near flow
field particle density distribution can be
computed knowing the far flow field densities
at the appropriate locations within the dust
cloud. The far flow field particle densities
can be obtained utilizing the following
equation:

$$(\rho_p)_{Av} = \frac{m}{u} \qquad (45)$$

In utilizing equation (45), the average value of
the near flow field density can be approximately
obtained as that corresponding to the center
point of the cloud roll-up above the rotor plane
(Figure 15).

Although the above approach is considered to be
adequate for predicting an average (order of
magnitude) particle concentration at or below
the rotor plane, it is believed to be inadequate
for computing detailed particle distributions in
the rotor near flow field. This is due to the
fact that some of the dust particles which
actually recirculate through the rotor disc are
those which are entrained directly from the
ground under their own momentum through the
rotor "fountain flow" and from the recirculation
region discussed previously.

An analytical treatment of the trajectories of
discrete particles as affected by the airflow,
the particle initial momentum, and the aero-
dynamic and gravitational forces acting on each
particle is indeed very complicated and is
considered to be outside the scope of the present
work.

Because of a lack of such rigorous theoretical
analysis on particle trajectories, a semi-
empircal method postulated on pages 37 and 38 is

38
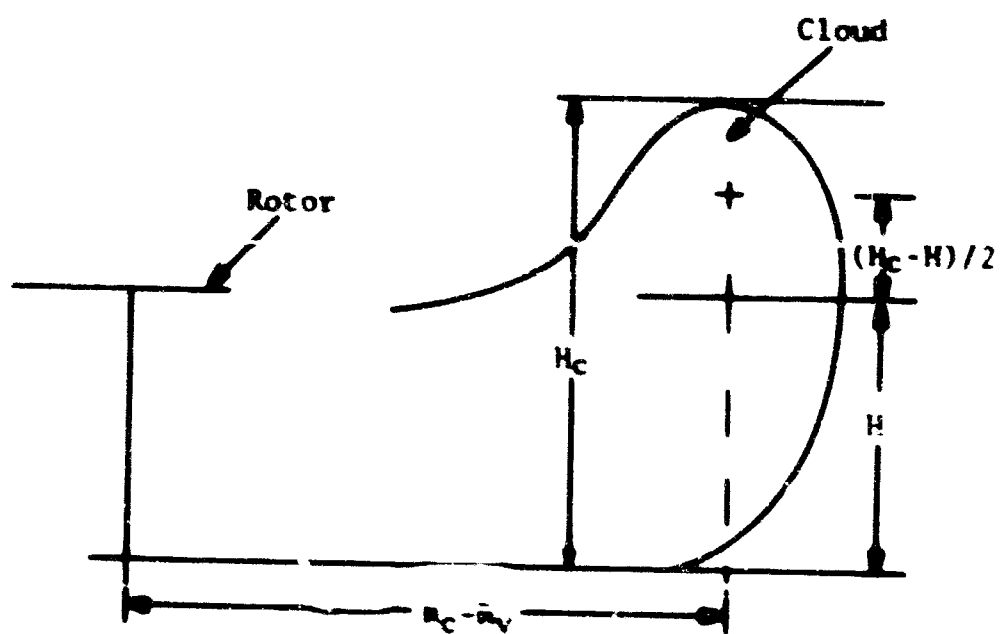
Figure 15. Schematic Representation of Dust Cloud Geometry.

herein utilized to obtain an indication of the
order of magnitude of dust particle concentra-
tion at the rotor plane or at the probable
location of engine intakes below the rotor. The
results obtained by this method are expected to
be lower than those obtained from the tests
primarily because of the nature of the assump-
tions utilized in the analysis.

b. **Particle Size Distribution**

A method of predicting the particle size distribution
in the downwash is presented in Reference 9. This
method is based on the terminal velocity principle
set forth by Kuhn in Reference 18, in which the free-
fall terminal velocity of a particle is equated to
the upflow velocity required to support this
particle. This relationship was used to predict the
maximum size of spherical sand particles that can be
supported by a given air velocity. The results are
shown in Figure 16, which is reproduced from
Reference 18.

The general procedure for determining the maximum
size particles is to first obtain the magnitudes of
the upflow velocities in the vicinity of the rotor
operating in ground effect. Then the maximum size
of the transported particles is obtained from Figure
16.

Once the maximum size of particles that can be
supported by the local airflow is determined, it is
related to the distribution of particles on the
ground in the following manner. If the maximum size
of transported particles is larger than the maximum
size of particles available on the ground, then the
distribution of particles in the air is assumed to
be equal to that of the ground sample. If, however,
the predicted maximum size of particles that can be
supported by the local airstream is smaller than the
maximum size on the ground, then the airborne particle
distribution is modified as follows:

40
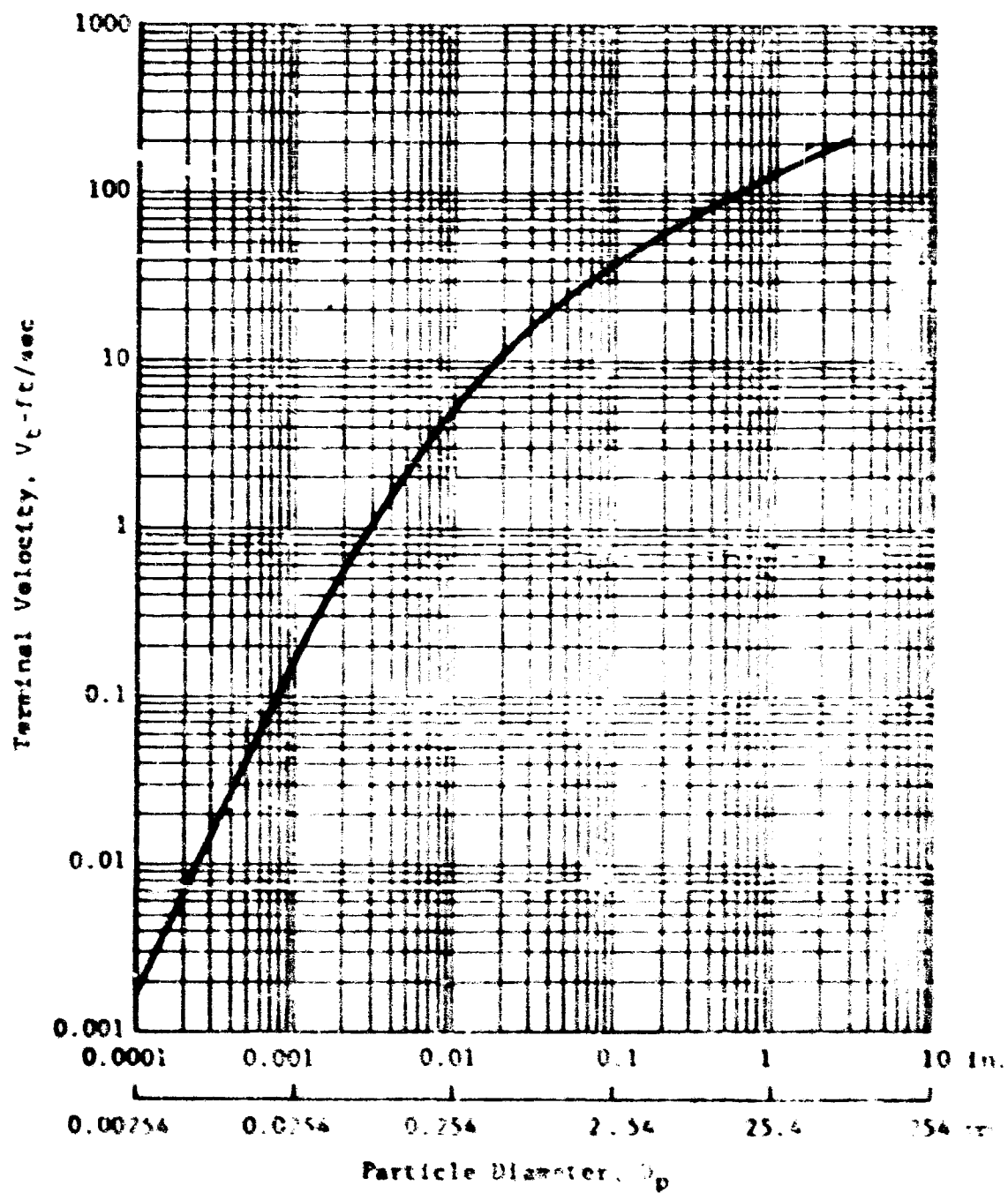
Figure 16. Variation of Terminal Velocity of Particles With Particle Diameter.

$$e_A = \frac{100}{(e_G)_{max}} \ e_G \qquad\qquad (46)$$

At each radial station, the maximum particle size distribution with height is obtained from Figure 16 where the terminal velocity is a local resultant velocity determined in Section II. A.

C. DOWNWASH SIGNATURE EFFECTS

Presented in this section is a brief analysis of the effects of rotor downwash environment on pilot's visibility, engine, ground equipment, and personnel.

1. Pilot's Visibility

One of the potential hazards of operating a V/STOL aircraft in ground proximity is the loss of pilot's visibility due to the dust cloud formation generated by the rotor downwash.

The process of seeing involves the reception of light impressions by the eye from the sighted object. These light impressions are very much dependent on the contrast between object and background, the absolute background light intensity, and the geometric angle the object extremities subtend at the eye. The relationship between these parameters has been established in Reference 19; the results directly applicable to this study have been extracted and are summarized in Figure 17.

The following analysis determines pilot visibility in terms of minimum perceivable object size for various distances from the pilot as affected by reduction of contrast and background light intensity created by the dust cloud.

Using Reference 20, the visibility reduction in terms of contrast reduction, C', due to the contaminated atmosphere is given by:
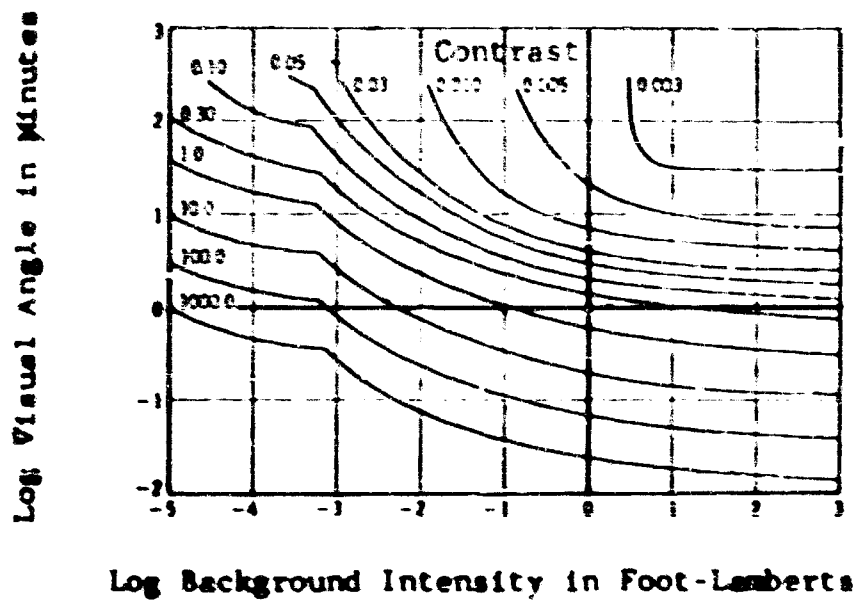
Figure 17. The Relation Between Visual Angle and Background Intensity for Test Objects of Constant Threshold Contrast.

$$c' = c\left(\frac{I_o}{I_o'}\right) T \qquad (47)$$

where the uncontaminated contrast C is given by

$$C = \frac{I_s - I_o}{I_o} \qquad (48)$$

Assuming that the background (terrain) intensity is indepen-
dent of distance and cloud density, i.e., $I_o' = I_o$, then
equation (47) reduces to

$$c' = TC \qquad (49)$$

In equation (49), the parameter T represents the light trans-
mittance which is defined as the ratio of light intensity
emitted by the object placed within the dust cloud to that
when the object is sighted in uncontaminated atmosphere.
The light transmittance T can be expressed as follows:

$$T = e^{-NA_p d} \qquad (50)$$

In the above equation, the number of particles per cubic foot
of air, N, can be obtained by assuming that all airborne
particles are equal to the mean particle size of the terrain.
Using this assumption, equation (50) can be expressed as:

$$T = e^{-\left(\frac{\rho_p d}{1.5 \ \rho_G \ D_{p\ast}}\right)} \qquad (51)$$

44

The geometric parameters which affect pilot's vision are the
cloud penetration distance (d) measured along the pilot's
line of vision to the object and the horizontal distance (S_h)
from the pilot to the object. The cloud penetration distance
(d) is determined knowing the height (size) of the sighted
object and the dust cloud geometry previously determined.
The horizontal distance (S_h) between the pilot and the object
can be obtained from basic geometry.

Thus, using the nomenclature of Figure 18, the distance (S_h)
can be expressed in terms of radial distance (r) measured
from the rotor centerline, the heading angle ψ relative to
the object, and the aircraft geometry:

$$S_h^2 = r^2 + C^2 - 2rC \cos \alpha \qquad (52)$$

where

$$C = \sqrt{A^2 + B^2} \qquad (53)$$

$$\alpha = \psi + \Psi - \beta - \sin^{-1}\left[\frac{C}{r} \sin(90-\Psi-\beta)\right] \qquad (54)$$

and

$$\beta = \tan^{-1}\left(\frac{A}{B}\right) \qquad (55)$$
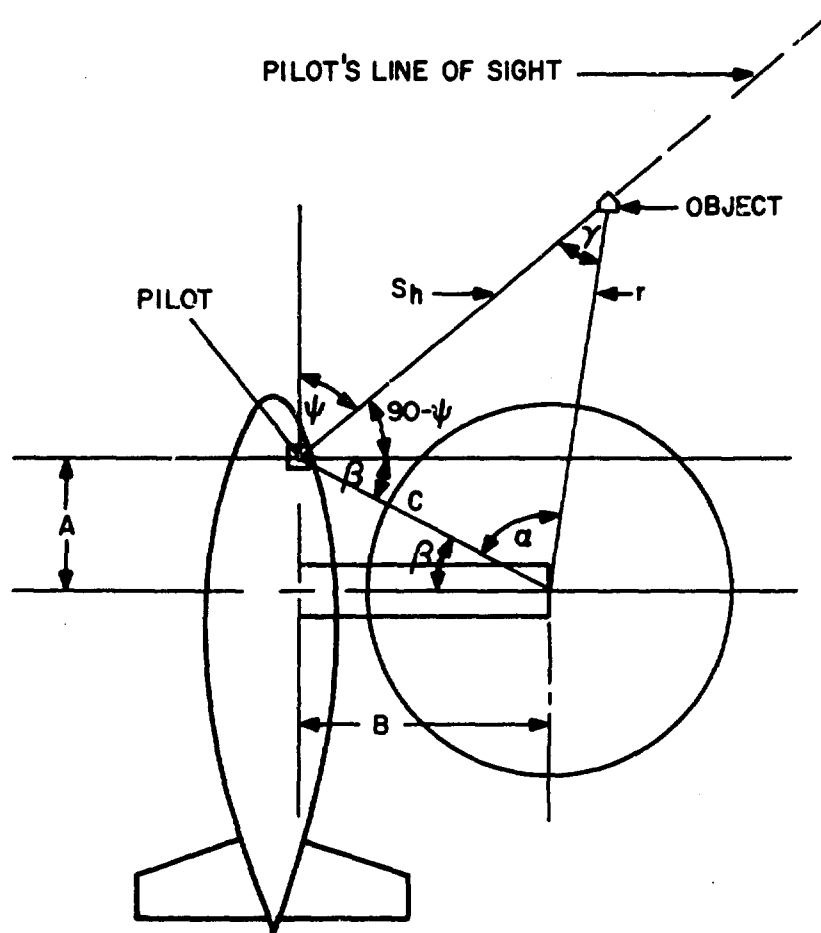
Figure 18.   Pilot's Line of Sight Relative to Vehicle.

2. Engine and Equipment Damage

The rotor downwash environment generated by high-disc-loading V/STOL aircraft can cause severe damage to aircraft components (engine), equipment, and personnel placed in the vicinity of hovering aircraft.

No specific analytical methods are available to predict the degree of such damage. However, some information on this subject was obtained from the pertinent wind tunnel and full-scale flight tests and is presented in Section III. C.

III. DOWNWASH ENVIRONMENT RESULTS FOR VARIOUS V/STOL AIRCRAFT

Although the analytical methods presented in the previous
section are completely general, the application of these
methods for predicting the downwash environment of a spe-
cific V/STOL configuration requires minor modification to
properly account for the number of lift devices, aircraft
geometry, and terrain conditions.

These methods have been used to predict the contaminant
cloud characteristics for the H-21, XC-142, X-22A, X-19A, and
XV-5A V/STOL aircraft operating over silty sand. The results
obtained for these aircraft are presented below.

A. FLOW FIELD

1. Flow Field Above Rotor Plane (Region 1)

The nondimensionalized velocity profiles of the flow field
above the rotor plane (inside and outside vortex cylinder -
Regions 1A and 1B) applicable to the H-21, XC-142, X-22A,
X-19A, and XV-5A V/STOL aircraft configuration are presented
in Figure 5. The dimensional values of the flow field for
each aircraft can be obtained by multiplying the non-
dimensional values of Figure 5 by the corresponding average
momentum velocities of the fully developed slipstream of
each aircraft and the appropriate ground effect factor given
in Figure 4.

2. Flow Field Below Rotor Plane (Region 2)

The velocity profiles below the rotor plane (Region 2)
applicable to the H-21, XC-142, X-22A, X-19A, and XV-5A
V/STOL aircraft are presented in the nondimensional form in
Figure 6. The dimensional values of the slipstream velocity
for each aircraft can be obtained by multiplying the values
of Figure 6 by appropriate average momentum value of the
induced velocity at the rotor plane.

3. Wall Jet Flow (Region 3)

Using the analytical methods developed in Section II. A. 3
and the aircraft geometric parameters listed in Table I,

48

TABLE I				
GEOMETRIC PARAMETERS OF V/STOL AIRCRAFT				
Aircraft	Gross Weight (lb)	Rotor/Prop Diameter (ft)	Disc Loading (psf)	Rotor Height With Wheels on Ground (ft)
H-21	13,000	44.0 x 2	4.28	16.0
XC-142	37,500	15.6 x 4	49.68	20 (avg)
X-22	15,800	7.0 x 4	103.0	7.5 (avg)
X-19	13,660	13.0 x 4	25.73	12.02
XV-5A	9,200	5.2 x 2	288.8	5.15
Sea-Level Conditions				

the wall jet velocity profiles have been calculated for the
selected aircraft for wheels on the ground and also for
wheels 50 feet above the ground for the XC-142 aircraft.

The results for zero wheel clearance of the selected aircraft
are presented in Figures 19 and 20, which show the wall jet
velocity distribution at the location where the wall jet begins
and at a common radial station 90 feet from the rotor center-
line, respectively. From these figures, it can be noted that
the wall jet contours for high-disc-loading aircraft are sub-
stantially lower in overall thickness than those for low-disc-
loading aircraft. It can also be seen that although a much
higher surface velocity occurs close to the high-disc-loading
aircraft, these velocities decrease more rapidly with increas-
ing radial distance than those for low-disc-loading aircraft.

Figure 21 shows the velocity profiles for the XC-142 aircraft
operating at 50 feet wheel clearance from the ground. Compar-
ing the results of Figures 19, 20, and 21 for this aircraft,

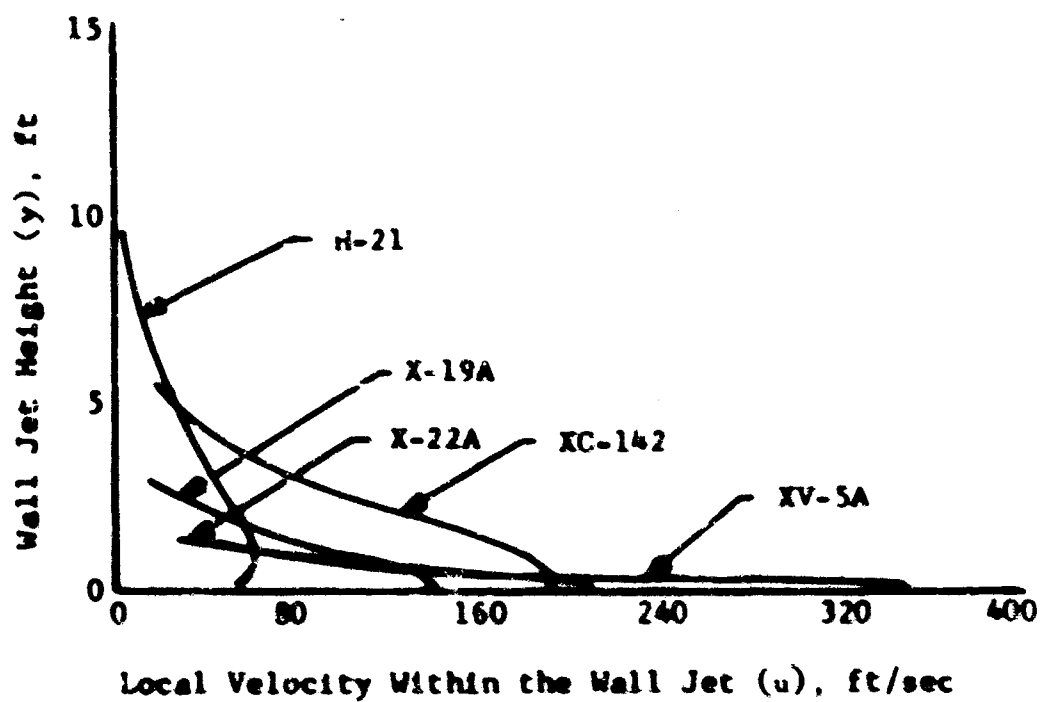Figure 19. Comparison of Wall Jet Velocity Distributions for Various Aircraft at the Start of the Wall Jet. Wheels on the Ground.
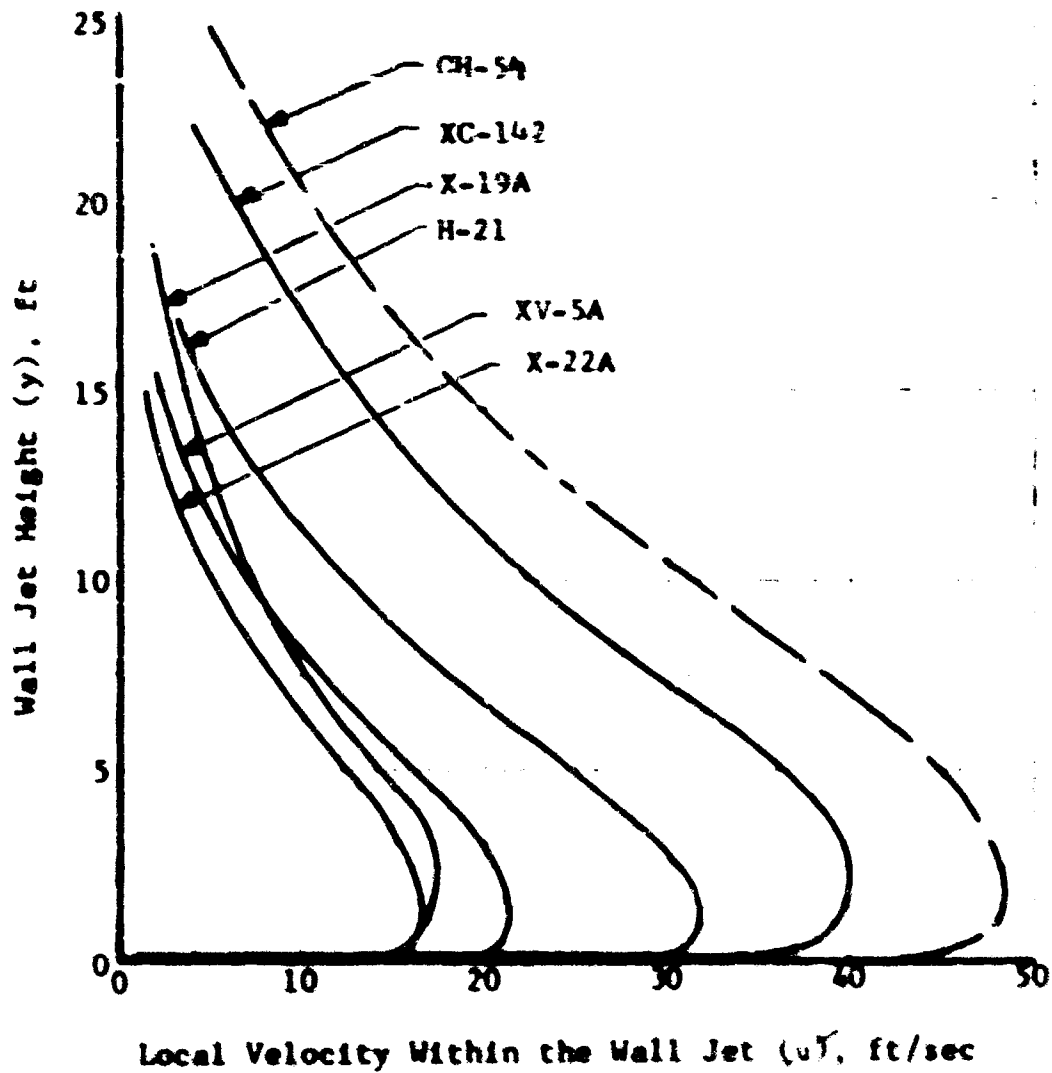
50

Figure 2C. Comparison of Wall Jet Velocity Distributions for Various Aircraft at a Common Radial Station (X = 90 Feet). Wheels on the Ground.
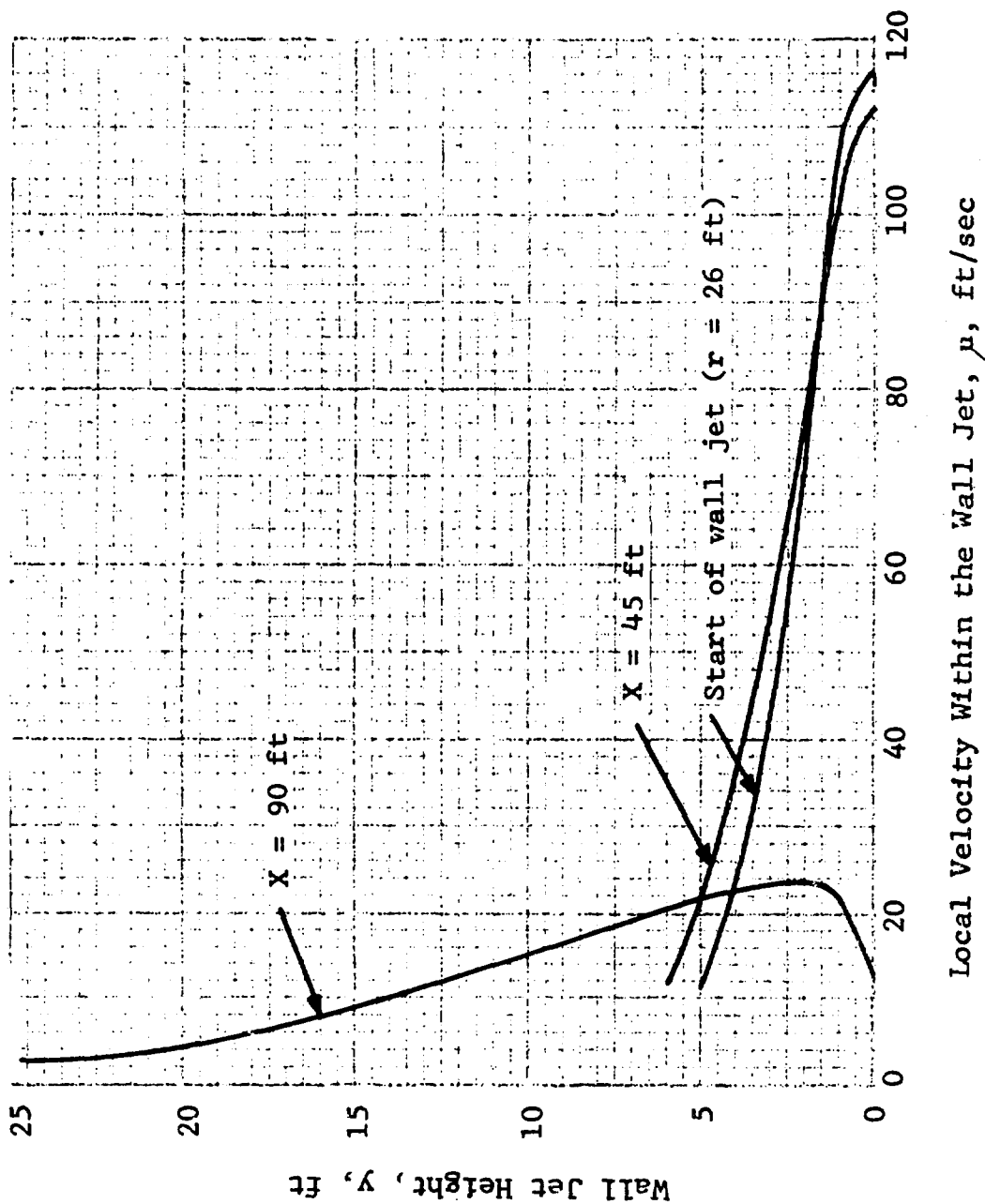
Figure 21. Wall Jet Velocity Distribution for XC-142 Aircraft at Various Radial Stations, Wheel Clearance, H_W = 50 Feet.

It can be noted that the effect of rotor height above the ground is to reduce the magnitudes of the wall jet velocities at an approximate rate of 1 percent per foot height of the corresponding wall jet velocity with wheels on the ground.

The results of Figure 19 are replotted in Figure 22 in terms of maximum surface dynamic pressure versus radial distance from the rotor centerline. This figure indicates that the maximum surface dynamic pressure at the radial location where the wall jet begins is a strong function of aircraft disc loading. This trend is not indicated at other radial locations within the wall jet.

4. **Recirculation Flow (Region 4)**

The flow recirculation area for the aircraft having four lifting devices arranged side by side and in tandem is bounded by two expanding interaction planes, one along the longitudinal and one along the lateral plane of symmetry. For these aircraft, the flow recirculation area as defined in Section II. A. 4 is comparatively small and does not warrant special analysis. Therefore, the computations of the flow field in this region were performed only for the H-21 and XC-142 aircraft and are presented in Table II. Table III presents the results for the XC-142 aircraft operating at 50 feet wheel clearance from the ground.

From the results shown in Tables II and III, it can be noted that the magnitudes of the velocities in this region are quite small (less than 9 ft/sec). Furthermore, the effect of wheel clearance (rotor height) on the magnitudes of these velocities is negligible.

5. **Flow in the Interaction Region**

The equations derived in Section II. A. 5 have been utilized to compute the horizontal and vertical velocity components in the interaction plane at distances of 45 and 90 feet. The results are presented in Figures 23 through 27 for all selected aircraft with wheels on the ground, and in Figure 28 for the XC-142 aircraft operating at 50 feet wheel clearance from the ground. It should also be noted that since the results presented in Figures 23 through 28 do not include
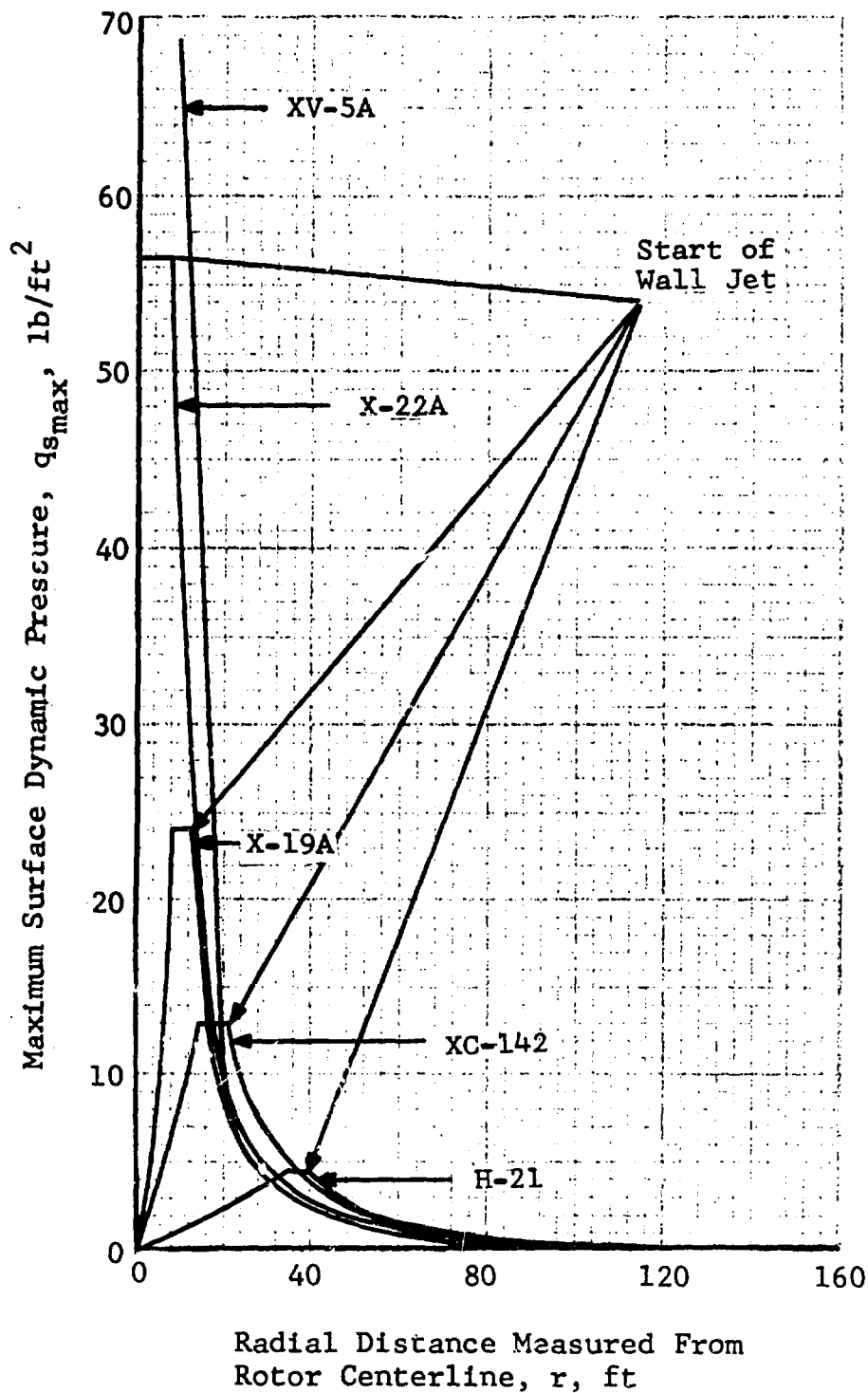
Figure 22. Variation of Maximum Surface Dynamic Pressure Along the Ground for Various Aircraft. Wheels on the Ground.

TABLE II

HORIZONTAL COMPONENTS OF THE VELOCITIES* IN THE RECIRCULATION REGION, WHEELS ON THE GROUND

(a) H-21

h, ft measured from rotor plane	X=50 ft U_X	X=60 ft U_X	X=70 ft U_X	X=80 ft U_X	X=90 ft U_X
0	2.6	3.88	2.84	2.18	1.72
2.5	4.4	2.94	1.96	1.4	0.94
5	3.26	2.04	1.06	0	0
8	1.86	.92	0		
10	0.94	0			
12	0				

(b) XC-142

h, ft measured from rotor plane	X=50 ft U_Y	X=60 ft U_Y	X=70 ft U_Y
0	9.2	5.45	3.66
2	7.6	4.36	2.74
4	6.1	3.3	1.83
6	4.6	2.1	.914
8	3.0	1.07	0
10	1.5	0	
12	0		

*Velocities in feet per Second

TABLE III
HORIZONTAL COMPONENTS OF THE VELOCITIES* IN THE RECIRCULATION REGION - H_H = 50 Feet

XC-142

h, ft measured from rotor plane	X=50 ft U_Y	X=75 ft U_Y	X=100 ft U_Y	X=125 ft U_Y
0	9.46	3.18	1.62	0.99
10	7.88	2.54	1.21	0.66
20	6.31	1.91	0.81	0.33
30	4.73	1.27	0.40	0
40	3.15	0.64	0	
50	1.58	0		
60	0			

*Velocities in Feet Per Second

Figure 23. Horizontal and Vertical Velocity Components Along the Interaction Plane for the H-21 Aircraft. Wheels on the Ground.

Figure 24. Horizontal and Vertical Velocity Components Along Interaction Plane for the XC-142 Aircraft. Wheels on the Ground.

Figure 25. Horizontal and Vertical Velocity Components Along Interaction Plane for the X-22A Aircraft. Wheels on the Ground.
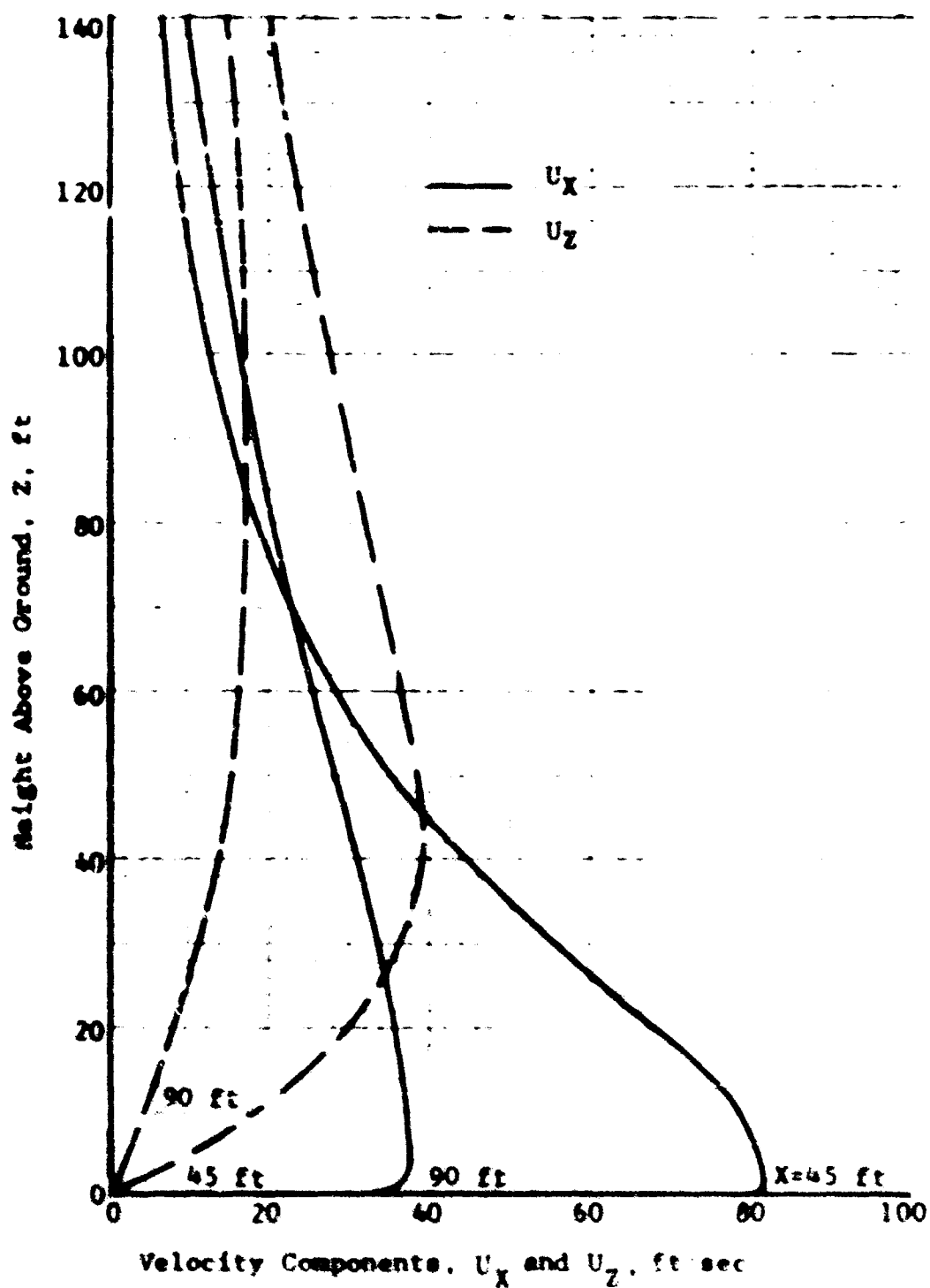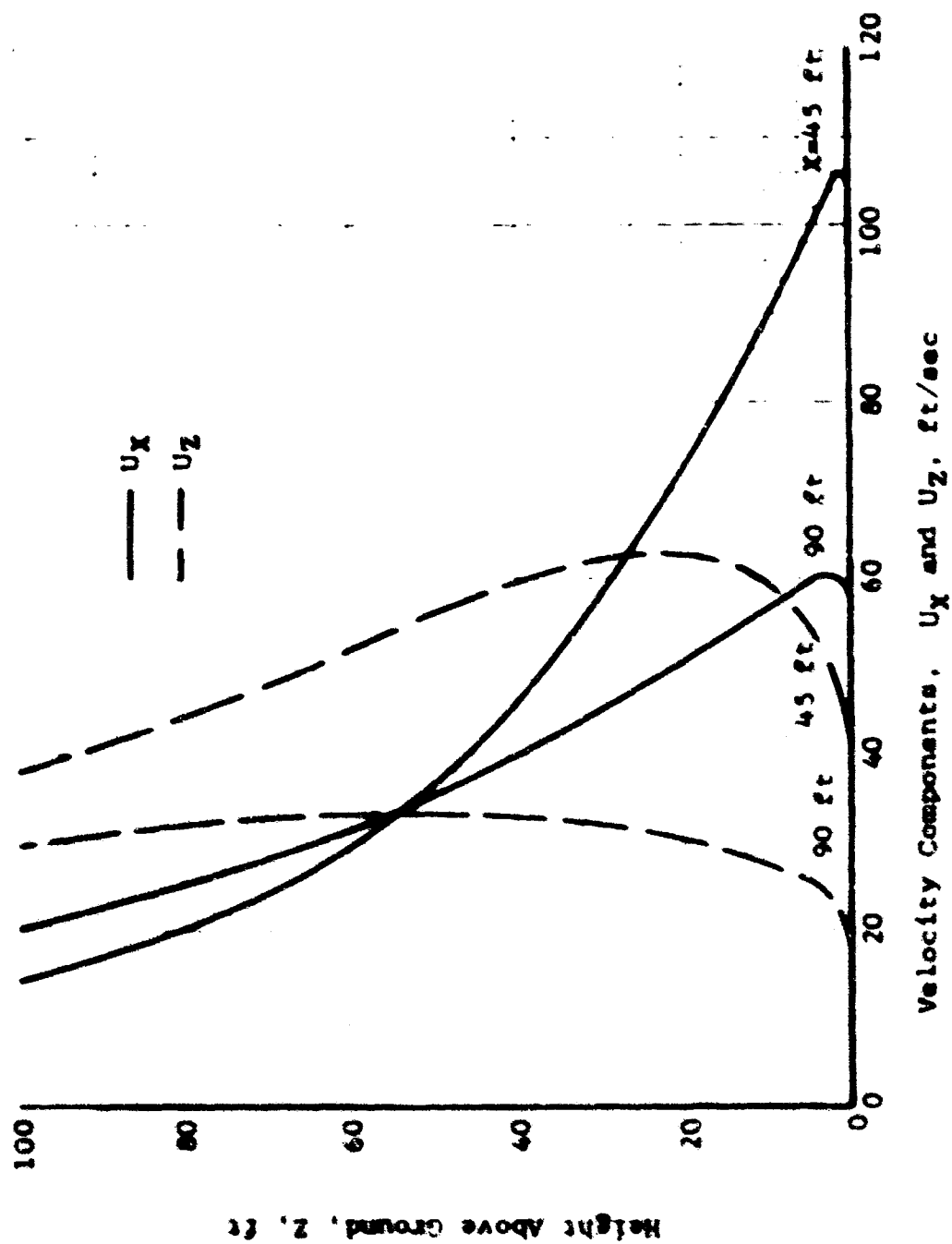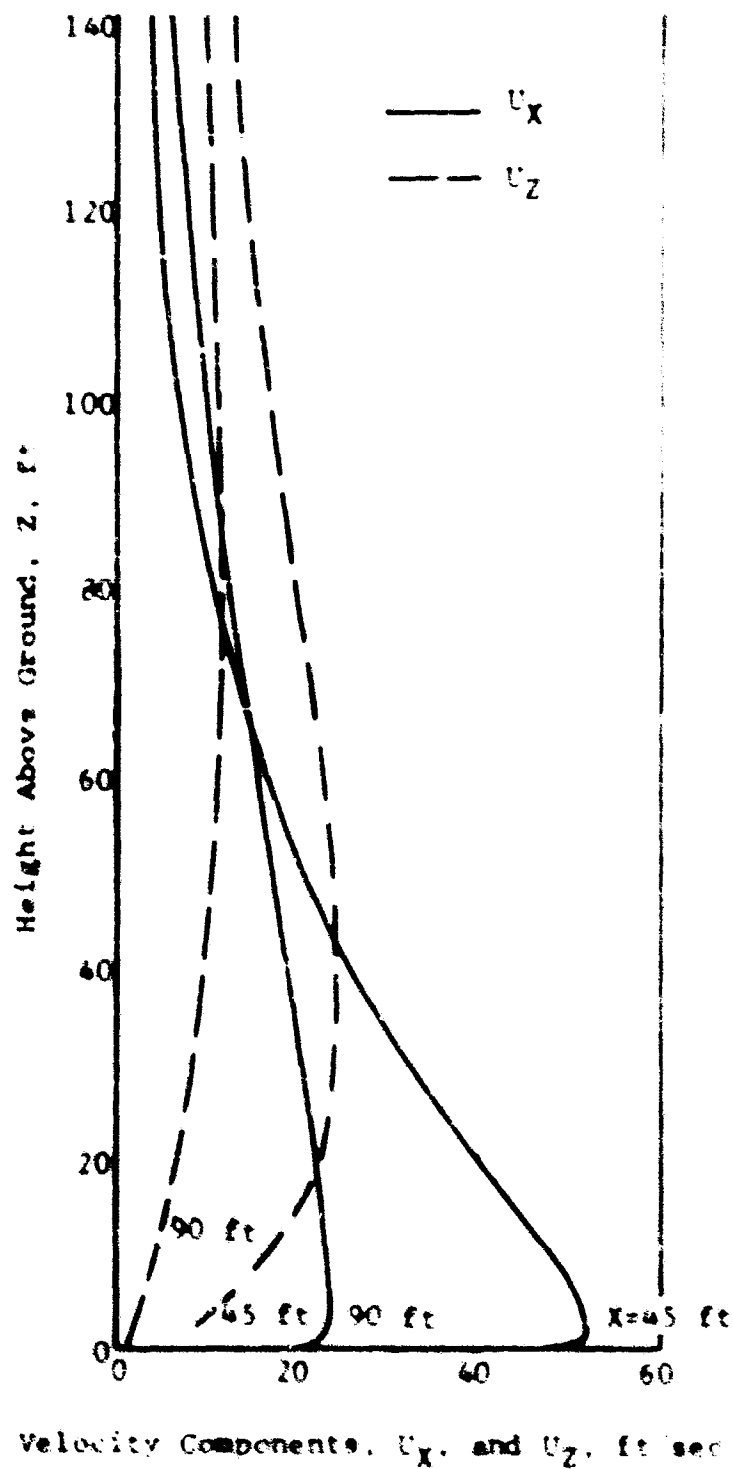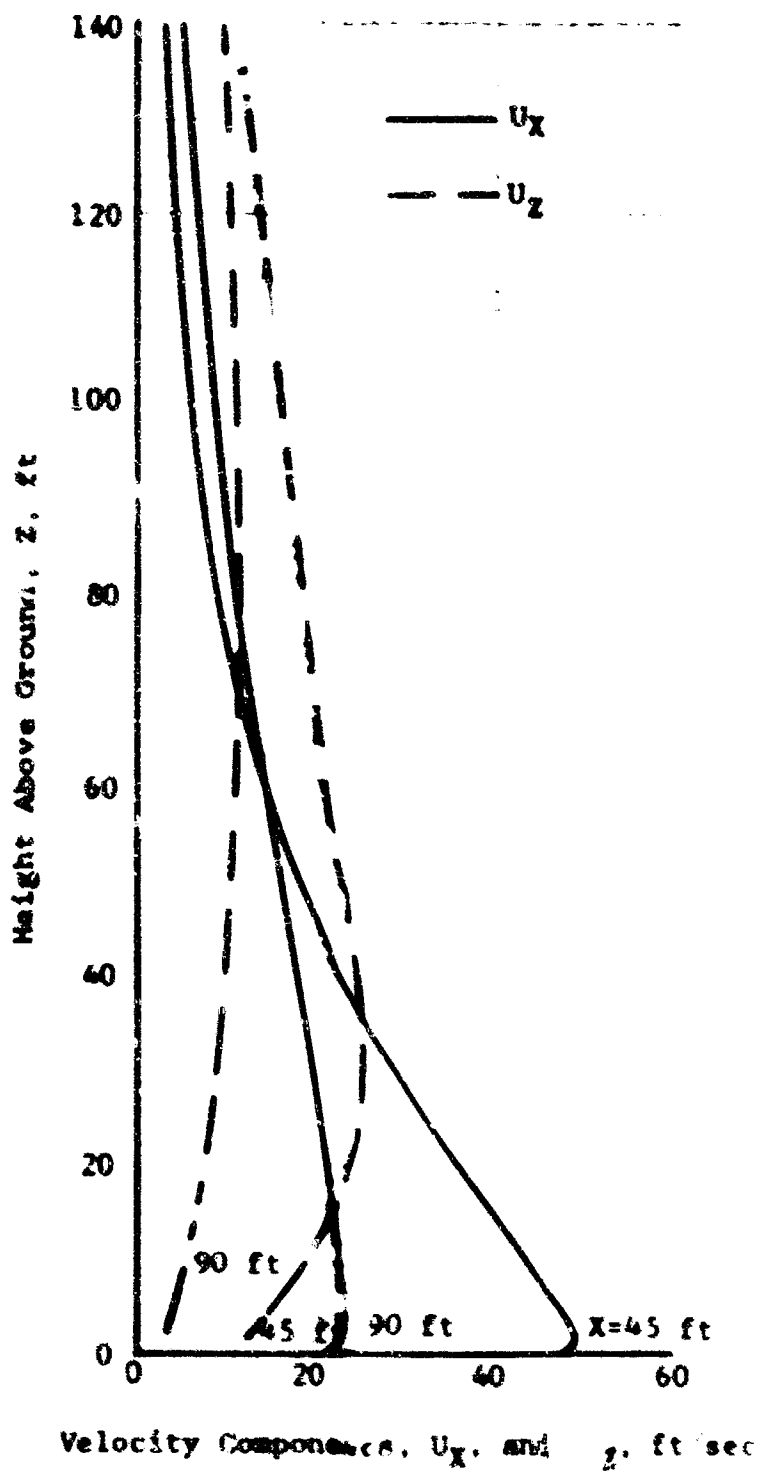
Figure 26. Horizontal and Vertical Velocity Components Along Interaction Plane for the X-19A Aircraft. Wheels on the Ground.

Figure 27. Horizontal and Vertical Velocity Components Along Interaction Plane for the XV-5A Aircraft. Wheels on the Ground.
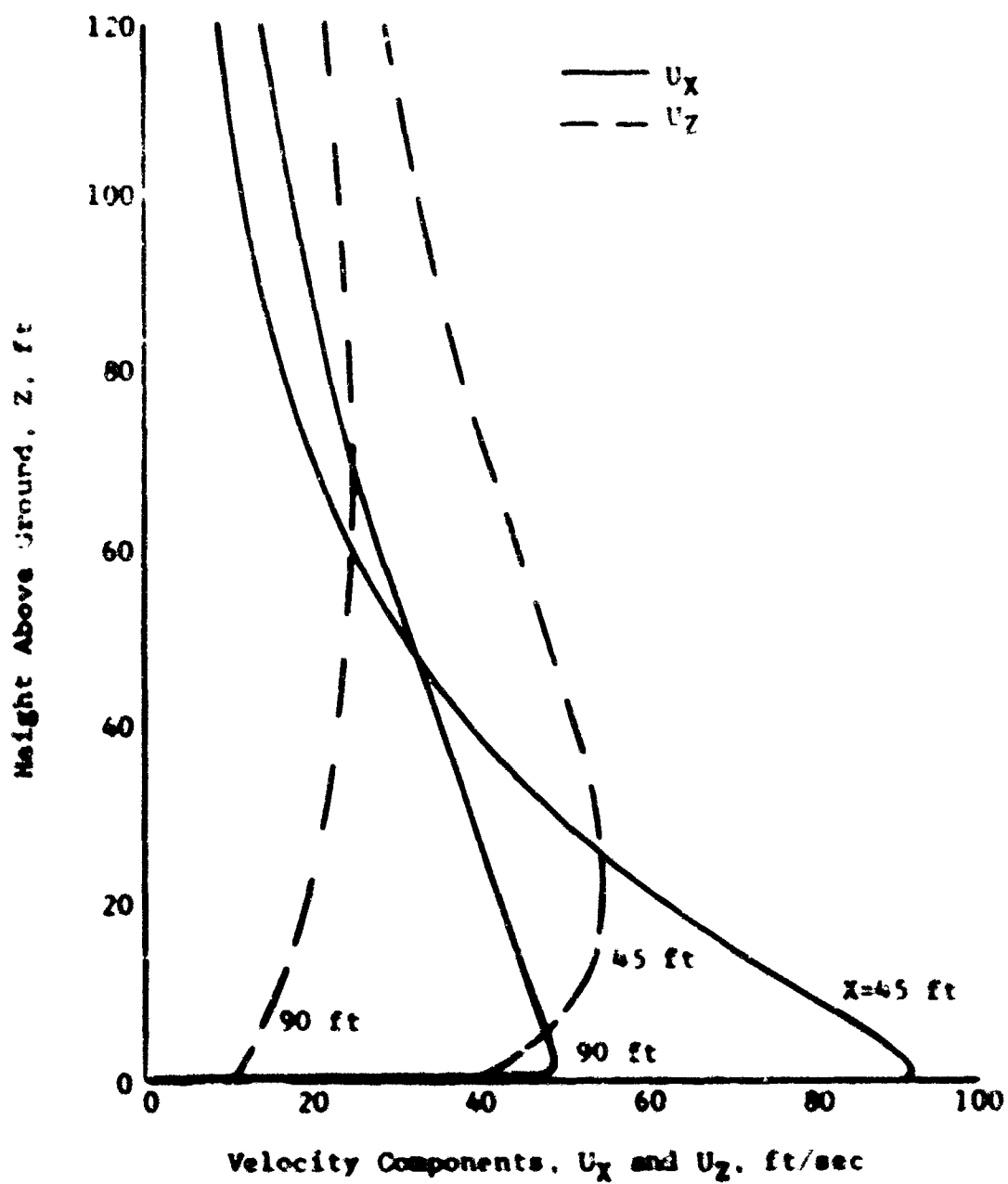
61

Figure 28. Horizontal and Vertical Velocity Components Along
Interaction Plane for the XC-142 Aircraft,
$H_w = 50$ Feet.

62

air viscosity effects, the calculated values represent upper
bounds of the velocities to be expected in this region.

6. <u>Contour Plots of Maximum Surface Dynamic Pressure</u>

It is convenient to combine the velocity results computed in
Region 3 (Wall Jet Region) and Region 5 (Interaction Plane
Region) for the selected aircraft in the form of contour
plots of the maximum surface dynamic pressure along the
ground. Such comparative contour plots obtained for the
H-21, XC-142, X-22A, X-19A, and XV-5A aircraft with wheels
on the ground are presented in Figures 29, 30, 31, 32, and
33, respectively. Figure 34 shows the results for the
XC-142 aircraft operating at 50 feet wheel clearance from
the ground.

From these figures, it can be noted that along the inter-
action plane of two rotor configurations, higher maximum
dynamic pressures are generally indicated than those of a
single jet configuration. This is readily apparent in
regions far from the aircraft center. Near the aircraft,
however, the flow in the interaction plane is nearly vertical;
hence, the horizontal component of the dynamic pressure shown
in the contour plots is smaller than that for an equivalent
single jet.

Furthermore, as was previously noted, the dynamic pressure
along the ground in the wall jet region for a low disc
loading aircraft is relatively low, but is persists at much
greater distances as compared to high disc loading aircraft
of equivalent gross weight.

B. <u>DOWNWASH SIGNATURES</u>

1. <u>Cloud Size and Shape</u>

The radial boundary (R_c) and height (H_c) of the dust clouds
for the selected V/STOL aircraft were computed utilizing
techniques developed in Section II. B. 1. The details of the
dust cloud shape were established utilizing good engineering
judgement based on the actual observations and recorded film
data of a variety of V/STOL aircraft operating in dust
environment. The consistency of the ground terrain considered
for this study is loose silty sand found at Phillips Drop Zone

63

q_s/q_N	q_s
0.2	0.86
0.4	1.71
0.8	3.42

Figure 29. Contour Plots of Maximum Surface Dynamic
Pressure Along the Ground for the H-21 Aircraft.
Wheels on the Ground.

64

Figure 30. Contour Plots of Maximum Surface Dynamic
Pressure Along the Ground for the XC-142
Aircraft. Wheels on the Ground.

Figure 31. Contour Plots of Maximum Surface Dynamic Pressure Along the Ground for the X-22A Aircraft. Wheels on the Ground.
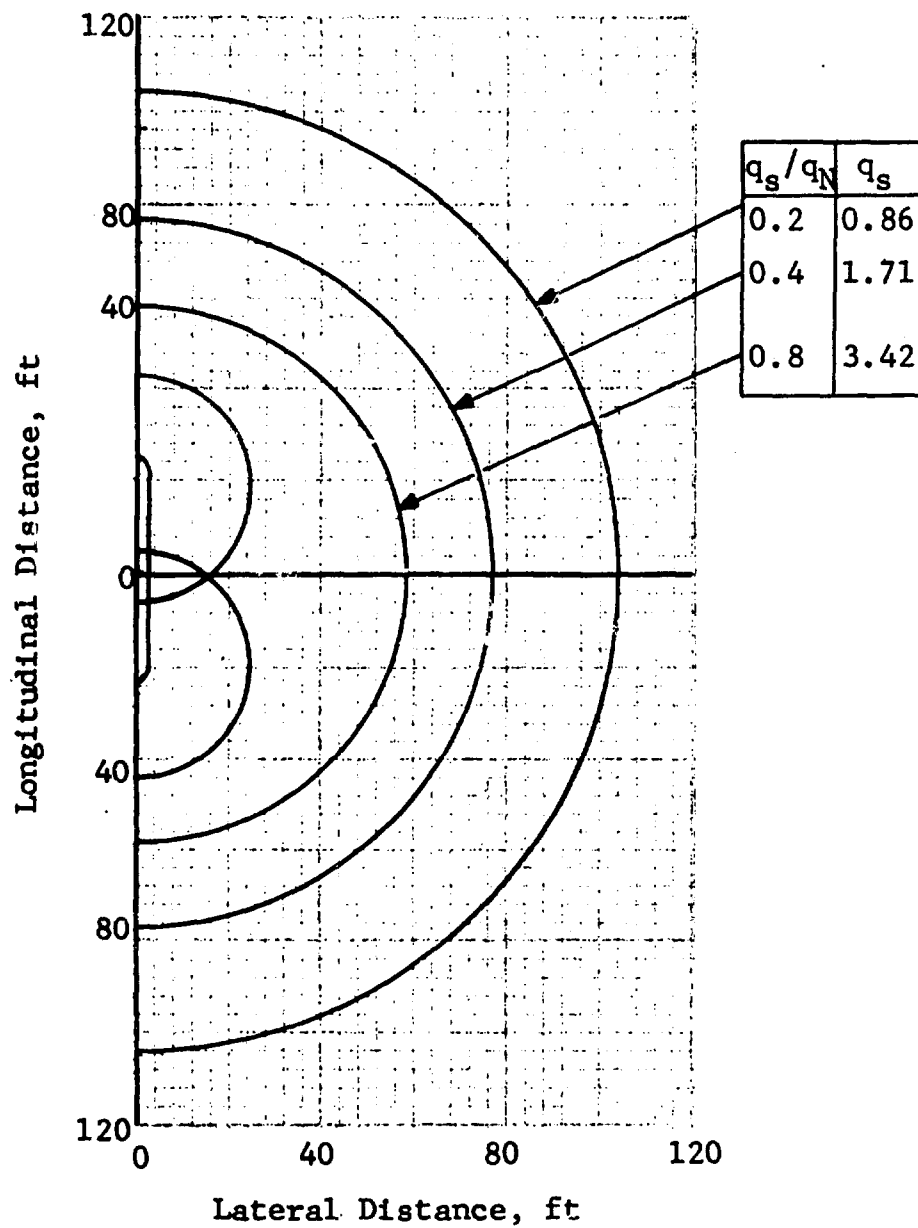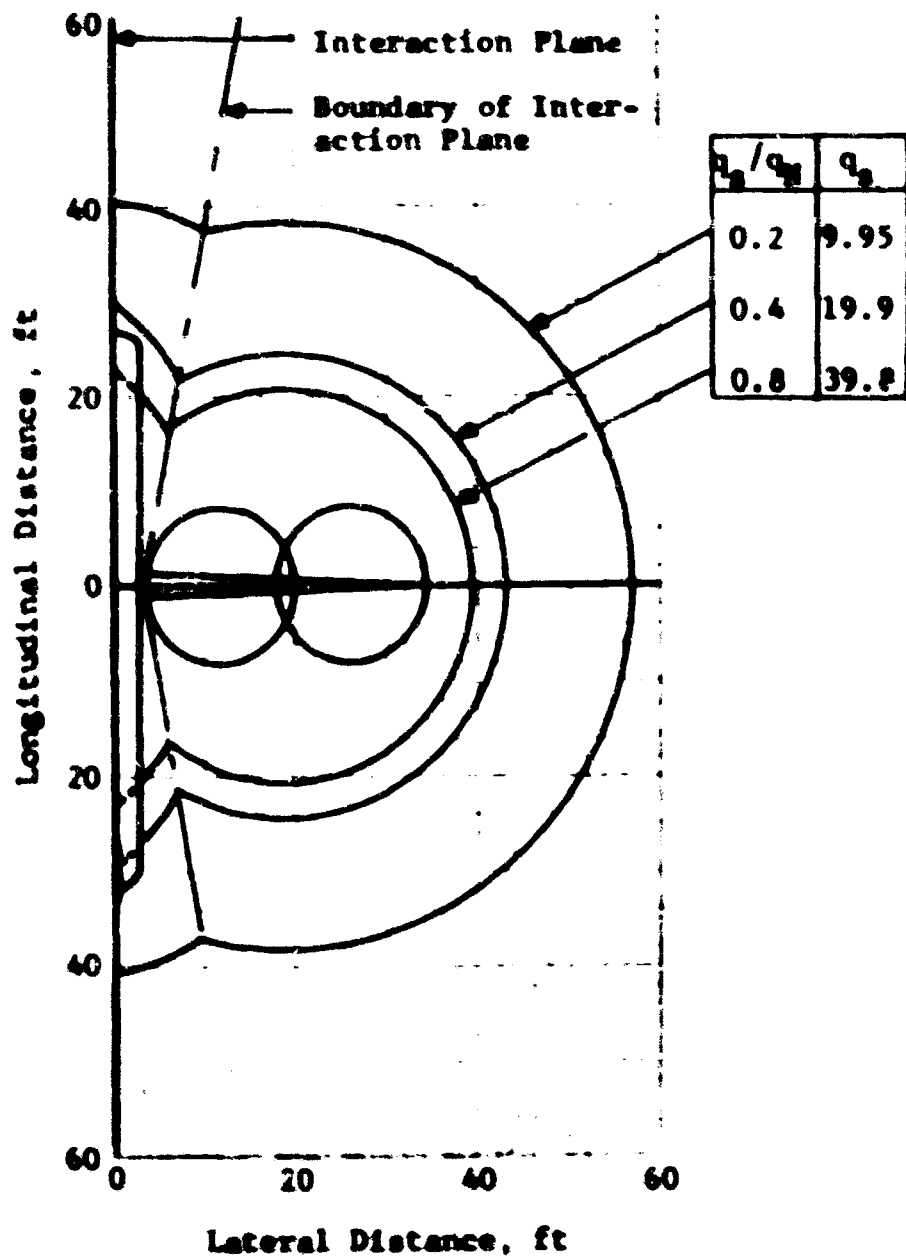
Figure 32. Contour Plots of Maximum Surface Dynamic Pressure Along the Ground for the X-19A Aircraft. Wheels on the Ground.
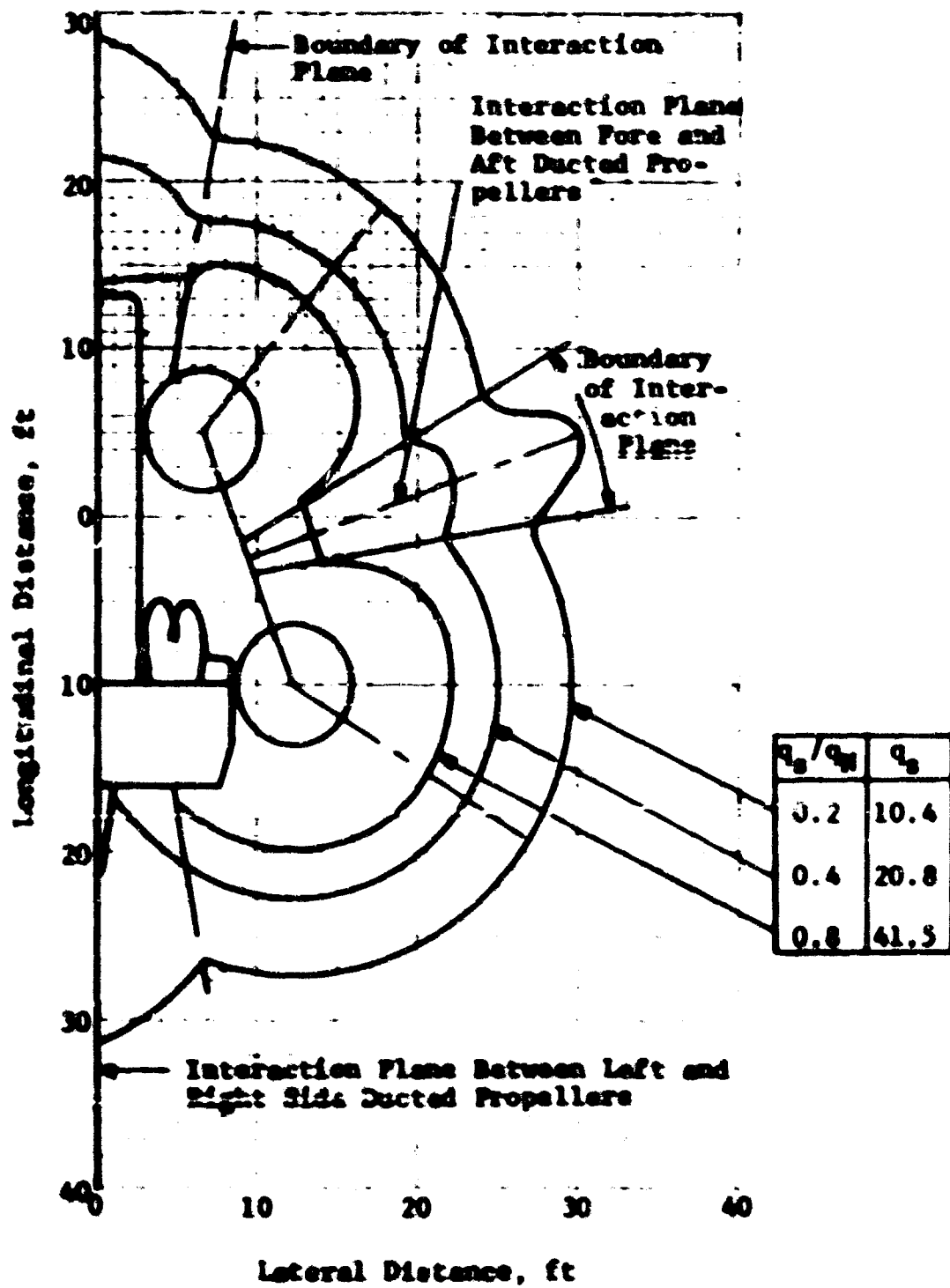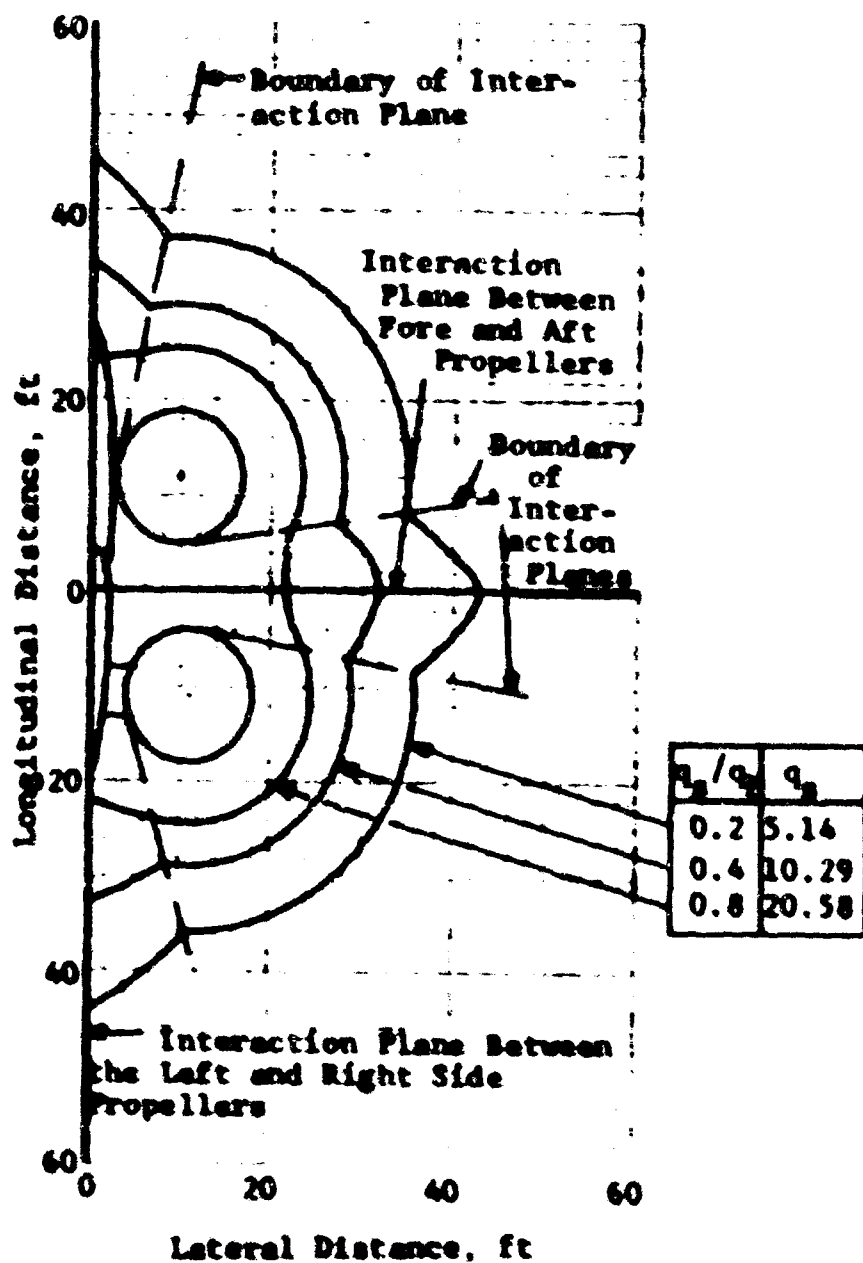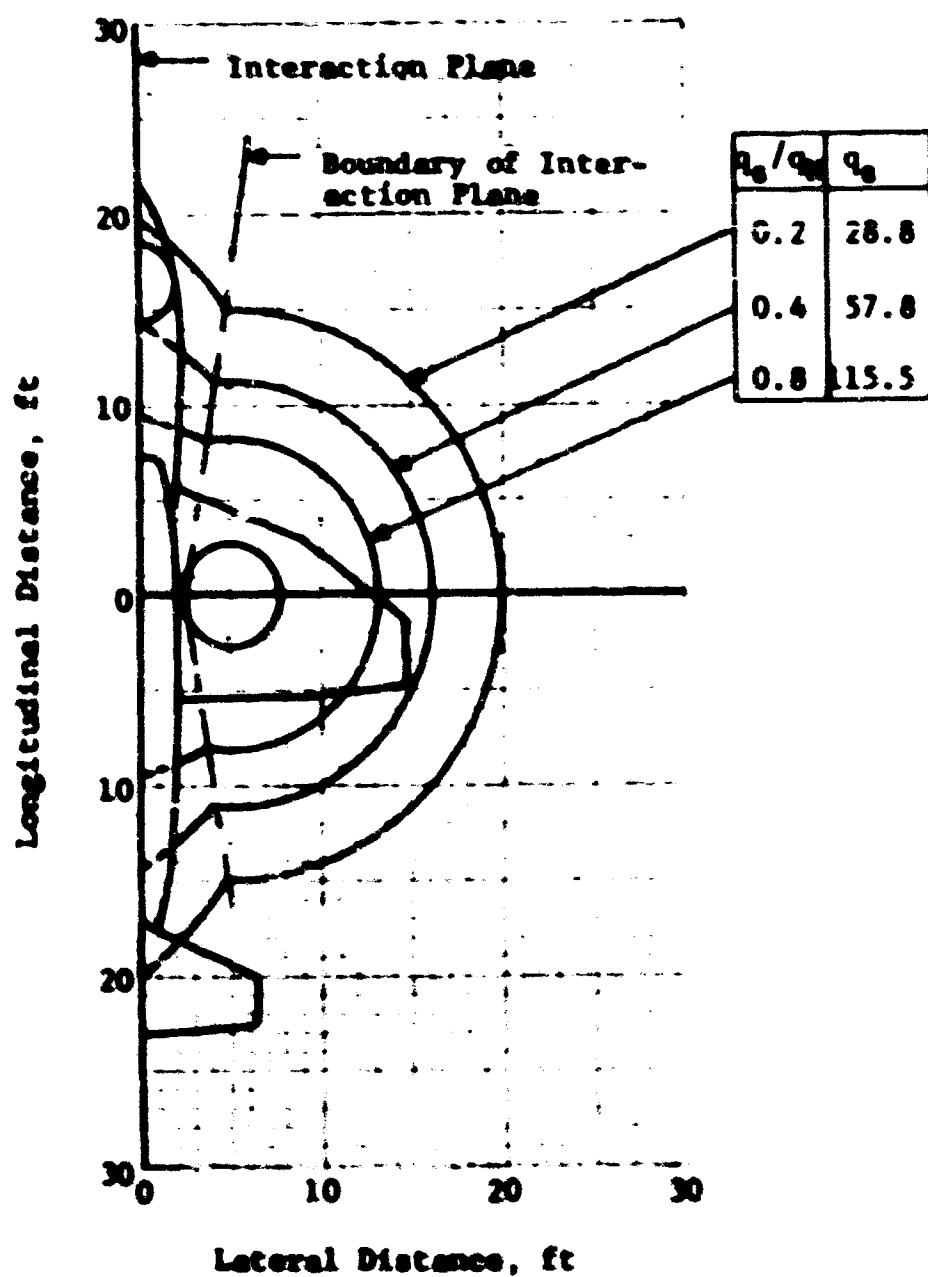
Figure 33. Contour Plots of Maximum Surface Dynamic Pressure Along the Ground for the XV-5A Aircraft. Wheels on the Ground.
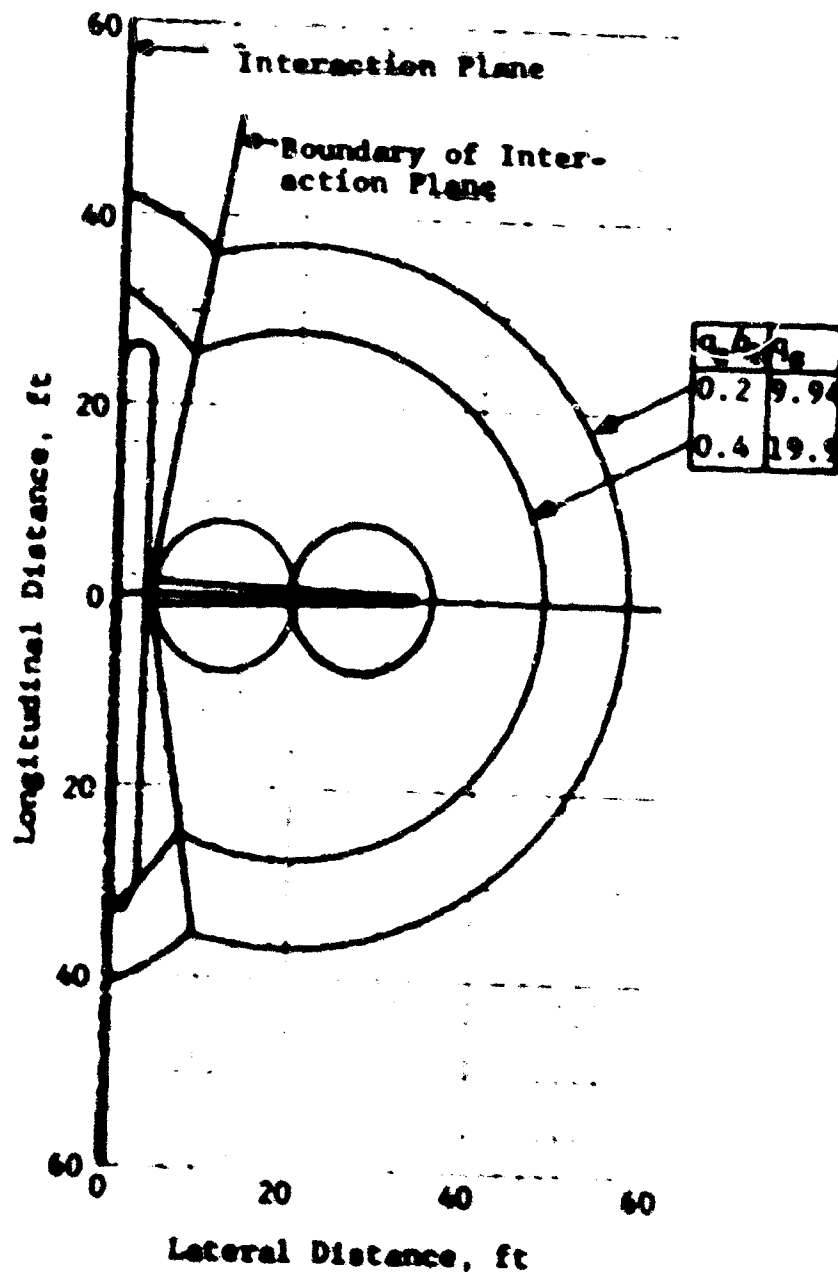
Figure 34. Contour Plots of Maximum Surface Dynamic Pressure Along the Ground for the XC-142 Aircraft, H_y - 50 Feet.

of Yuma Proving Grounds. The ground sample selected for this study and presented in Figure 35 shows ground particle size distribution by weight. Additional information on the ground sample is presented in the appendix.

Figures 36, 37, 38, and 40 show the dust clouds predicted for the H-21, XC-142, X-22A, X-19A, and XV-5A aircraft, respectively. These figures present the cloud sizes and shapes along both longitudinal and lateral planes for each aircraft for zero wheel clearance. Figure 41 shows the corresponding results for the XC-142 aircraft operating at 50 feet wheel clearance from the ground.

For multirotor configurations, one or both of these planes is the interaction plane. Figures 36 through 41 clearly indicate the asymmetry of the cloud shapes in the two planes. Film data such as those obtained from the test program reported in Reference 15 indicate that the cloud shape resembles that of a torus, or a doughnut, with its center at the center of the aircraft.

In order to obtain a better indication of the effects of aircraft parameters on dust cloud size, the results of Figures 36 through 40 are cross-plotted in Figures 42 and 43, which show the variation of maximum radial and vertical cloud sizes as a function of the dynamic pressure of a fully developed slipstream for each aircraft. It can be noted from these figures that for approximately constant gross weight (e.g., CH-47B, CH-54, and XC-142 aircraft), both the maximum dust cloud radius and height slightly decrease with an increase in disc loading. Furthermore, the maximum dimensions of the dust cloud increase appreciably with an increase of aircraft gross weight (compare H-21 or X-22 data with XC-142 data).

These figures also present the available test data obtained from the films of References 15 and 21 and the unpublished test data obtained at Edwards Air Force Base for the selected aircraft. Incidentally, good correlation can be noted between the predicted cloud sizes and those obtained from the films.

The effect of rotor height on cloud sizes can be obtained by comparing the results of Figure 37(a) (zero wheel clearance)
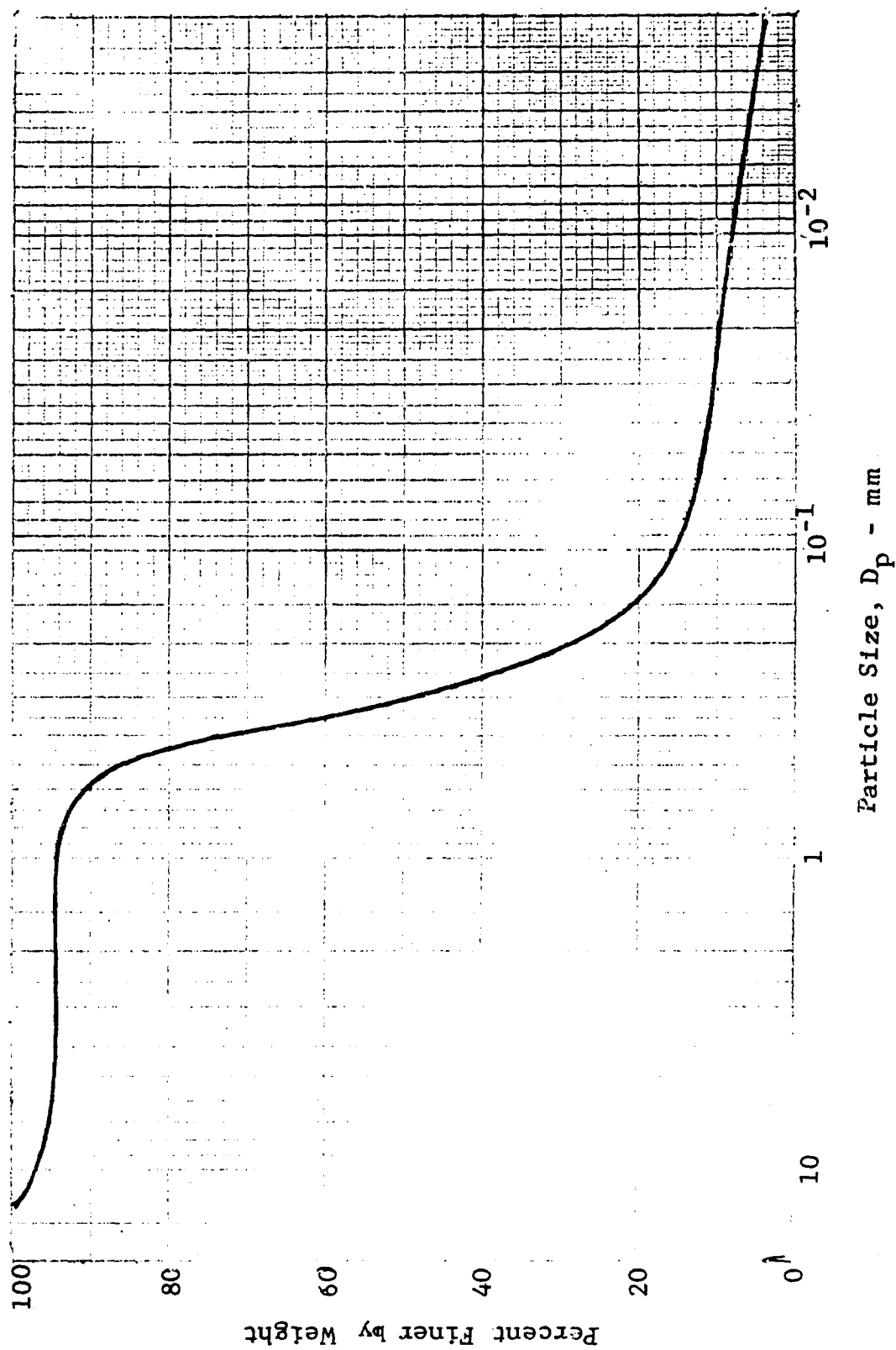
Figure 35. Ground Sample Particle Size Distribution.

Particle Size, D_p - mm

Percent Finer by Weight

71
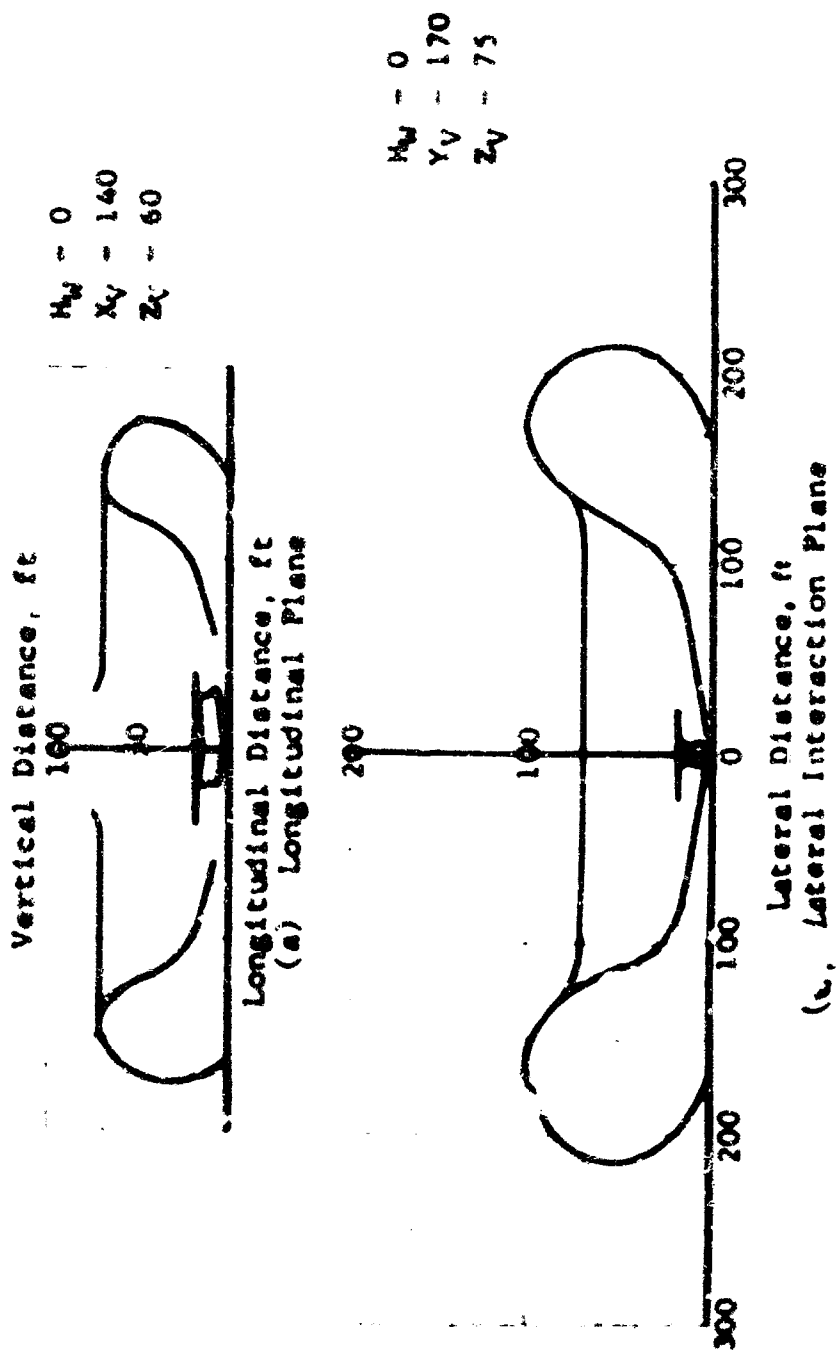
Figure 36. Dust Cloud Size and Shape for the H-21 Helicopter.
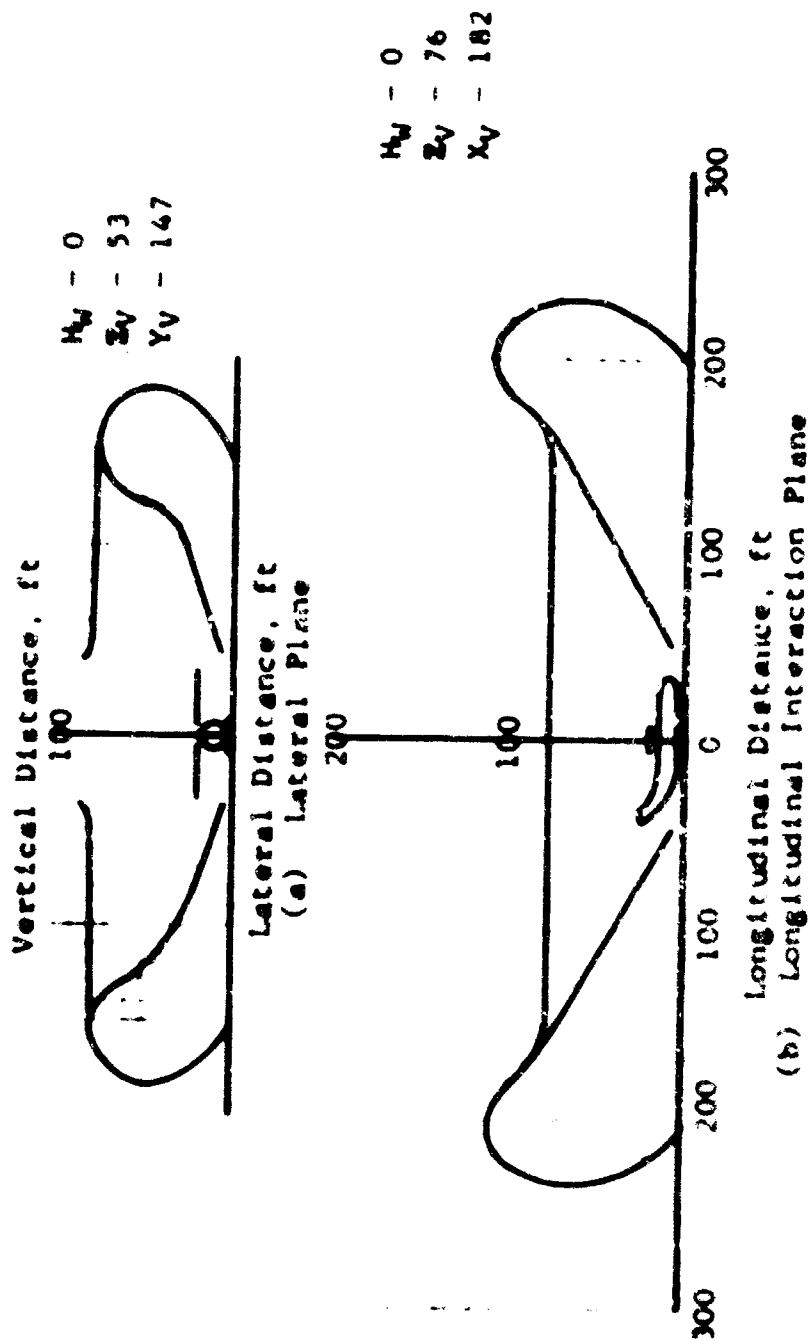
Figure 37. Dust Cloud Size and Shape for the XC-142 Aircraft.

73
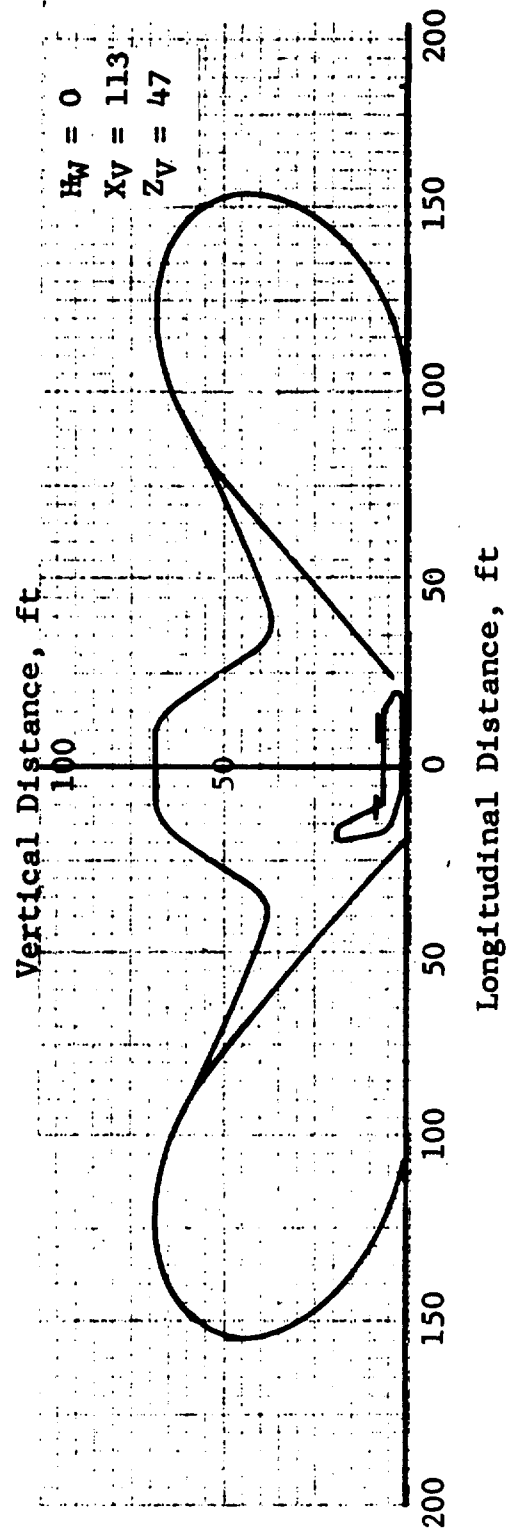
Figure 38. Dust Cloud Size and Shape for the X-22A Interaction Plane.

74

Vertical Distance, ft

$H_V = 0$
$X_V = 110$
$R_V = 46$

Longitudinal Distance, ft
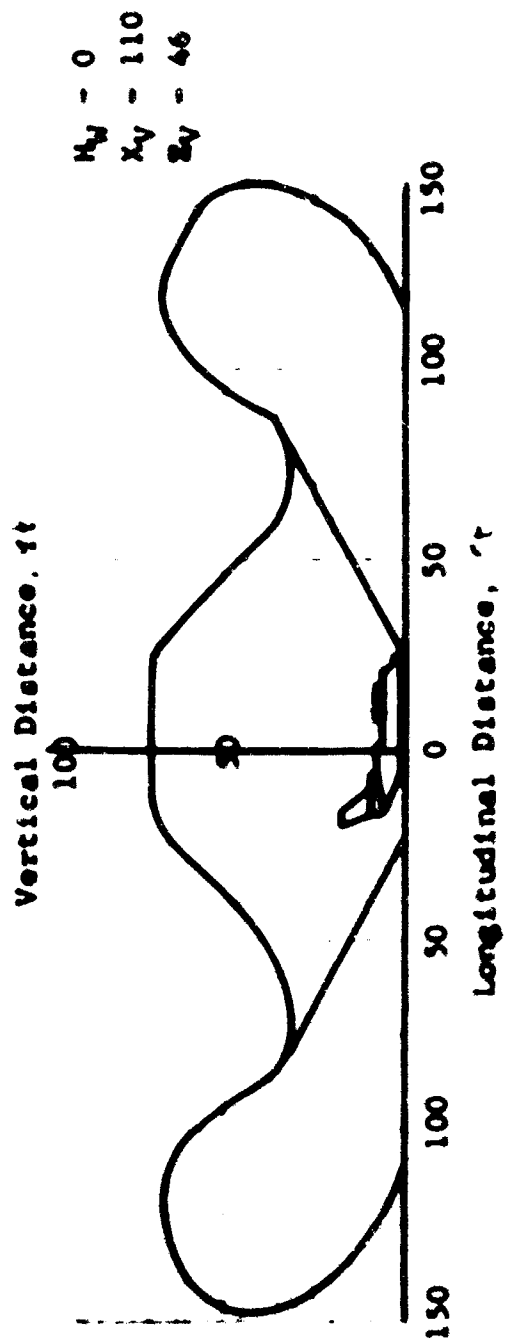
Figure 35. Dust Cloud Size and Shape for the X-19A Interaction Plane.

Vertical Distance, ft

Lateral Distance, ft
(a) Lateral Plane

Longitudinal Distance, ft
(b) Longitudinal Interaction Plane
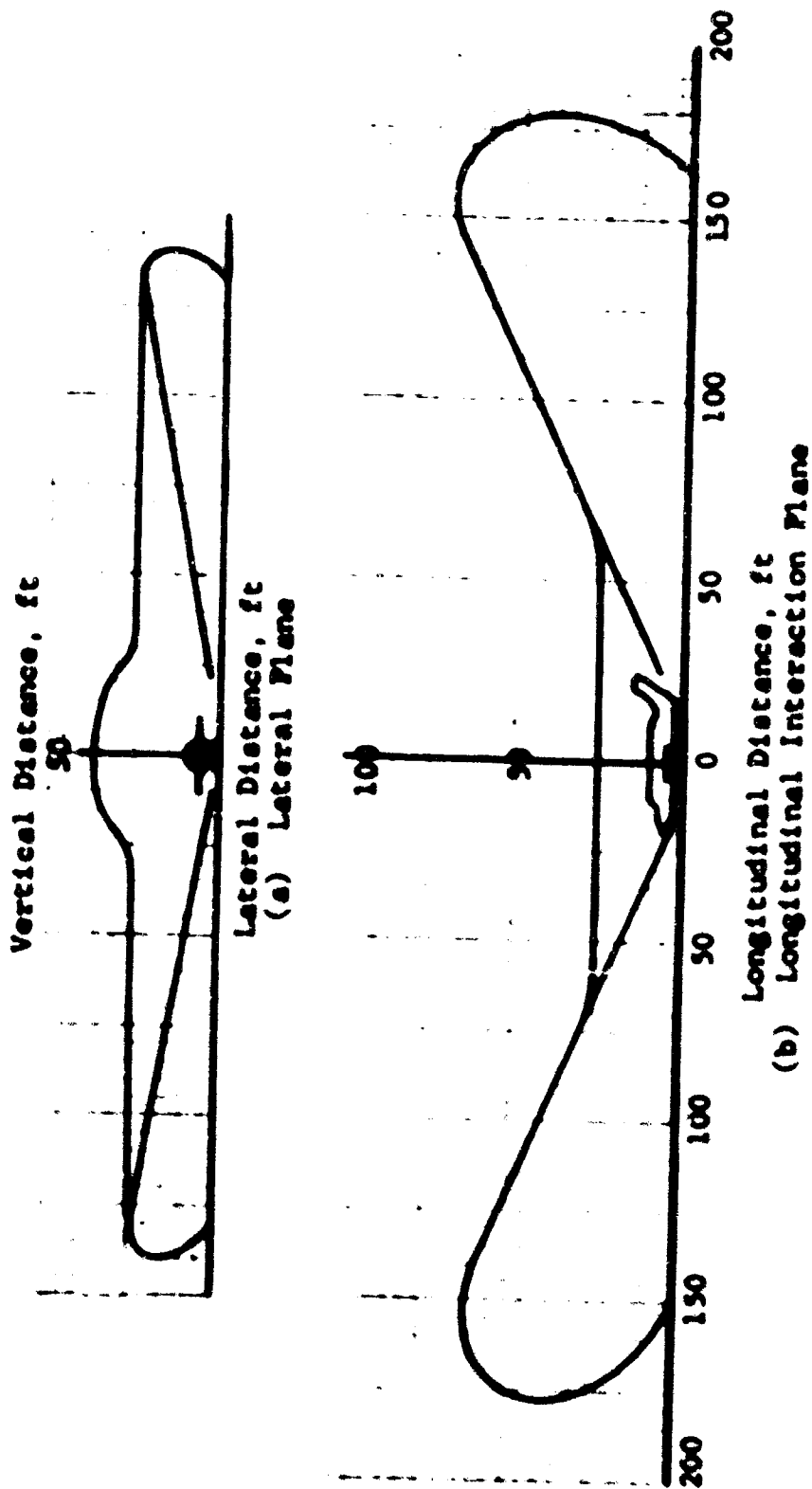
Figure 40. Dust Cloud Size and Shape for the XV-5A Aircraft.
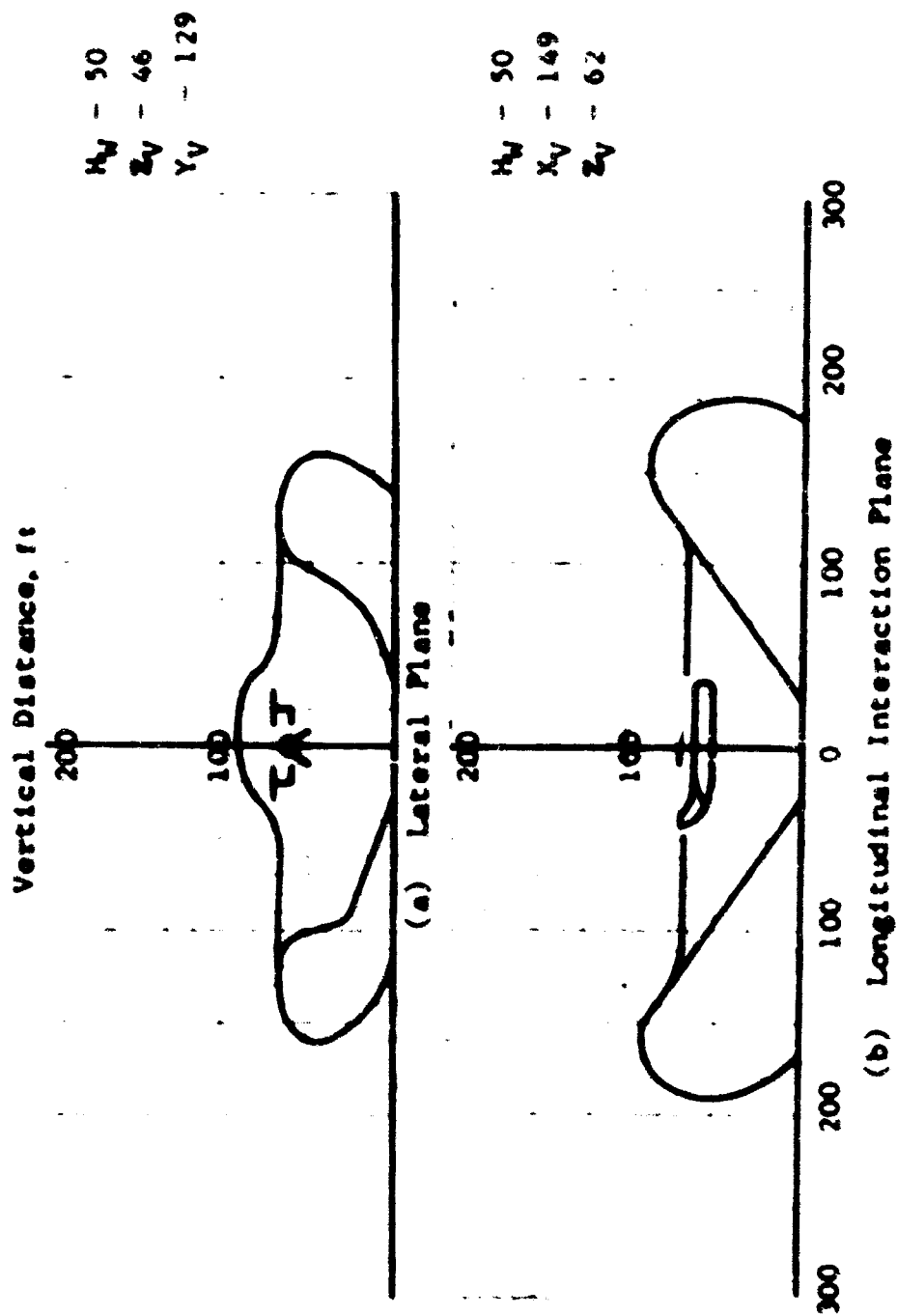
Figure 41.   Dust Cloud Size and Shape for the XC-142 Aircraft. H_W - 50 Feet.
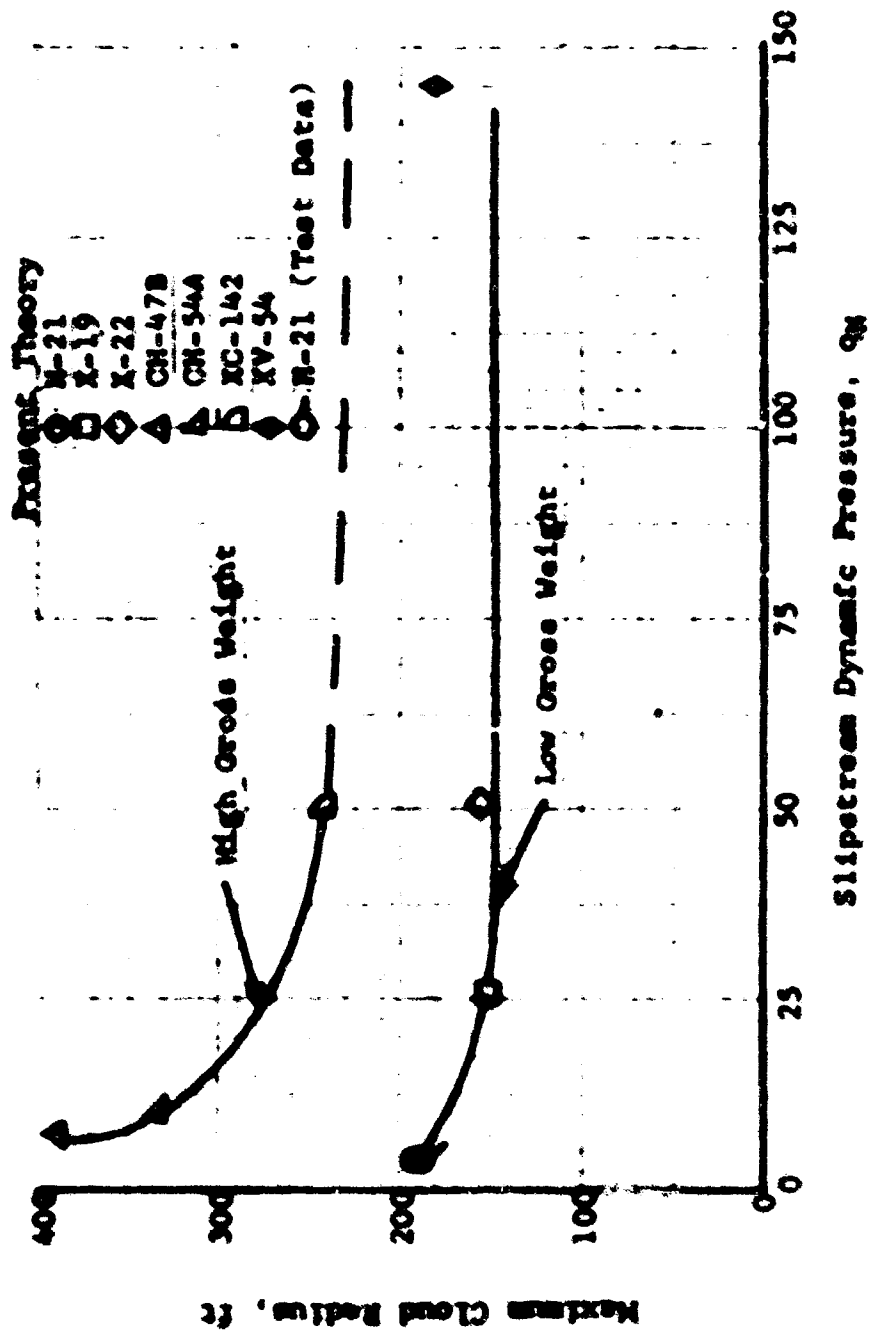
Figure 42. Maximum Boundary of Cloud versus Slipstream Dynamic Pressure for Various Aircraft.
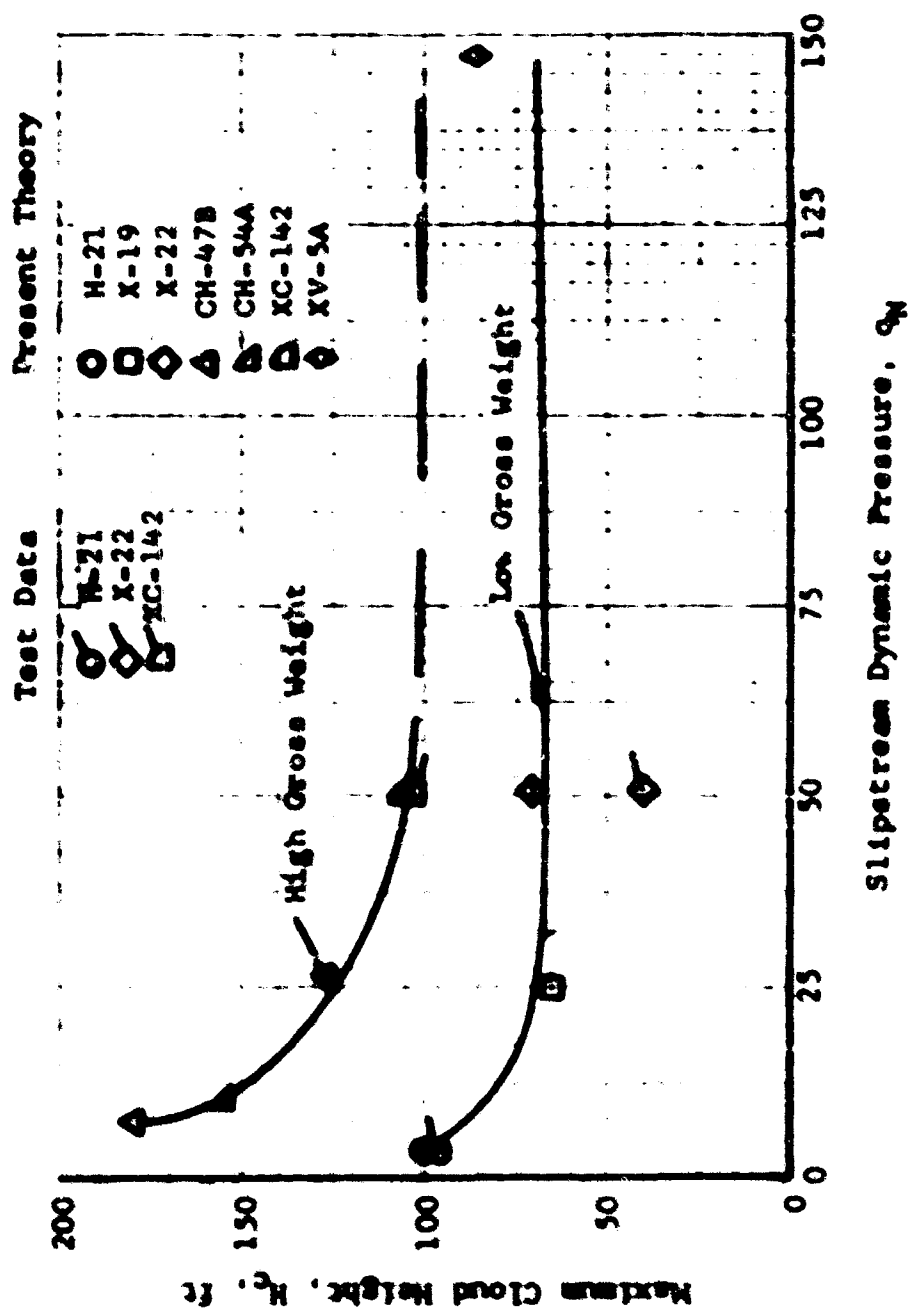
Figure 43. Maximum Cloud Height versus Slipstream Dynamic Pressure for Various Aircraft.

79

with Figure 41 (50 feet wheel clearance) for the XC-142
aircraft. It can be noted from these figures that for high
disc loading aircraft (such as the XC-142), 25 percent
reduction in cloud height and about 17 percent reduction in
cloud radius is indicated for a 50 foot increase in wheel
clearance from the ground.

2. Cloud Content

    a. Particle Density Distribution

        (1) Far-Field Density Distribution

            The far-field particle density distribution for
            the selected V/STOL aircraft at two radial
            locations, X = 45 feet and X = 90 feet, are
            presented in Figures 44 through 49. These
            results were obtained by first computing mass
            flow rate distribution and local velocities
            within the dust cloud using analytical tech-
            niques developed in Section II. Equation (45)
            was then applied to compute the corresponding
            density distribution. This analytical tech-
            nique was checked against the test data obtained
            for the H-21 helicopter operating over desert
            sand. A comparison of the theoretical results
            with test data is presented in Figure 44, which
            shows a good correlation of the present theory
            with test.

            From Figures 44 through 49, it can be noted that
            for a constant radial location, the particle
            density increases with a decrease in vertical
            distance from the ground.

            Furthermore, for the radial stations closer to
            the rotor centerline (X = 45 feet), a greater
            density decay rate is indicated with height
            from the ground as compared to that for larger
            radial stations (X = 90 feet).

            The effect of rotor height above the ground on
            particle density distribution for the XC-142
            aircraft can be seen by comparing Figure 45
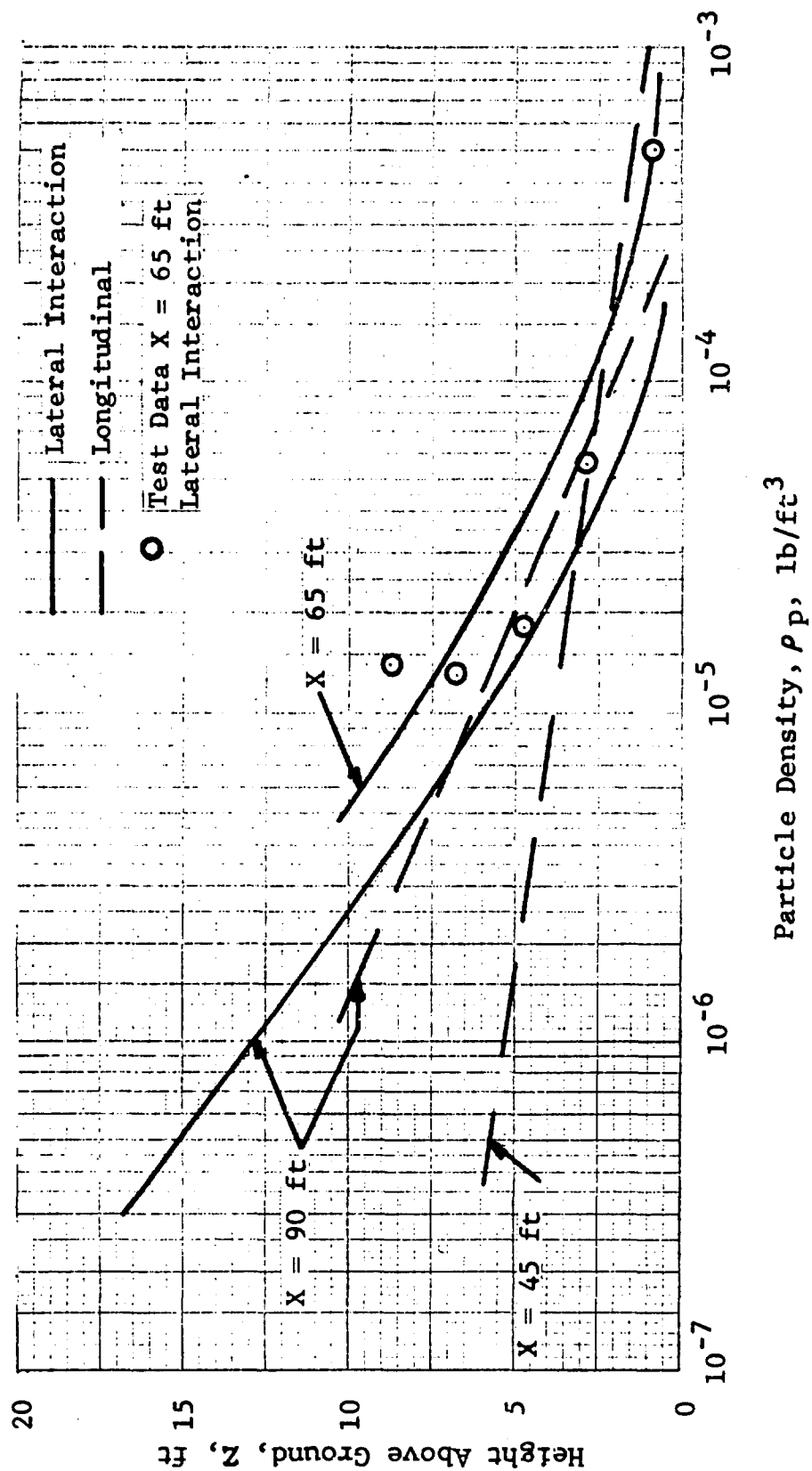
Figure 44. Particle Density Distribution for the H-21 Helicopter.

81
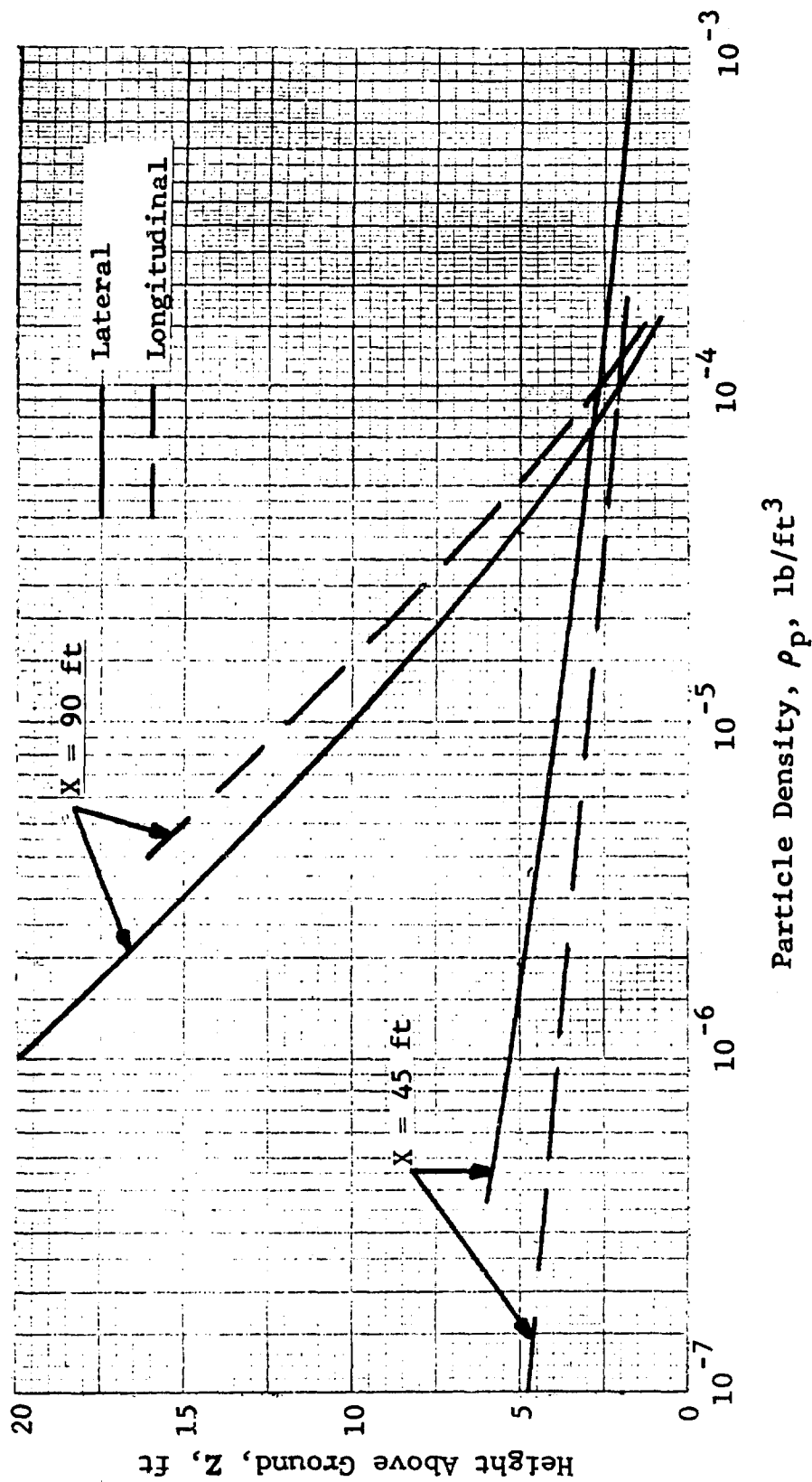
Figure 45. Particle Density Distribution for the XC-142 Aircraft.

82
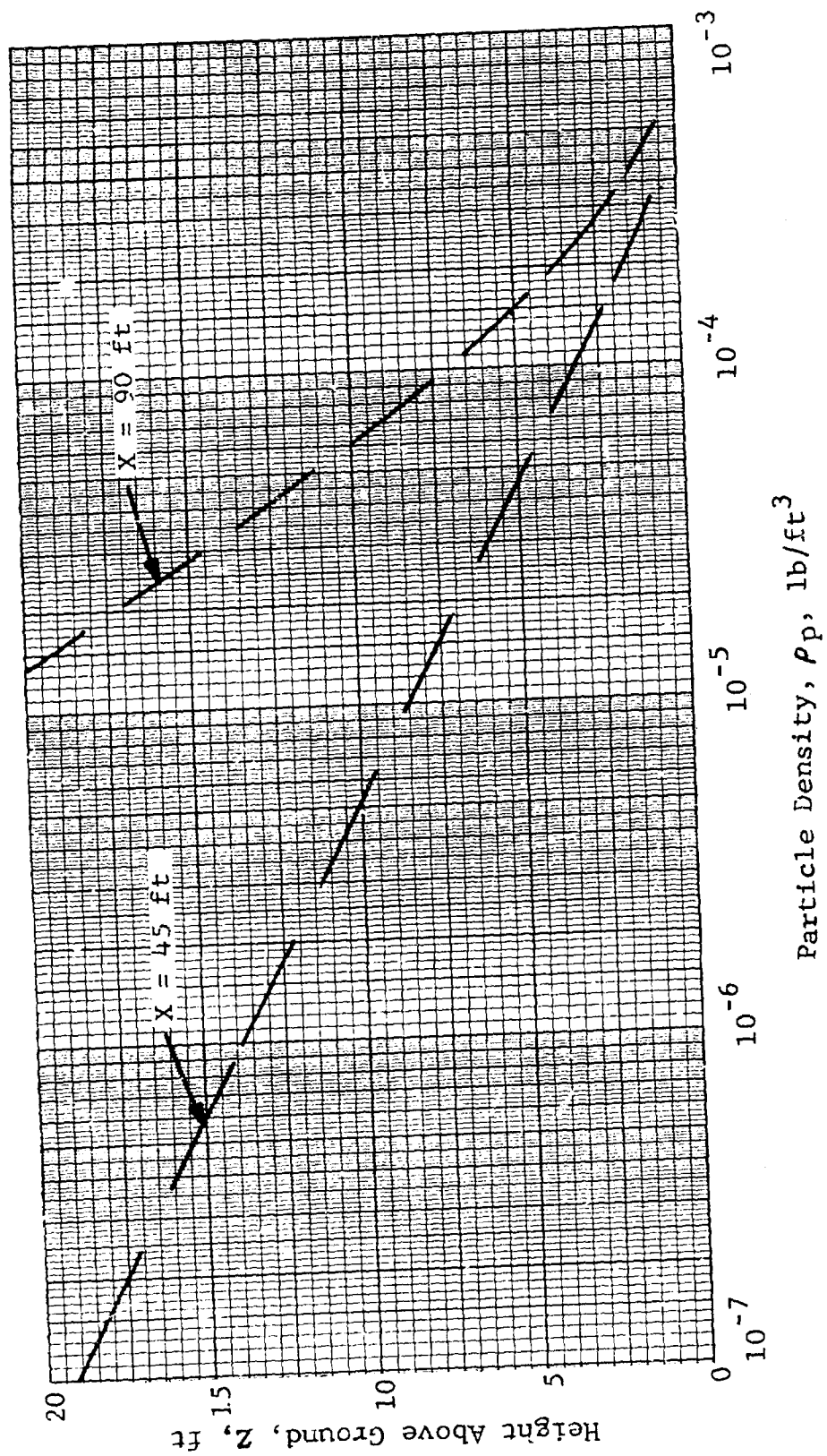
Figure 46. Particle Density Distribution for the X-22A Aircraft.
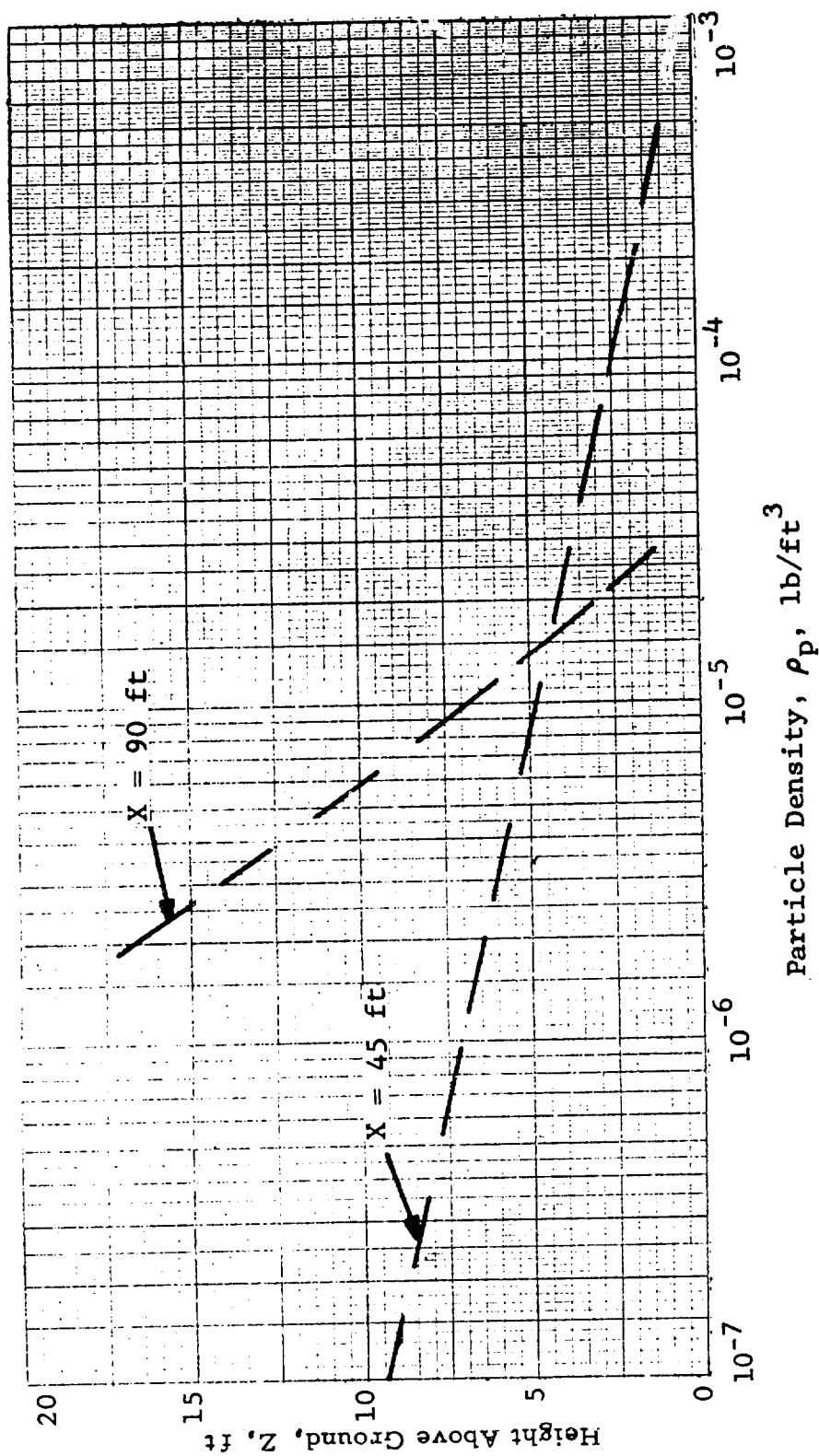
Figure 47. Particle Density Distribution for the X-19A Aircraft.
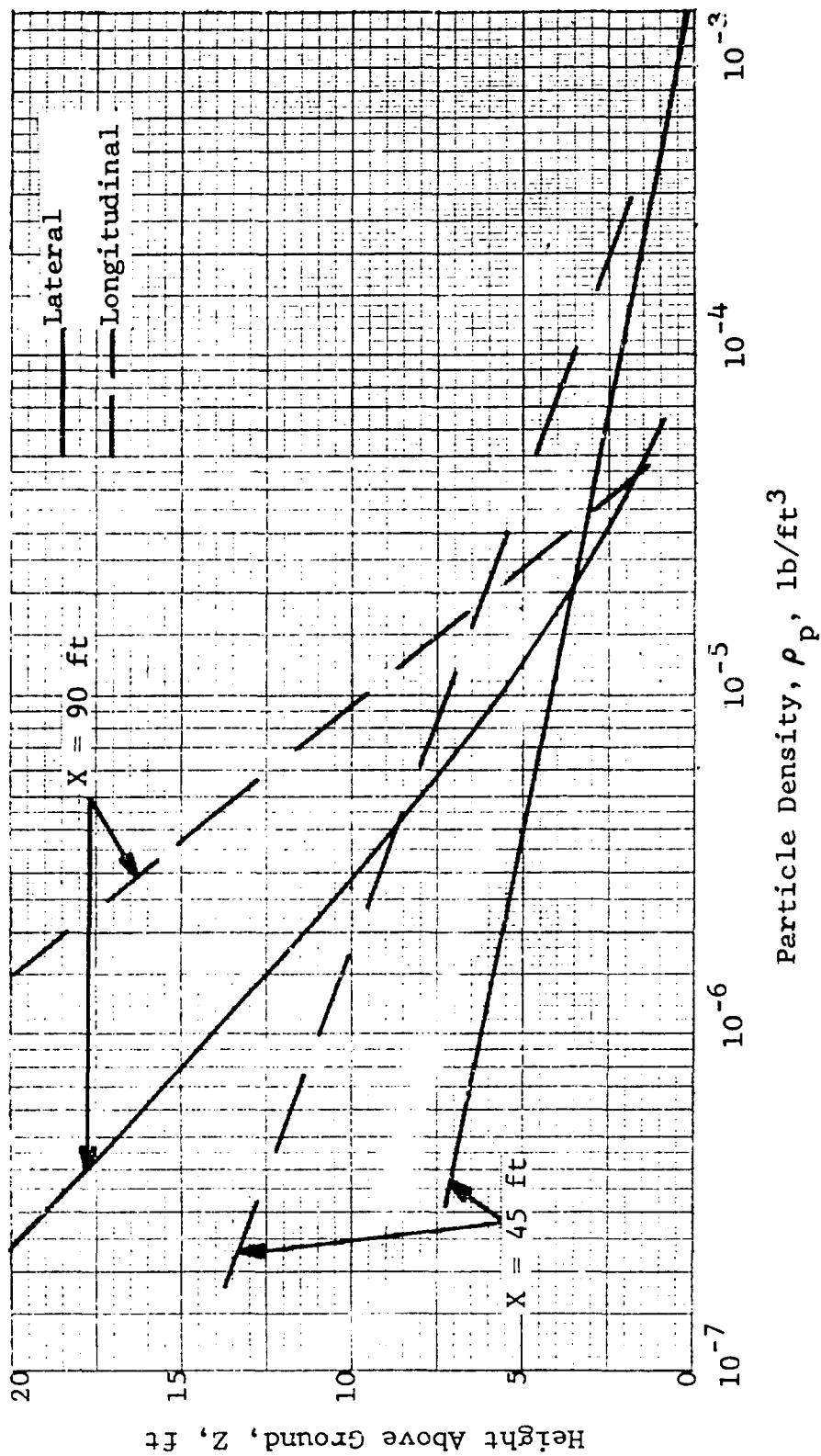
Figure 48. Particle Density Distribution for the XV-5A Aircraft.
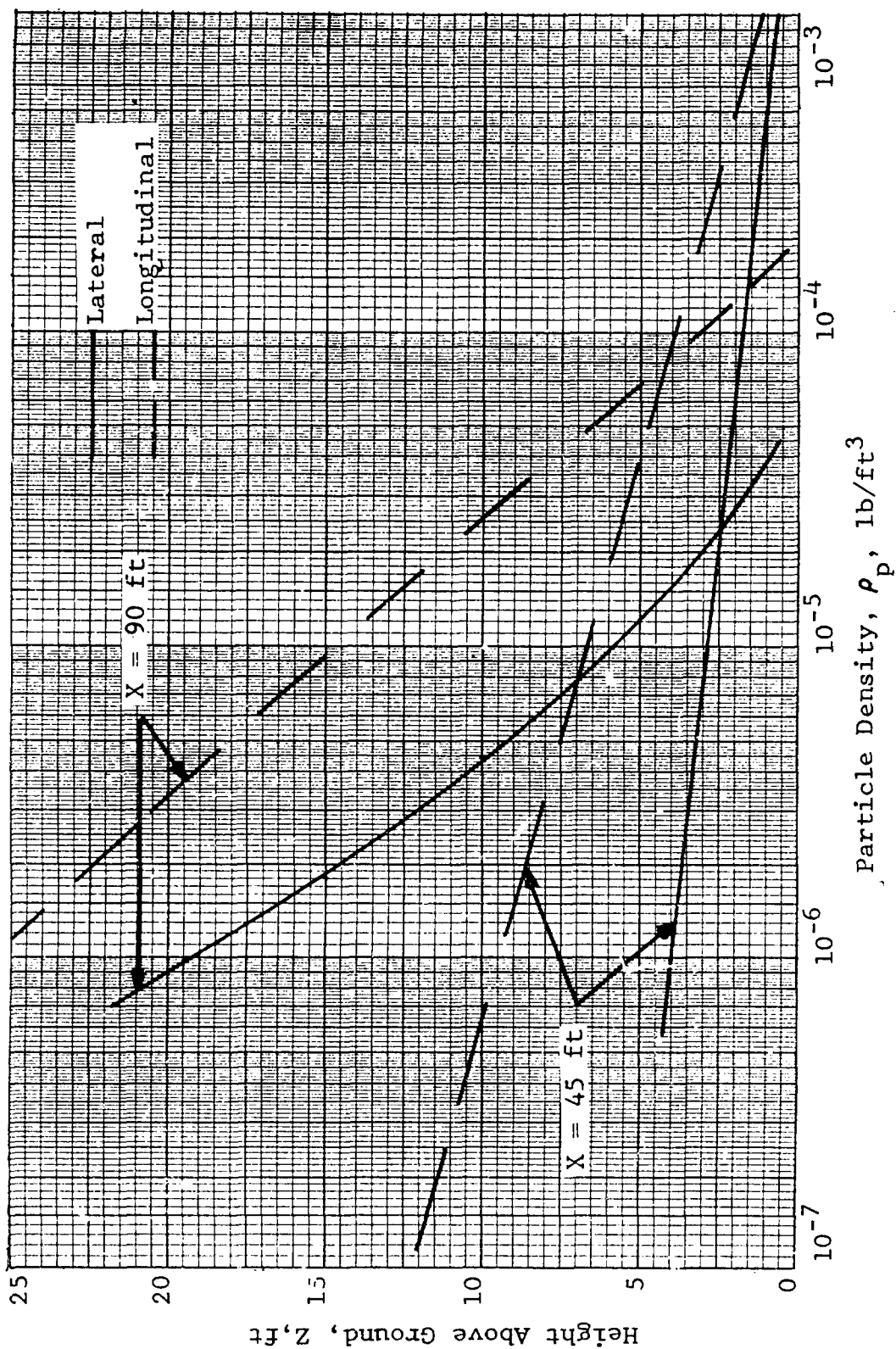
Figure 49. Particle Density Distribution for the XC-142 Aircraft, $H_W = 50$ Feet.

(zero wheel clearance) with Figure 49 (50 feet wheel clearance). It can be noted from these figures that particle density decreases as the aircraft lifts off the ground.

(2) Near-Field Density Distributions

As discussed previously, the near-field particle density distributions at or below the rotor disc (within the vortex cylinder) were computed utilizing the flow continuity concept within a given flow stream tube. The results thus obtained for the selected V/STOL aircraft are presented in Table IV, which also contains the pertinent test data.

It can be noted from this table that the predicted particle densities are generally higher along the interaction planes of multi-rotor configurations than along other locations in the close vicinity of rotor planes. Furthermore, the magnitudes of the predicted particle densities generally fall between the maximum and minimum values obtained from the tests for various V/STOL aircraft.

b. Particle Size Distributions

The particle size distributions for the selected V/STOL aircraft were computed based on the specified ground sample size profile.

This ground sample, together with the airborne particle size profile at the rotor planes for the selected V/STOL aircraft, is presented in Figure 50.

It can be noted from this figure that the airborne particle size (at the rotor plane) for the XC-142, X-22A, and XV-5A aircraft is not much different from the ground sample profile. This implies that practically all size particles present in the ground sample will be airborne as a result of the downwash velocities generated by these aircraft.

87

TABLE IV

PREDICTED AND MEASURED AVERAGE PARTICLE DENSITIES IN THE CLOSE VICINITY OF ROTOR PLANES FOR THE SELECTED AIRCRAFT

a. Predicted Particle Densities at the Rotor Plane

Aircraft	Densities (mg/ft^3)	
	Lateral Plane	Longitudinal Plane
H-21	19.75	4.15
XC-142	5.5	35.4
X-22A	-	62.96
X-19A	-	17.2
XV-5A	-	44.9
XC-142 (50 ft wheel clearance)	1.96	4.4

b. Measured Particle Densities in the Close Vicinity of the Rotor Plane

Source of Test Data	Densities (mg/ft^3)	
	Maximum	Minimum
Full-scale dual tandem test rig, two Lycoming T-53 engines (Reference 21)	31	--
KAC mock-up of X-22 at engine intakes (Reference 22)	85	--
Kaman HTK helicopter (Reference 20)	8.0	2.7
Kaman HTK helicopter hovering near an HOK helicopter (Reference 20)	24.5	5.4
Vertol Model 107 helicopter (Reference 23)	7.5	1.0
H-21 at Yuma (Reference 15)	31 64	2.8
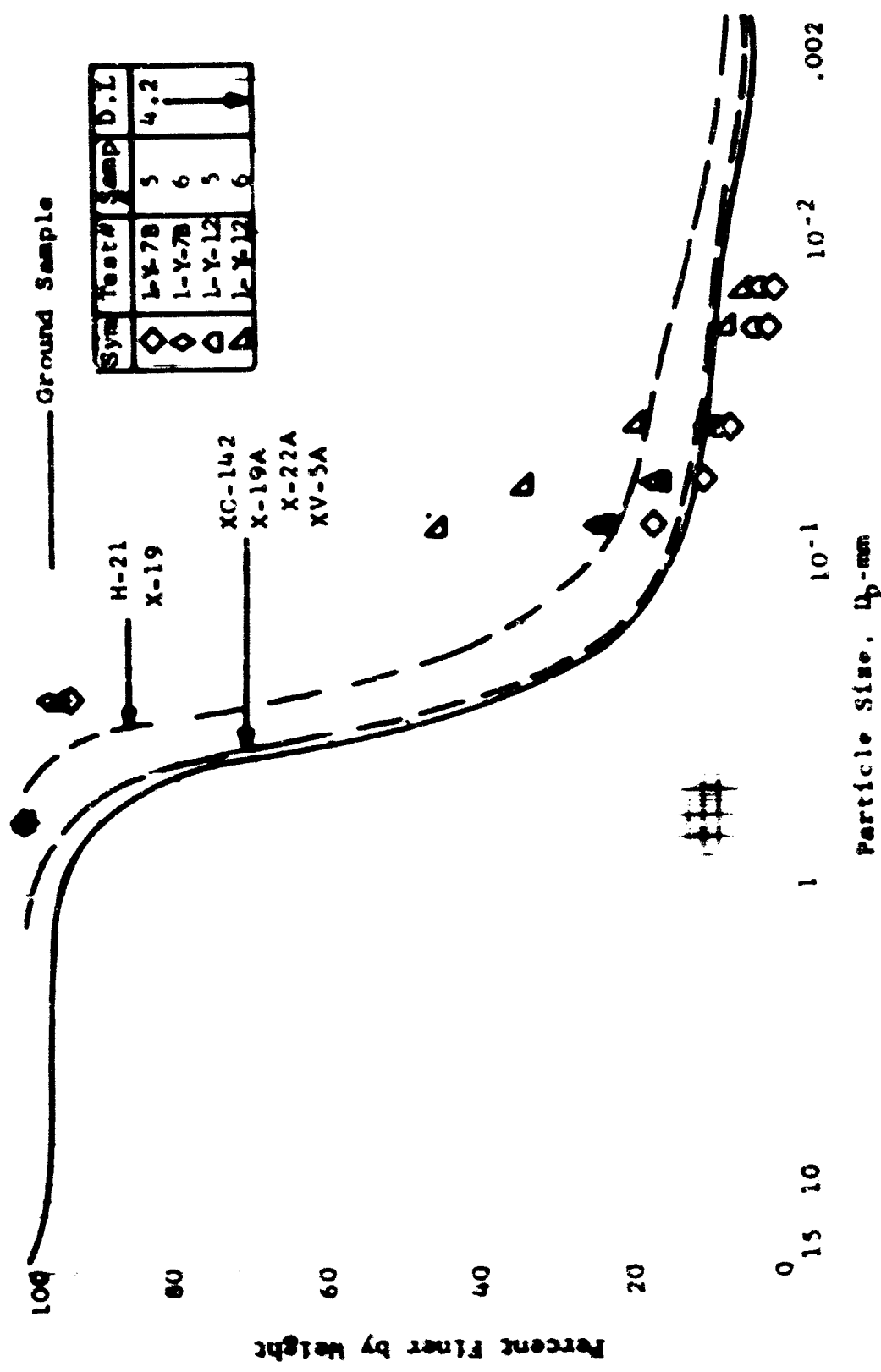
Figure 50. Particle Size Profiles (Ground Sample and the Airborne Sample at the Rotor Plane) for Various Aircraft.

The corresponding airborne particle sizes for the
H-21 and X-19A aircraft are appreciably smaller
than the ground sample sizes.

Figure 50 also contains the test data obtained from
Reference 15 for the H-21 helicopter. In general,
good correlations are indicated between the
predicted and measured particle sizes. More
detailed information on these tests is presented in
the appendix.

The maximum and mean (50 percent finer by weight)
particle size distributions for the H-21, XC-142,
and XV-5A are presented in Figures 51, 52, and 53,
respectively.

These figures show the variation of particle size
(diameter in mm) with height above the ground for
constant radial locations of X = 45 feet and
X = 90 feet.

It can be noted from these figures that for a
constant radial location, the maximum size of
particles reduces with increasing height. Also, for
a constant height above the ground (e.g., 7 feet),
larger maximum size particles can be found further
away from the aircraft (X = 90 feet). This latter
trend is a function of aircraft disc loading, height
above the ground, and aircraft geometry; it may
reverse depending on the combinations of these
parameters (e.g., see Figure 51 for heights of less
than 5 feet above the ground).

c. **Effect of Terrain**

The rotor downwash signatures thus far discussed are
strongly dependent on the type of terrain and the
dynamic pressure generated by the lifting aircraft.

As reported in Reference 9, the point of incipient
erosion for any terrain can be related to the
aircraft's disc loading; thus, the criteria under
which the rotor downwash will create a dust cloud
for a given terrain can be established. The data
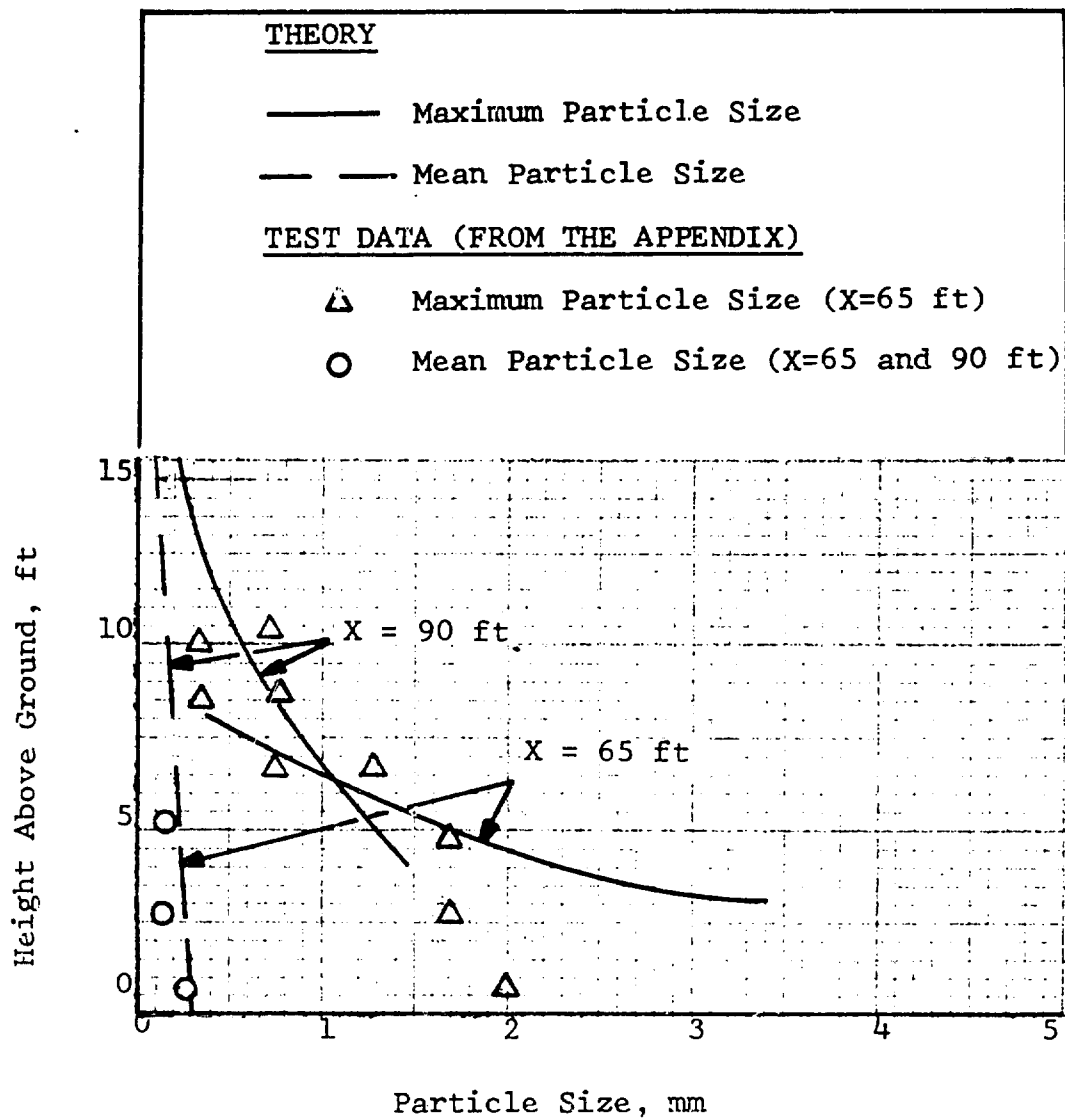
Figure 51. Particle Size Distributions for the H-21 Aircraft.
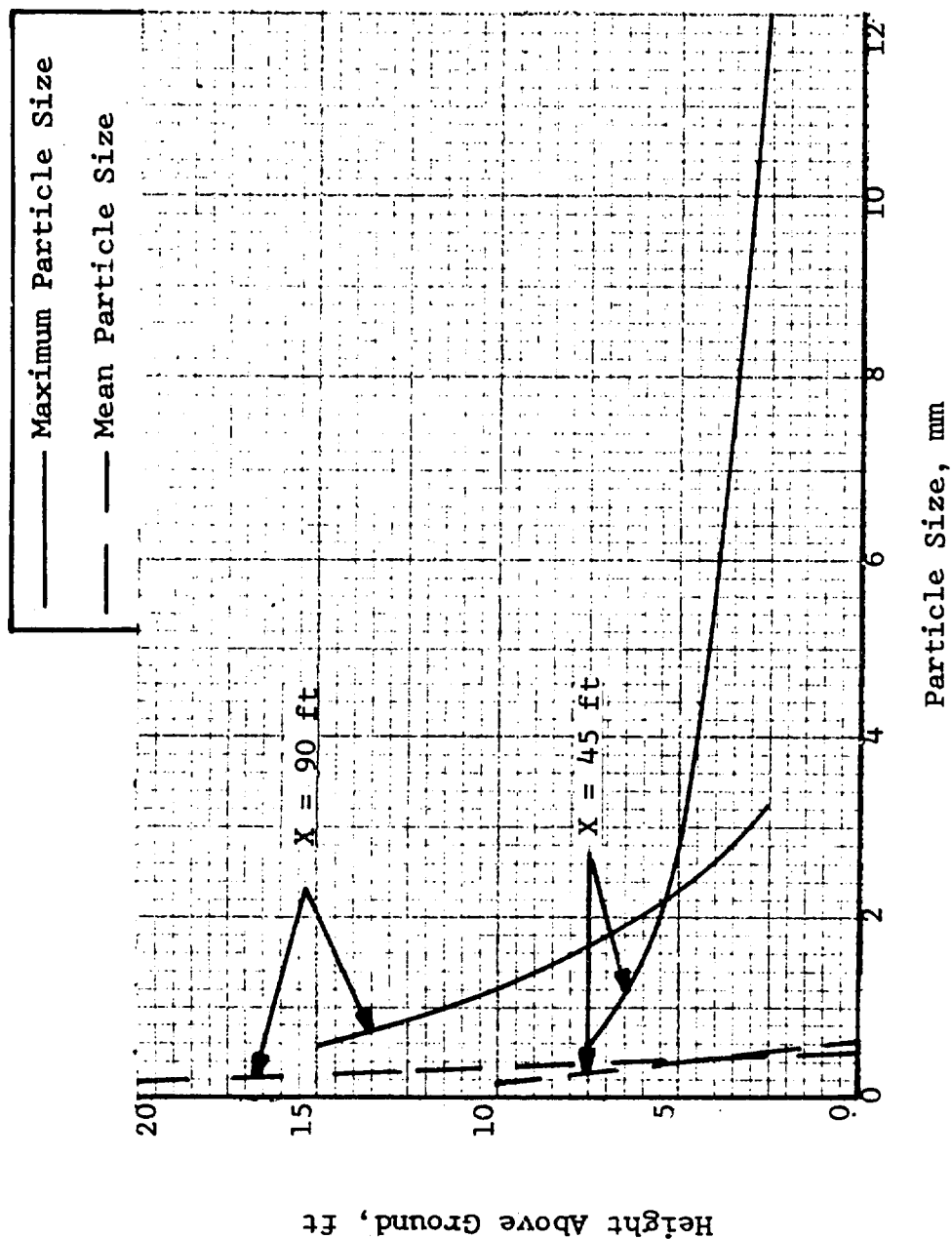
Figure 52. Particle Size Distributions for the XC-142 Aircraft.
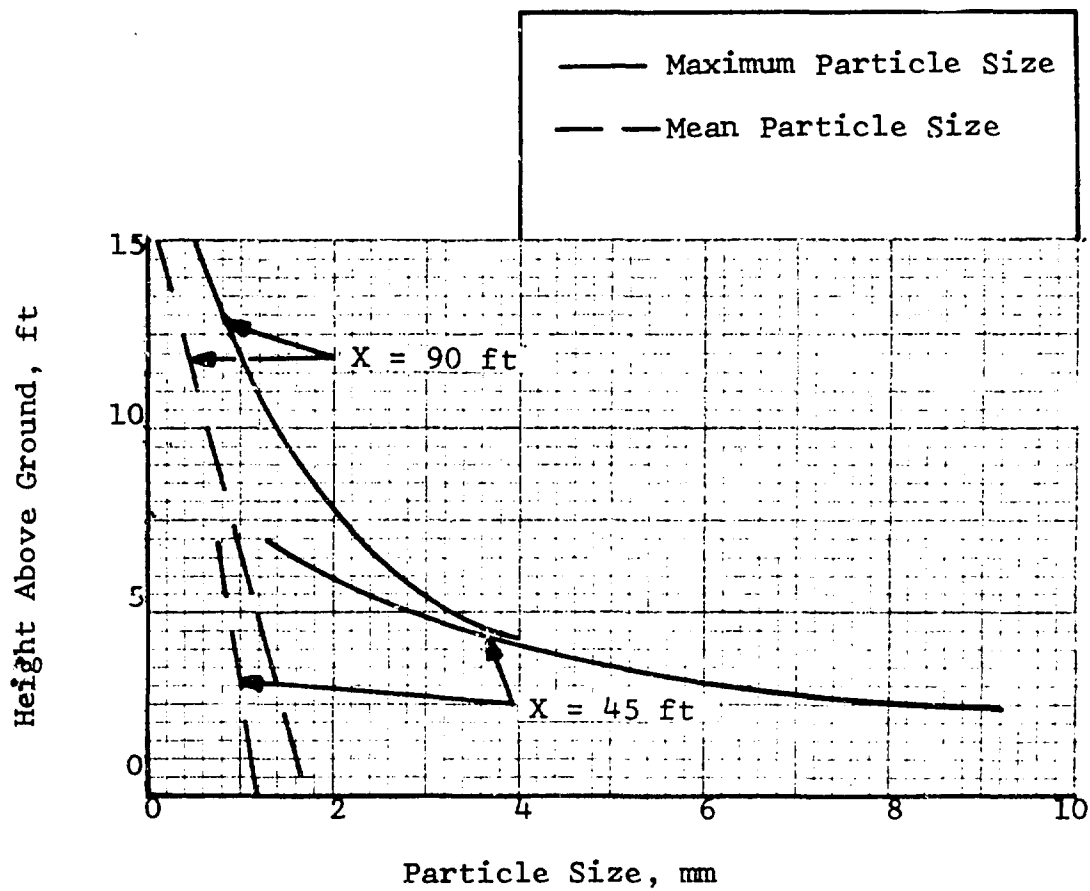
Figure 53.   Particle Size Distributions
             for the XV-5A Aircraft.

93

for the incipient erosion of various terrains as
presented in Reference 9 are summarized in Figure 54.
As can be noted from this figure, terrains such as
silty sand or water can be eroded by all aircraft
considered in this study; crushed stone, plowed
earth, or soaked sand will be eroded only by the
XC-142 or X-22A; and packed lean clay will be eroded
only by the XV-5A.

C. DOWNWASH SIGNATURE EFFECTS

Presented in this section are the results of the effects of
rotor downwash environment on pilot's visibility, engine,
ground equipment and personnel.

1. Pilot's Visibility

The computations of pilot's visibility as affected by the
dust cloud were performed assuming the object and background
light intensities in the uncontaminated atmosphere of
$I_s = 0.2$ foot-lambert and $I_o = 0.1$ foot-lambert, respectively.

In addition, the aircraft heading relative to the object was
taken as 45 degrees along the pilot's line of sight. Al-
though the prime concern in pilot's visibility through a
dust cloud is an unimpaired ground reference, the reduction
in pilot's visibility is herein computed in terms of light
transmittance (T) as a function of object height above the
ground.

The results which were obtained for the five selected V/STOL
aircraft are presented in Figures 55 through 60, which show a
reduction of light transmittance with reduction in object
height. This trend occurs due to an increase in particle
density and cloud penetration distance as object height from
the ground is reduced. For a constant object height, the
variation of light transmittance with horizontal distance
from the pilot to the object depends on the dust cloud
characteristics and aircraft geometry (e.g., compare Figure 55
with Figure 58).

For direct comparison of loss of pilot's visibility from
various V/STOL aircraft, the light transmittance results

94
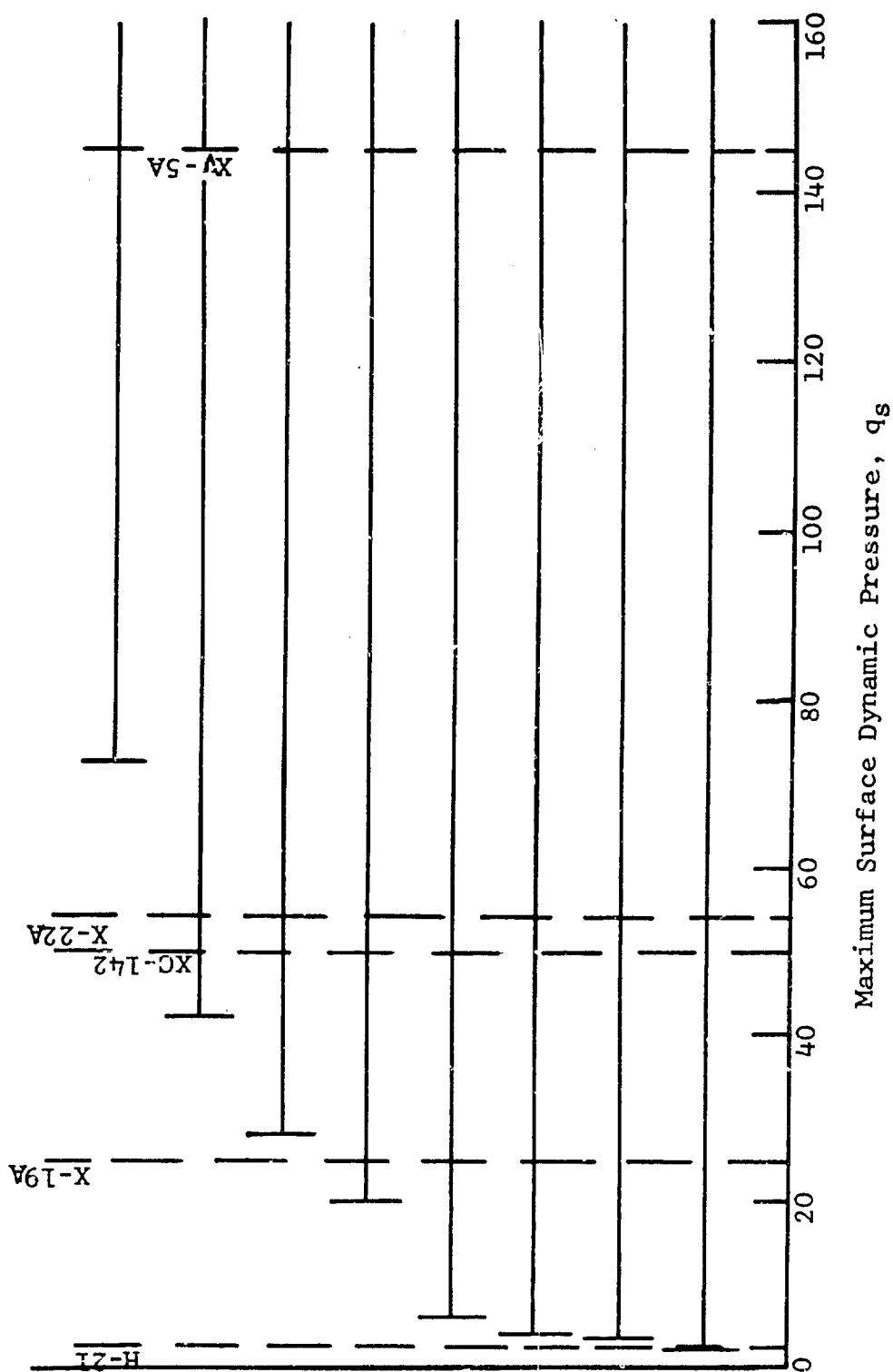
Figure 54. Variation of Incipient Erosion With Terrain.

Maximum Surface Dynamic Pressure, q_s
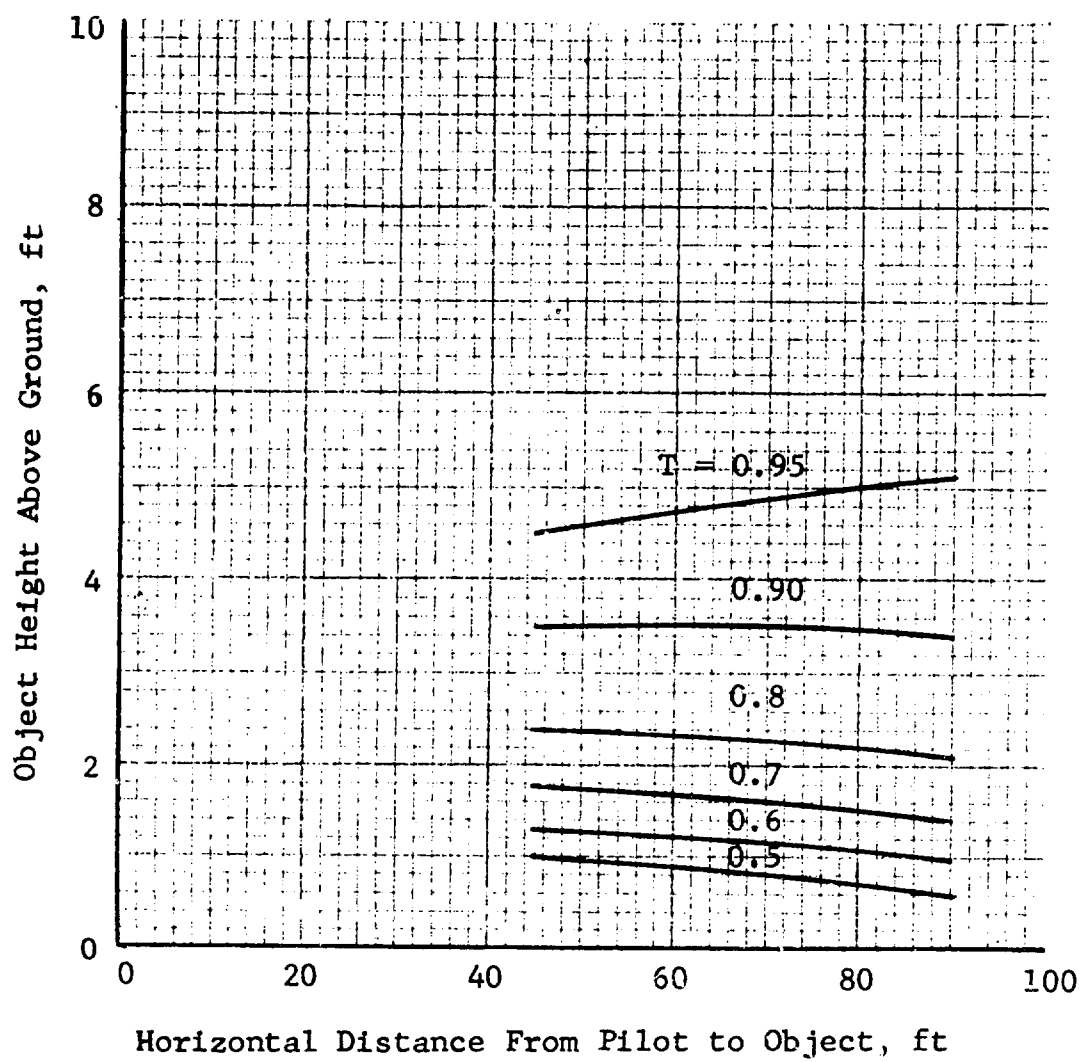
Figure 55. Light Transmittance for the H-21 Aircraft.
Wheels on Ground, $\psi = 45°$.

96
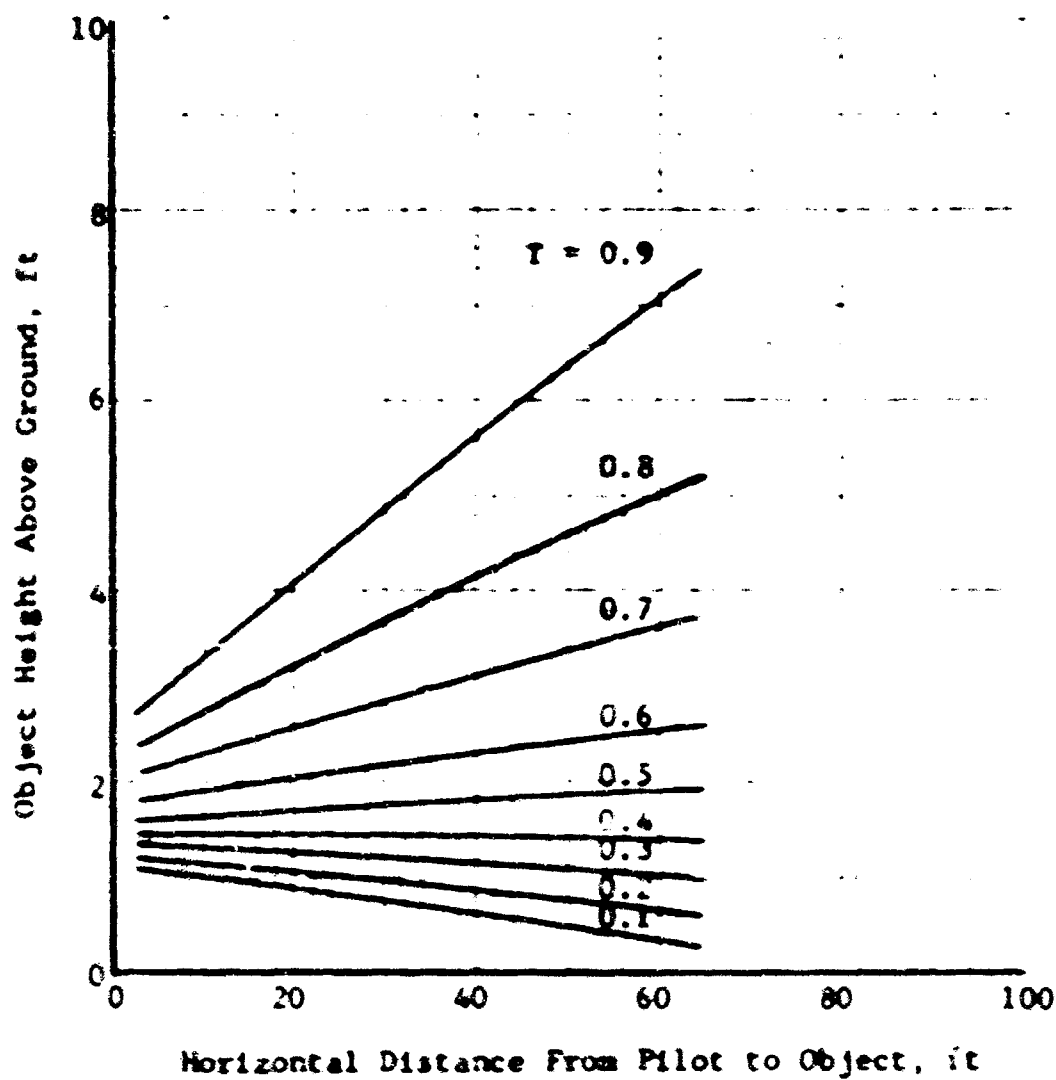
Figure 56. Light Transmittance for the XC-142 Aircraft. Wheels on Ground, φ = 45°.
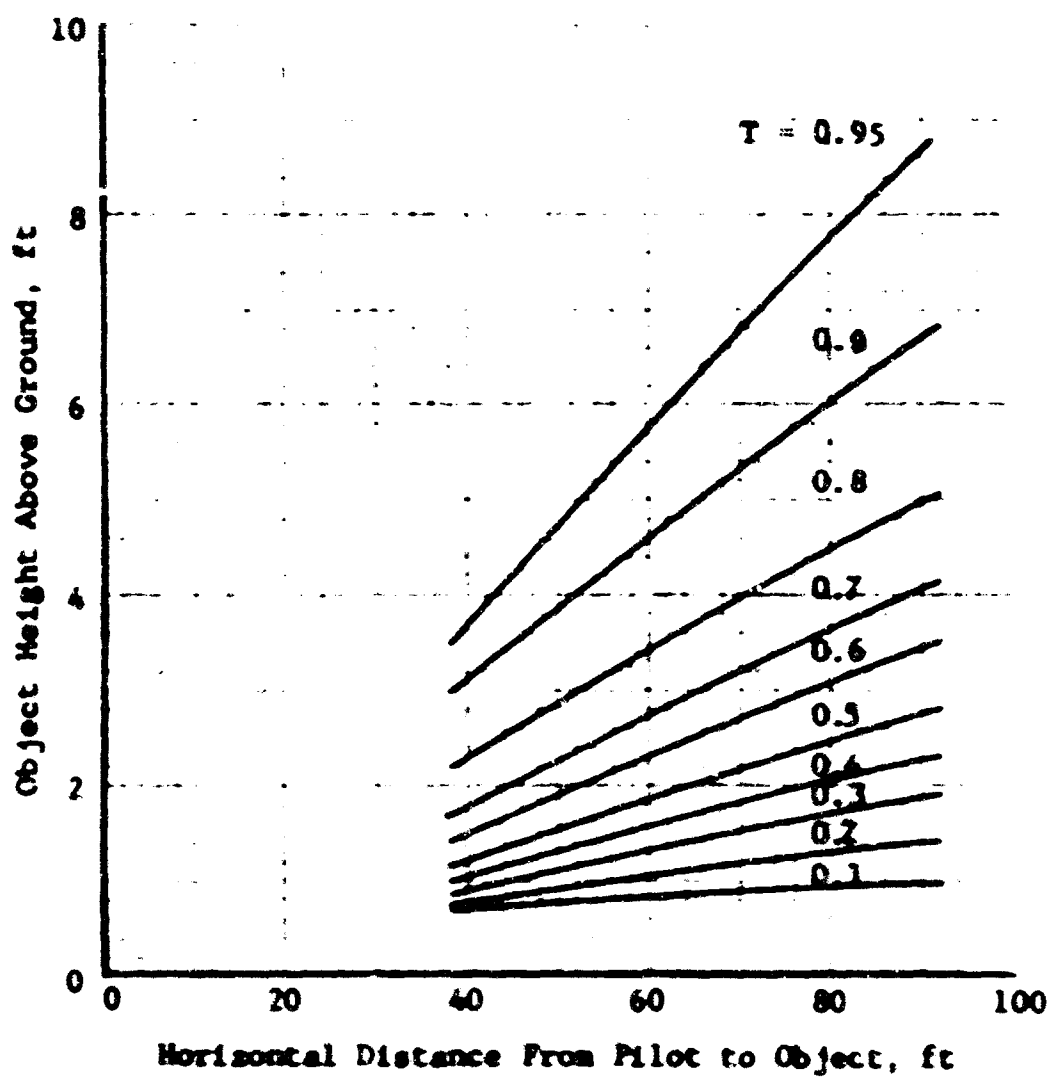
Figure 57. Light Transmittance for the X-22A Aircraft. Wheels on Ground, $\phi = 45°$.
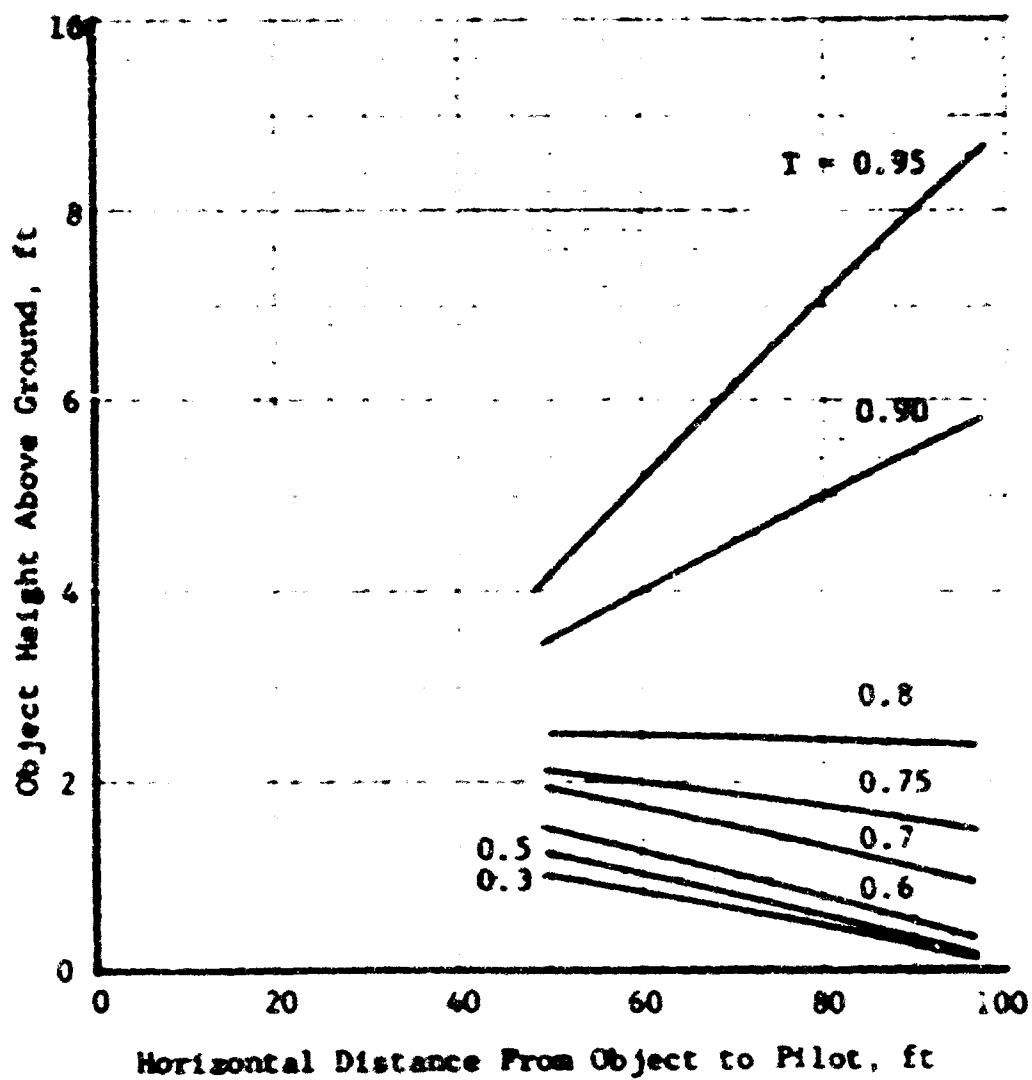
Figure 58. Light Transmittance for the X-19A Aircraft. Wheels on Ground. ψ = 45°.
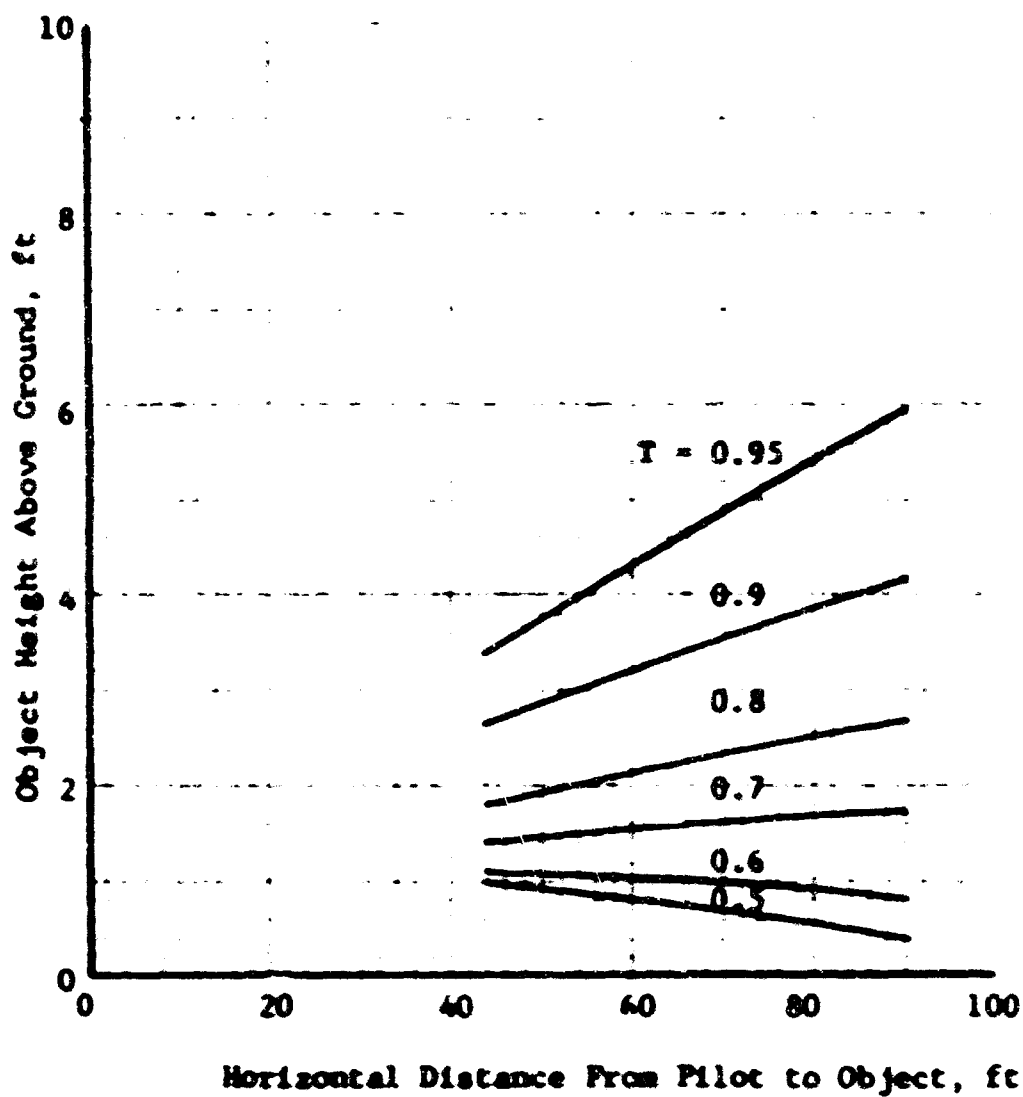
Figure 59. Light Transmittance for the XV-5A Aircraft. Wheels on Ground, $\psi = 45°$.
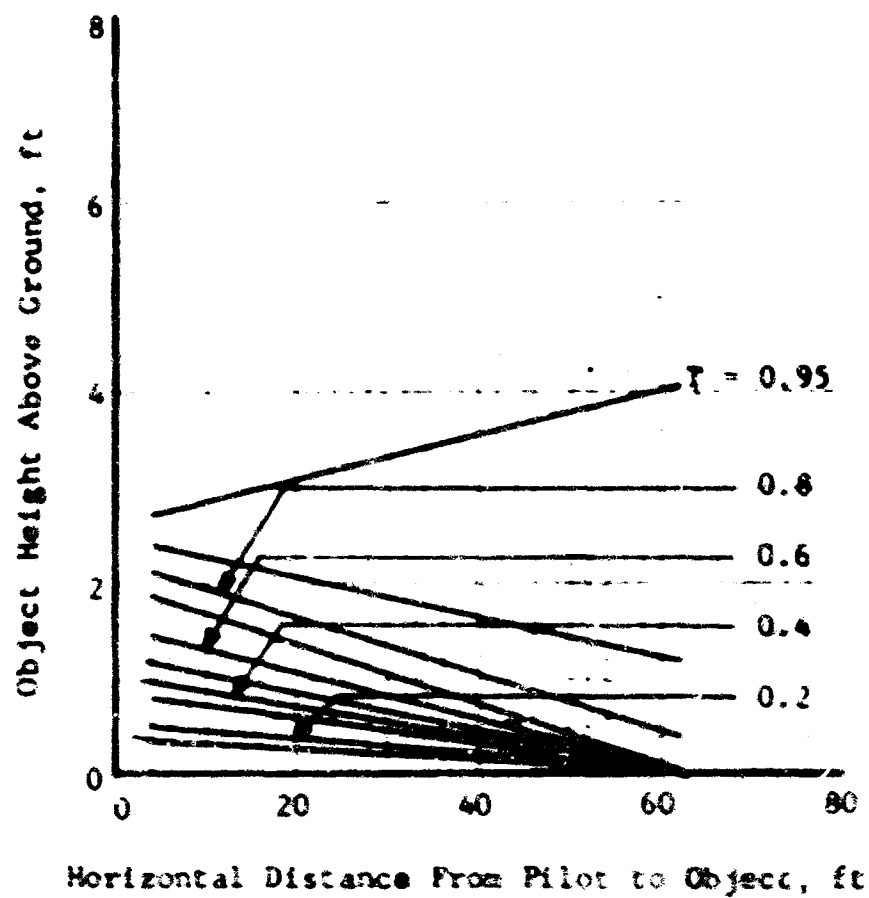
Figure 60. Light Transmittance for the X-142 Aircraft.
Wheels on Ground, Wheel Height = 50 Feet.

(Figures 55 through 60) were utilized to compute minimum perceivable object size for 1 foot object height above the ground. These results, together with the uncontaminated atmosphere data, are presented in Figure 61. In general, Figure 61 shows an order of magnitude reduction in pilot's visibility due to the dust cloud for all aircraft as compared to the visibility in uncontaminated atmosphere. Variations of visibility for specific aircraft are functions of aircraft disc loading, gross weight, and orientation of the pilot with respect to the sighted object. The latter variable affects both the depth of penetration in the cloud (d) and the distance to the object (S_h). Both of these parameters are important in determining the minimum perceivable object size. Effect of distance from the pilot to the object is demonstrated in Figure 61 by comparing the results of perceivable object size for the XC-142 aircraft for zero and 50 feet wheel clearance. Even though particle density close to the ground is significantly higher for zero wheel clearance than for 50 feet height, the visibility in terms of object size is better at lower height due to the reduced distance, S_h.

2. Engine Damage

Another significant effect of downwash signatures is that on engine damage. The discussion presented below outlines the types of damage to engine components and the resulting effects on engine performance. Also, the effects of sand and dust filtration on extending engine life and improving engine performance are discussed.

a. Damage of Engine Components

Based on the test data presented in References 22 through 27, the following types of turbine engine damage have been incurred by operation of various types of engines in a sand and dust environment:

(1) Compressor blade leading edge bending and peening.

(2) Compressor blade trailing edge rounding.
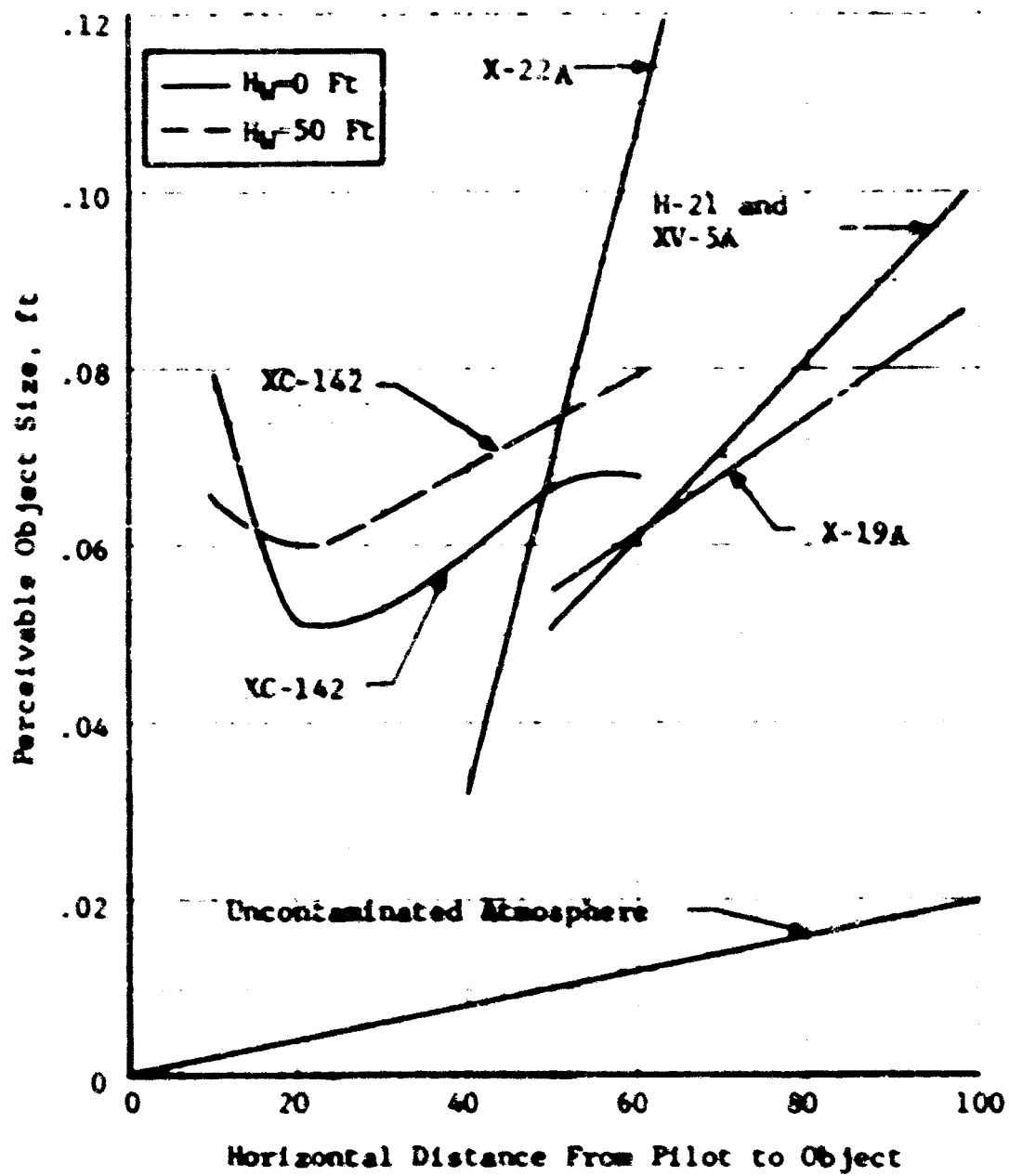
Figure 61. Perceivable Size of an Object Sighted Through Dust Clouds Generated by Various Aircraft.

(3) Erosion of compressor blade tips and stator vanes roots.

(4) Scale-like dirt accumulation.

The leading edge bending and peening of the first and possible second stage compressor blades is caused by ingestion of large size particles (greater than 200 microns). These particles, which are subsequently reduced in size through a direct impact on the first stage compressor blades and the small size particles (less than 200 microns) directly ingested, cause trailing edge rounding of compressor blades in the second and succeeding stages.

The ingested sand and dust which is centrifuged outward as it proceeds axially causes erosion of compressor blade tips and stator vane roots. As a result of this damage, the mass distribution of both compressor blades and stator vanes changes such that the natural frequency of the compressor blades is increased while that of the stator vanes is reduced.

Scale-like dirt has been found accumulated on diffuser combustion chamber and other engine components after prolonged engine operations in contaminated atmosphere.

b. **Deterioration in Engine Performance**

As shown in References 22 through 27, sand and dust ingestion adversely affects engine performance. Continued operation in the contaminated atmosphere will produce damage which in turn reduces engine available power and increases engine fuel consumption.

Analysis of the test data presented in References 22 through 27 indicates that engine power loss can be related to the accumulated weight of ingested sand and dust. Figure 62 presents trends of ingested sand and dust weight as a function of engine airflow corresponding to a 5-percent reduction in engine normal rated power.

104
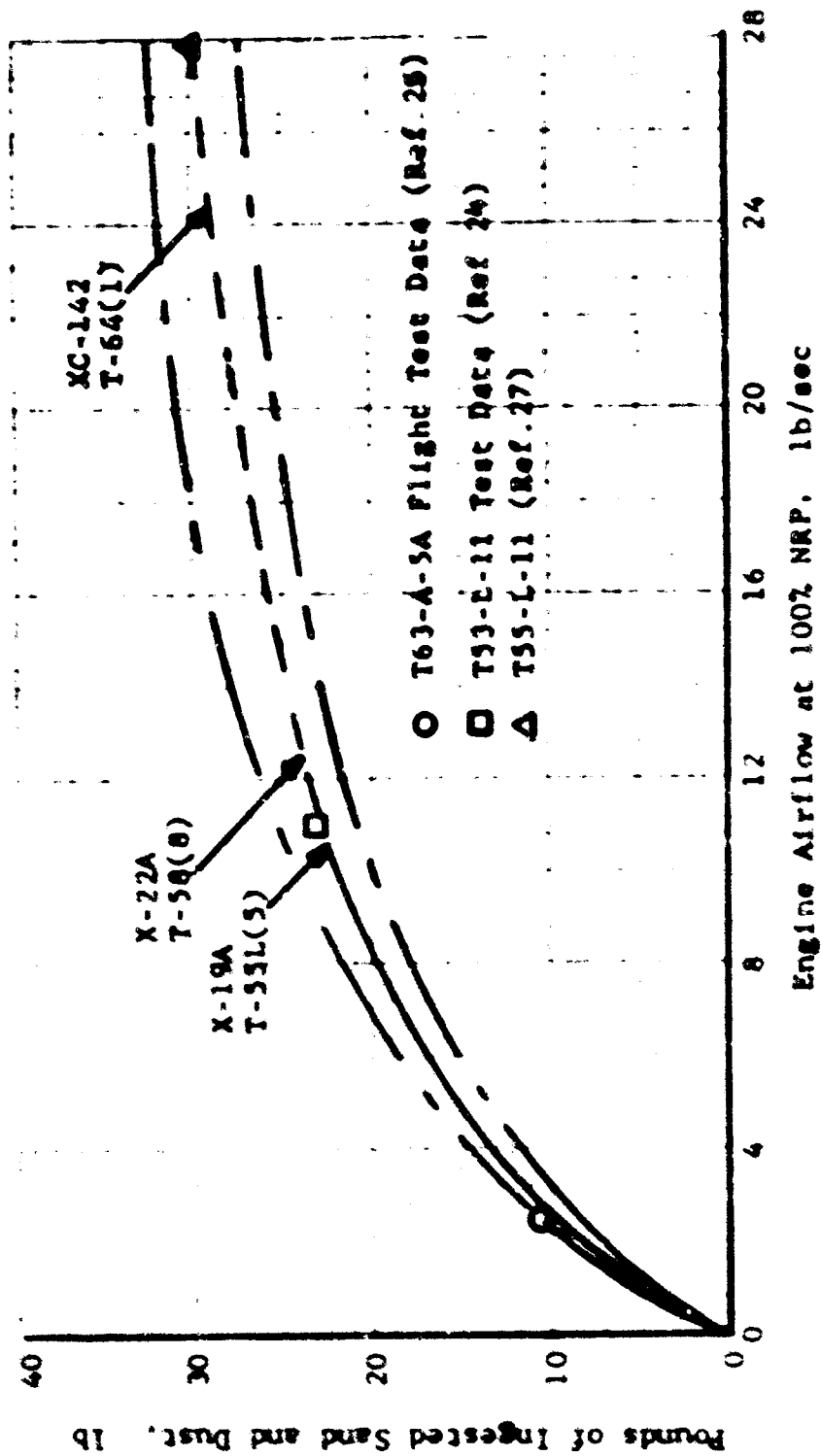
Figure 62. Variation of Engine Ingested Sand and Dust With Engine Airflow for a 5-Percent Reduction in Normal Rated Power.

The results presented in this figure are based on
limited test data obtained for the T-53-2 engine
(Reference 25) and the T-55-L-11 engine (Reference
27). These results can be extrapolated to other
V/STOL aircraft engines. A bandwidth of approxi-
mately ±10% (from the available test data) is shown
in this figure to account for variations in
susceptibility of a particular engine design to
damage and relative hardness of the contaminant
material.

Figure 62 also shows the amount of sand and dust
which can be ingested by the T-64(1), T-58(8), and
T-55L(5) engines, prior to 5-percent loss in normal
rated power. Based on these results, the engine
endurance corresponding to the XC-142, X-22A, and
X-19A aircraft has been calculated and is presented
in Table V.

c. Improvements Offered by Dust Filtration

Considerable improvements in engine life and perform-
ance is possible with sand and dust filtration. The
degree of this improvement, as indicated in Figure 63,
is very much dependent on filtration efficiency of
air particle separators installed on the engines.
Figure 63 shows that even with the current air
particle separator designs (75 to 90-percent filtra-
tion efficiency), net operational gain in engine
endurance of 4 to 10 is achievable. The net opera-
tional gain is herein defined as the ratio of engine
endurance with particle filtration (protected engine)
to that with no particle filtration (unprotected
engine) corresponding to 5-percent reduction in engine
normal rated power.

The filtration efficiency warranted for a given design
is a function of engine susceptibility to the particle
damage and engine maintenance schedule desired. As
shown in Figure 63, the net operational gain increases
very rapidly with filtration efficiency beyond 80
percent and becomes large at 100-percent filtration
efficiency.

	TABLE V			
RESULTS OF DUST INGESTION BY VARIOUS V/STOL ENGINES FOR A 5-PERCENT REDUCTION IN NORMAL RATED POWER				
Aircraft	Sand Ingested (lb)	Airflow (lb/sec)	ρ_P (lb/ft^3)	Engine Endurance (minutes)
XC-142	29	24.5	7.7×10^{-5}	20
X-22A	24	12.4	34.2×10^{-5}	7.2
X-19	22.5	10.7	2.7×10^{-5}	99

3. Personnel and Ground Equipment Damage

This section presents the effects of rotor downwash signature on personnel and ground equipment in terms of primary and secondary wind damage. Primary damage relates to direct injury to man and destruction of equipment. Secondary damage pertains to the indirect effect of downwash upon man and equipment such as impaired work capabilities of a man or displacement of objects placed in the rotor downwash environment.

Based on the test data of Reference 10, rotor downwash impingement can directly cause injury to man. The extent of injury can vary from damage to loose areolar tissues about the eyes at wind speeds of 100 knots, to severe confluent subconjunctional hemorrhages at speeds of 515 knots. Figure 64 graphically presents levels of direct and indirect damage to man and equipment due to impingement of downwash velocities generated by the selected aircraft.

Comparing the results of Figure 64, it can be noted that the downwash velocity from the X-19A, X-22A, XV-5A, and XC-142 aircraft at respective distances of up to 13, 20, 26, and 36 feet can cause a serious injury to man's eye areolar tissues.
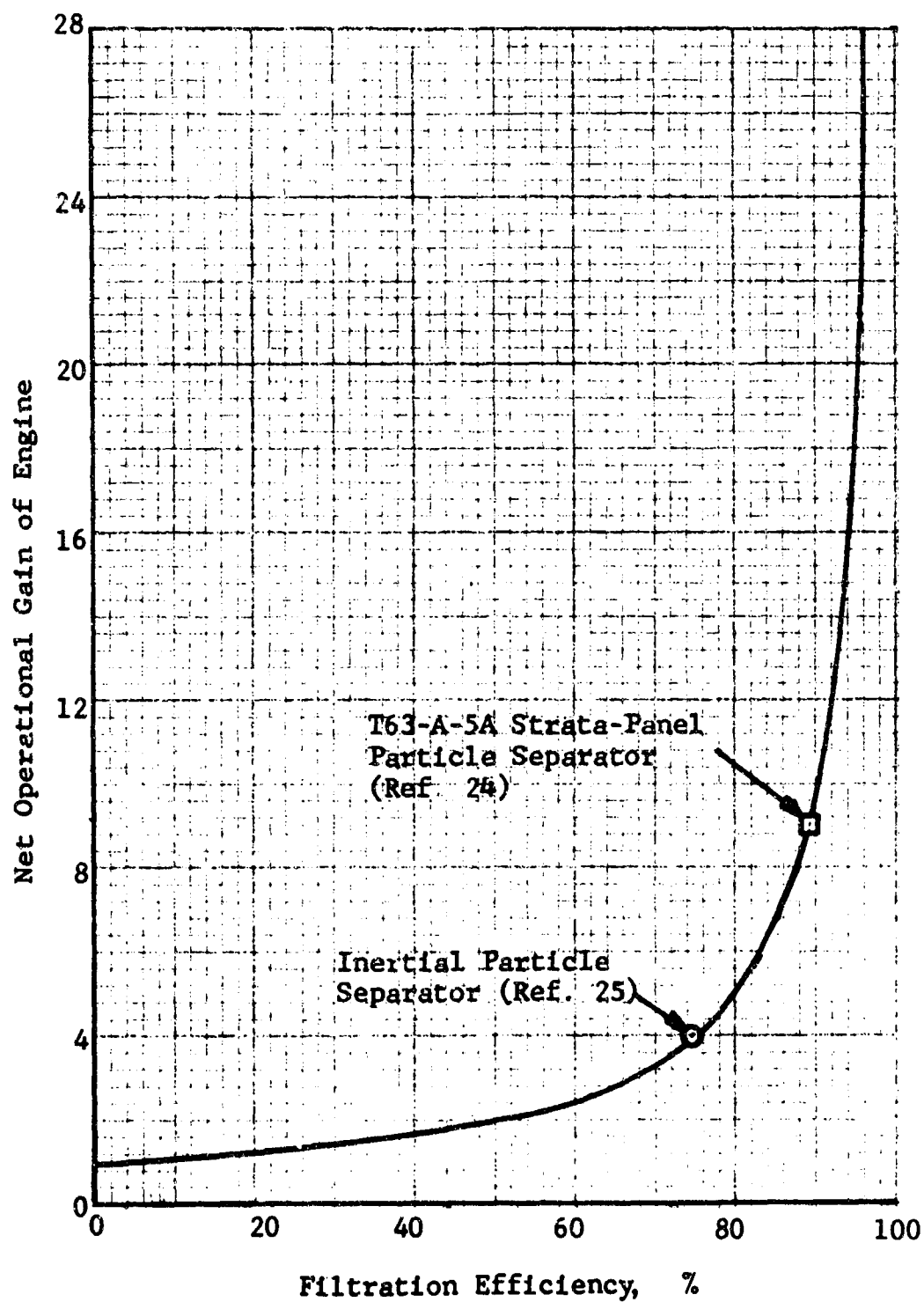
Figure 63. Engine Net Operational Gain for a 5-Percent
Reduction in Normal Rated Power.

108
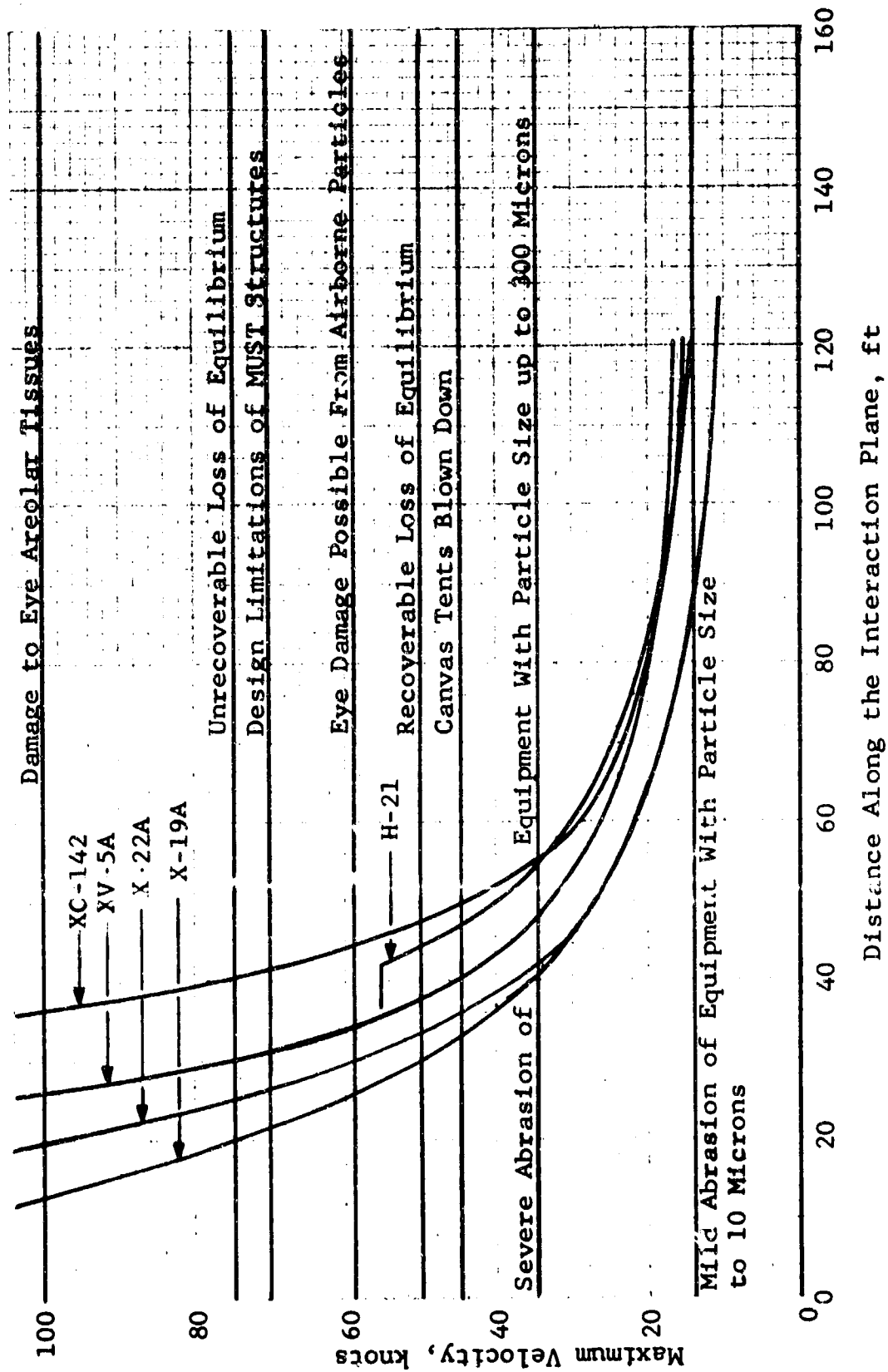
Figure 64.   Effects of Rotor Downwash Upon Man and Equipment for Various Aircraft. Wheels on the Ground.

Also, the design limitations of MUST structures can be exceeded in the downwash environment generated by the four aircraft at distances of up to 21.5, 26, 31, and 41.5 feet, respectively. These design limitations of MUST structures would not be exceeded by the downwash velocities of the H-21 helicopter. Canvas tents can be blown down by the downwash velocities of each of the five selected V/STOL aircraft. These velocities can cause a severe penetration and abrasion of equipment with particle sizes of up to 300 microns. This type of equipment damage can be incurred at distances up to 40 to 60 feet from each aircraft.

In general, it can be stated that the high-disc-loading aircraft such as the XC-142, X-22A, X-19A, and XV-5A are potentially capable of generating a more hazardous downwash environment to man and equipment than the low-disc-loading V/STOL aircraft such as the H-21.

IV. CONCLUSIONS AND RECOMMENDATIONS

1. The analytical methods presented herein for predicting rotor downwash signatures generally correlate well with the limited test data.

2. High downwash velocities generated by high-disc-loading aircraft decay much more rapidly than the low velocities generated by low-disc-loading aircraft. As a result, the latter velocities generated in ground effect persist at greater radial distances along the ground.

3. For the type of terrain analyzed, the size of a dust cloud generated by a V/STOL aircraft is primarily dependent on aircraft gross weight rather than rotor disc loading. The maximum cloud sizes reduce slightly with increasing disc loading (constant gross weight) but reduce appreciably with reduction in aircraft gross weight.

4. The pilot's far-field visibility through a dust cloud depends upon the density and size of the cloud and the location of the sighted object relative to the pilot.

5. Sand and dust ingestion in V/STOL engines causes severe damage to engine components, thus reducing engine life and resulting in appreciable reduction in engine performance. Particle separators with filtration efficiencies in excess of 80 percent are required for any VTOL aircraft for sustained operations in sand and dust environment.

6. High-disc-loading aircraft are potentially capable of generating a more hazardous downwash environment to man and equipment than low-disc-loading aircraft.

7. It is recommended that further tests be conducted to define better and to confirm more firmly the analytical methods for predicting the rotor downwash signatures.

111

V. REFERENCES

1. Heyson, H. H., "An Evaluation of Linearized Vortex Theory as Applied to Single and Multiple Rotors Hovering in and out of Ground Effect", NASA TND-43, September 1959.

2. Fradenburgh, E. A., "Flow Field Measurements for a Hovering Rotor Near the Ground", Fifth Annual Western Forum, American Helicopter Society, Inc., September 1958.

3. Goland, L., "The Normal Induced Velocity in the Vicinity of a Thrust Rotor", University of Pennsylvania Dissertation, 1962, Dynasciences Corporation Report No. DCR-12, December 1962.

4. Heyson, H. H., and Katzoff, S., "Induced Velocities Near a Lifting Rotor With a Nonuniform Disk Loading", NACA Report 1319, 1957.

5. Gessow, A., and Myers, G. C., Jr., "Aerodynamics of the Helicopter", The MacMillan Company, 1952.

6. Heyson, H. H., "Induced Velocity Near a Rotor and Its Application to Helicopter Problems", Proceedings of the Fourteenth Annual Forum, American Helicopter Society, Inc., April 1958.

7. Ludwig, G. R., and Brady, W. G., "Theoretical and Experimental Studies of Impinging Uniform and Nonuniform Jets", TRECOM Technical Report 64-42, U.S. Army Aviation Materiel Laboratories, Fort Eustis, Virginia, August 1964.

8. Glauert, M. B., "The Wall Jet", Journal of Fluid Mechanics, Vol. 1, Pt. 6, December 1956.

9. George, M. M., and Perlmutter, A. A., and Butler, L., "Downwash Impingement Design Criteria for VTOL Aircraft", TRECOM Technical Report 64-48, U.S. Army Aviation Materiel Laboratories, Fort Eustis, Virginia, August 1964.

10. Schane, W. P., LTC, MC, "Effects of Downwash Upon Man", USAARU Report No. 68-3, U. S. Army Aeromedical Research Unit, Fort Rucker, Alabama, November 1967.

11. Bolonovich, M., and Marks, M. D., "Experimental Downwash Velocity, Static Pressure, and Temperature Distributions in Ground Effect for a 75-Foot Jet Driven Rotor", AHS Journal, Vol. 4, No. 2, April 1959.

12. Newsom, W. A., and Tosti, L. P., "Slipstream Flow Around Several Tilt-Wing VTOL Aircraft Models Operating Near Ground", NASA TND-1382.

13. Morse, A., and Newhouse, H., "VTOL Downwash Impingement Study - Surface Erosion Tests", TREC Technical Report 60-67, U. S. Army Aviation Materiel Laboratories, Fort Eustis, Virginia, October 1960.

14. Coronato, A. A., "Overhaul on Condition - Eliminate Time Between Overhaul", Sikorsky Aircraft, Division of United Aircraft Corporation, Stratford, Connecticut, AHS Seventeenth Annual National Forum, May 3-5, 1961, Washington, D.C.

15. Rodgers, S. J., "Evaluation of the Dust Cloud Generated by Helicopter Rotor Blade Downwash", USAAVLABS Technical Report 67-81, U. S. Army Aviation Materiel Laboratories, Fort Eustis, Virginia, March 1968.

16. Spreiter, J. R., and Sacks, A. H., "The Rolling Up of the Trailing Vortex Sheet and Its Effect on the Downwash Behind Wings", Aerodynamics Session, Eighteenth Annual Meeting, I.A.S., New York, January 23-26, 1950.

17. Bagnold, R. A., FRS, "The Physics of Blown Sand and Desert Dunes", Methuen and Company LTD, London, July 1953.

18. Kuhn, R. E., "An Investigation to Determine Conditions Under Which Downwash From VTOL Aircraft will Start Surface Erosion From Various Types of Terrains", NASA TND-56, September 1959.

19. Bartley, S. H., "The Psychophysiology of Vision",
Handbook of Experimental Psychology (edited by S. S.
Stevens), John Wiley and Sons, Inc., New York, Chapman
and Hall Ltd., London, 1951.

20. Watzen, E., "Amount of Dust Recirculated by a Hovering
Helicopter", Kaman Aircraft Corporation Report No.
R-169, Bloomfield, Connecticut, December 1956.

21. Pruyn, R. R., "Effects of Airframe Geometry on Downwash
Problems of Tandem Ducted - Propeller VTOL Aircraft",
Kellett Aircraft Corporation Report No. KAC 179T80-6,
Willow Grove, Pennsylvania, January 1964.

22. Curtis, N. C., Jr., "Downwash Tests of the Dual Tandem
Ducted Propeller VTOL Research Aircraft Configurations
to Evaluate Engine Inlets, Protection Devices and Study
Aerodynamic Interference", Kellett Aircraft Corporation
Report No. 179T80-12, Willow Grove, Pennsylvania,
November 1965.

23. Anon., "Unpublished Data on the Effects of Foreign
Object Ingestion on the Mission Endurance of the Vertol
Model 107 (CH-46A) Helicopter", Vertol Division of the
Boeing Company, Morton, Pennsylvania.

24. Connors, H. D., "Development of the Lycoming Internal
Particle Separator", Proceedings of the Seventh Annual
National Conference on Environmental Effects on Aircraft
and Propulsion Systems", Report No. 67-ENV-5, Princeton,
New Jersey, September 1967.

25. Bianchini, G. V., "Field Evaluation of an Air Cleaner for
the T63 Engine Powered OH-6A Aircraft", Proceedings of
the Seventh Annual National Conference on Environmental
Effects on Aircraft and Propulsion Systems, Report No.
67-ENV-6, Princeton, New Jersey, September 1967.

26. Stephenson, C. D., Shohet, H. H., and Speiden, E. F.,
"CH-54A and CH-53A Engine Air Particle Separator (EAPS)
Development", Proceedings of the Seventh Annual National
Conference on Environmental Effects on Aircraft and
Propulsion Systems, Report No. 67-ENV-7, Princeton,
New Jersey, September 1967.

27. Model Spec. No. 124.27 dated 15 February 1965 and
Amendment No. 2 dated 12 April 1967, Revised 1 June 1967,
entitled T55-L-11 Shaft Turbine Engine (Lycoming Model
LTC4B-11B), Lycoming Division, AVCO Corporation,
Stratford, Connecticut.

APPENDIX
SURFACE EROSION TEST DATA

In conjunction with the tests at Yuma conducted by MSA
Research Corporation (Reference 15), this contractor obtained
test data on the weight and size of particles entrained from
the ground and transported along the wall jet.

The dust particles were collected in specially designed
particle traps which were located in the vicinity of the H-21
helicopter hovering in ground proximity. The particle trap
layout used during the tests is shown in Figure 65. The
particle traps were made from 2-3/8-inch-inside-diameter
plastic tubing. The shape of the basic trap was a "T" lying
on its side. The leg of the "T" was the intake for the
contaminated air, and a cup was provided on the bottom for
collecting the dust sample. A wire mesh screen shaped into
a cone with a surface area five times the inlet area of the
trap was attached to the top of the trap. This was used as
a filter which collected the dust particles while permitting
the now clear air to flow out of the trap. The filter screen
was made from 200 mesh wire cloth with 33.6-percent open area.
The size of the screen openings was 0.0029 inch.

Six particle traps were mounted on a boom to a height of 10
feet, as shown in Figure 65. Two booms with a total of 12
traps were used for these tests. The location of the booms
was varied from the front to the side of the helicopter
depending on the sampling method selected for the particular
test.

During all tests, a target was placed in the pilot's view,
providing him with heading and distance information from the
first sampler location. The pilot approached the target
point, hovered at an altitude of approximately 1 foot wheel
clearance for a specified period of time, and quickly backed
away from the test area.

Data were obtained for a total of nine tests; four of these
tests were selected as providing the most reliable data. The
results for the remaining tests were questionable because of
the conditions encountered during testing; i.e., the

116
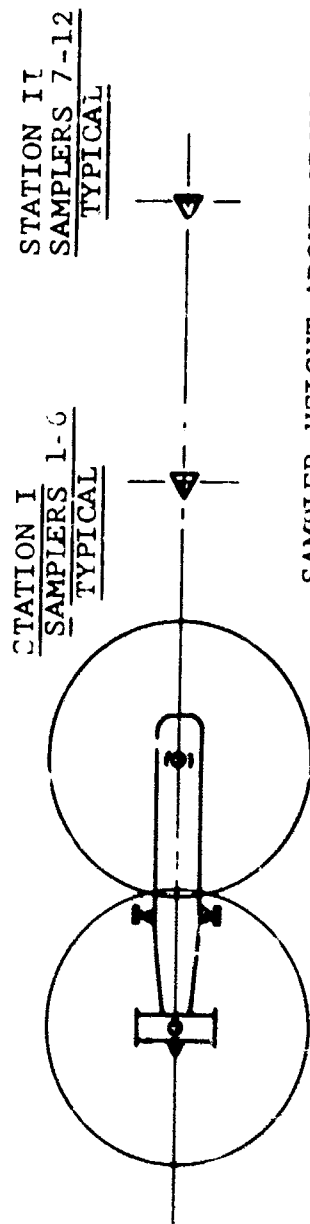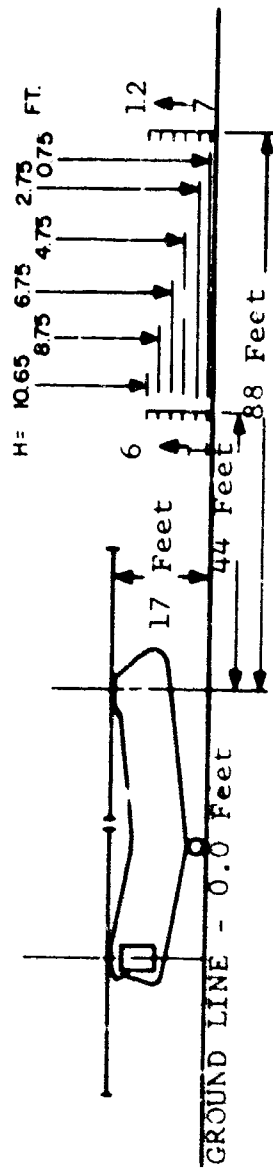
Figure 65. Particle Trap Layout.

TEST CONDITION II

STATION II

STATION I

88 Feet

44 Feet

21 Feet

17 Feet
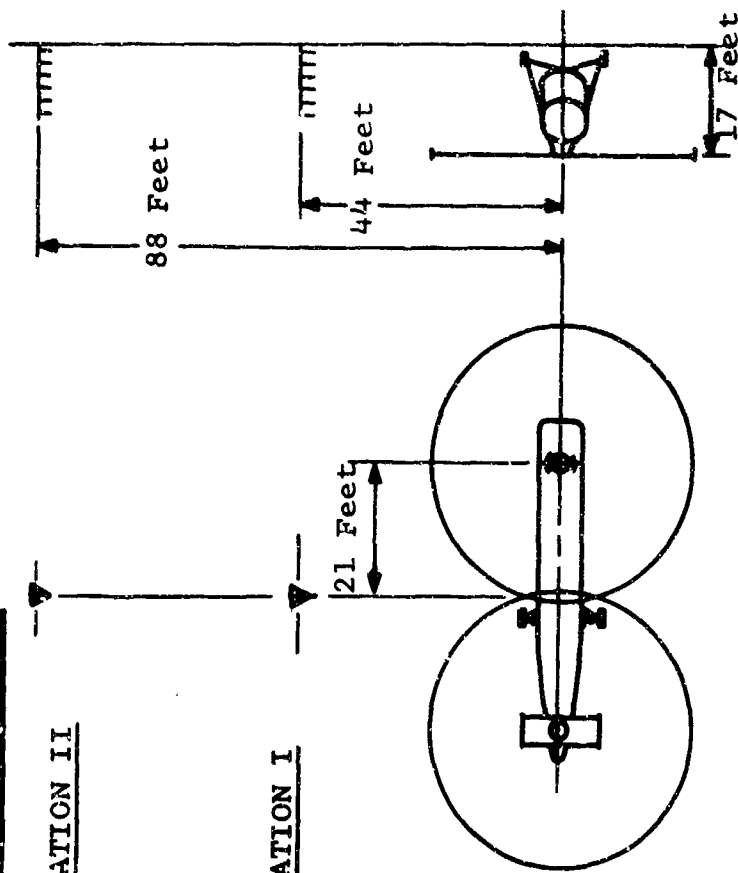
(b) Test Condition II

Figure 65. Continued.

118

excessive surface winds, the poor orientation of helicopter
with respect to the samplers, the undeterminable time of
operation of the helicopter in the vicinity of the samplers,
etc.

All samples collected were analyzed by the Vicksburg Water-
ways Experimental Station. The following information was
obtained:

1. Weight of particles.

2. Size distribution of particles for selected
   samplers.

3. Maximum size of particles found in each sample.

The test data for Test Condition I, Run No. 5 and Run No. 7
and for Test Condition II, Run No. 4 and Run No. 9 are
presented in Tables VI, VII, VIII, and IX, respectively.
These tables show particle mass flow rates measured along
longitudinal axis (Test Condition I) and lateral axis (Test
Condition II) of the H-21 helicopter. The collection of data
from both the front and side of the aircraft was performed to
determine any variations that might exist in surface erosion
due to the downwash interaction effects of the two rotors.

The results obtained from these tests at two radial stations
from the front and sides of the H-21 helicopter are
summarized in Figures 66 through 69.

The mass flow data are presented in Figures 66 and 67 for the
front and side of the helicopter, respectively. The flow
data are given in pounds of sand collected per second per
unit area and are plotted as a function of height above the
ground.

In Figure 66 the mass flow rate of particles measured along
the front of the H-21 helicopter, as expected, is seen to
decrease with increasing height above the ground. What is
unusual, however, is that with the exception of the region
very close to the ground, the flow rate increased with
increasing radial distance. This is contrary to data
obtained in Reference 13 for the 2-foot ducts. These data are

119

TABLE VI

GRADATION TEST RESULTS - TEST CONDITION I, RUN NO. 5

H-21 YUMA SAND AND DUST TESTS

Run No. 5   Time: 4.0 Minutes   Condition - I

Sample No.	Total Weight (grams)	Percent Finer by Weight (microns)								Maximum Particle Size
		1000	500	250	74	58	36	18	14.5	
1	1.520	98.7	87.9	41.9	4.9	3.0	1.1	0.6	0.4	2000
2	3.218									1700
3	3.349	9.2	94.8	66.1	9.3	4.5	1.2	0.7	0.5	1700
4	1.261									1300
5	0.559									750
6	0.321	100.0	99.0	86.7	18.9	10.2	4.6	2.2	1.9	750
7	1.901	99.4	95.0	63.5	10.5	5.7	2.7	1.6	1.2	1700
8	4.297									1700
9	9.391	99.7	98.3	78.4	11.9	7.8	2.8	1.4	0.9	1300
10	5.634									750
11	2.958									750
12	1.653	100.0	93.5	92.1	18.9	5.3	2.1	1.4	1.0	750

TABLE VII

GRADATION TEST RESULTS - TEST CONDITION I, RUN NO. 7

H-21 YUMA SAND AND DUST TESTS

Run No. 7   Time: 2 Minutes   Condition - I

Sample No.	Total Weight (grams)	Percent Finer by Weight (microns)								Maximum Particle Size
		1000	500	250	74	58	36	18	14.5	
1	37.518	99.6	95.5	62.4	5.0	2.0	1.0	1.0	0.8	2000
2	1.291									1100
3	0.750	100.0	99.7	88.3	14.1	7.6	1.8	1.4	0.5	750
4	0.540									750
5	0.341									375
6		100.0	100.0	95.1	28.8	15.5	5.0	3.5	2.4	375
7	31.489	99.6	97.8	76.8	12.4	4.2	3.1	2.1	1.2	2000
8	9.545									1300
9	4.311	100.0	99.2	85.2	8.6	5.3	3.3	1.8	1.2	750
10	1.975									750
11	0.892									750
12	0.448	100.0	100.0	95.6	22.9	8.5	3.8	3.6	3.0	375

TABLE VIII

GRADATION TEST RESULTS - TEST CONDITION II, RUN NO. 4

H-21 YUMA SAND AND DUST TESTS

Run No. 4   Time: 5 Minutes   Condition - II

Sample No.	Total Weight (grams)	Percent Finer by Weight (microns)								Maximum Particle Size
		1000	500	250	74	58	36	18	14.5	
1	89.895	99.6	96.4	67.7	8.1	3.9	1.9	1.2	0.8	2000
2	8.132									1100
3	2.339	100.0	98.0	76.2	12.4	6.4	3.6	1.2	1.0	750
4	1.070									750
5	0.572									750
6	0.339	100.0	99.5	93.3	25.3	16.7	3.8	2.3	1.7	1300
7	163.701	99.7	95.5	61.9	12.6	6.7	4.0	1.9	1.4	750
8	18.619									2000
9	9.009	99.8	97.9	74.7	10.0	6.0	2.2	1.1	0.7	2000
10	-									1300
11	2.003									750
12	1.130	100.0	99.1	84.2	18.4	10.6	5.7	3.8	2.8	750

TABLE IX

GRADATION TEST RESULTS - TEST CONDITION II, RUN NO. 9

H-21 YUMA SAND AND DUST TESTS

Run No. 9   Time: 2 Minutes   Condition - II

| Sample No.	Total Weight (grams)	Percent Finer by Weight (microns)								Maximum Particle Size
		1000	500	250	74	58	36	18	14.5	
1	77.992	99.1	90.1	49.2	4.7	2.9	1.6	0.8	0.6	2000
2	6.215									1700
3	1.225	99.1	94.0	62.8	9.7	6.0	2.1	1.2	0.8	1100
4	0.403									750
5	0.255									750
6	0.180	100.0	99.3	81.8	28.6	16.6	6.2	3.1	2.3	750
7	68.189	99.3	95.2	65.6	14.6	5.4	4.7	4.1	3.4	2000
8	12.880									2000
9	7.109	99.8	96.2	68.2	6.6	8.5	1.5	0.9	0.6	1700
10	2.429									1700
11	1.791									750
12	0.979	100.0	99.5	75.5	14.1	8.2	3.6	1.9	1.4	750
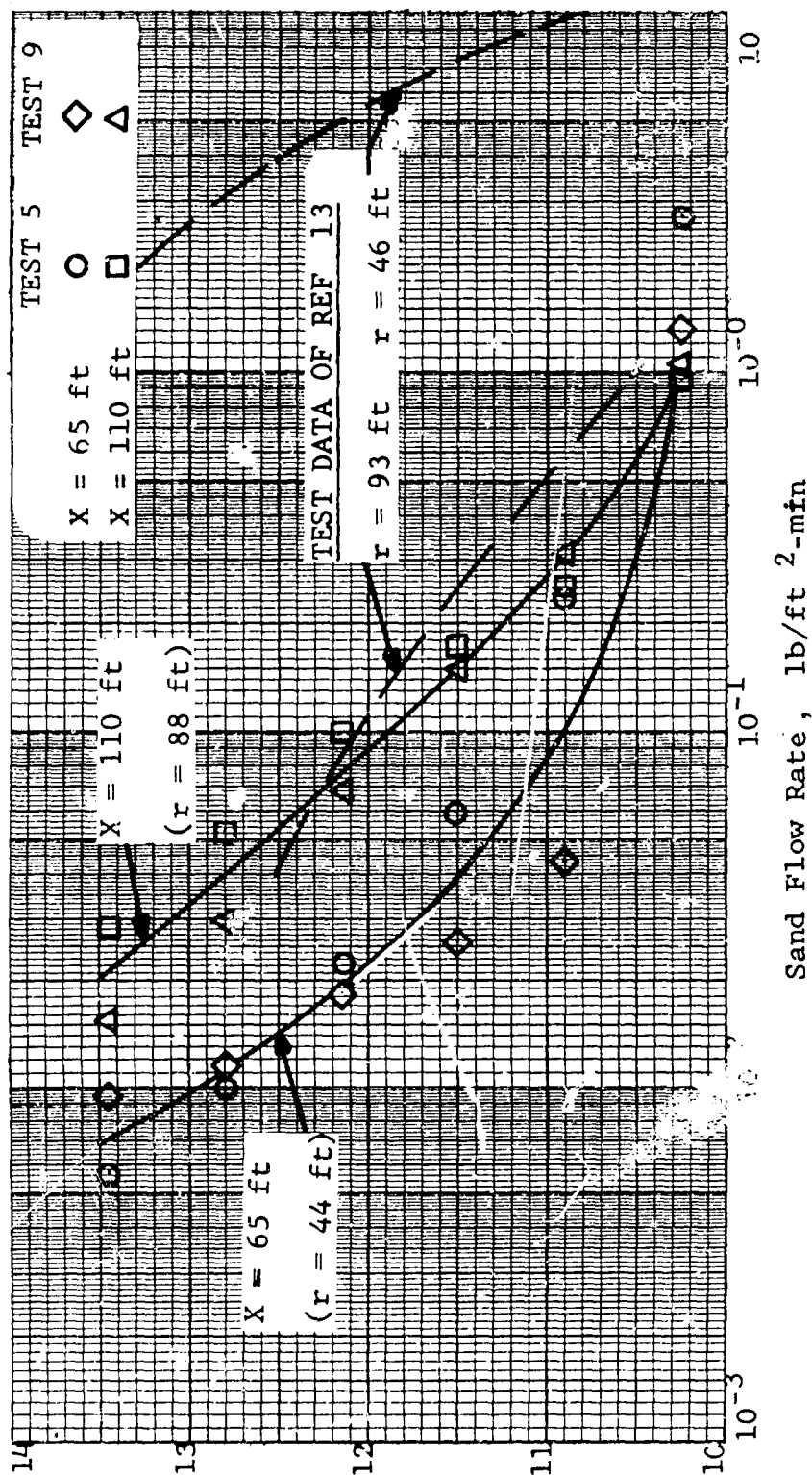
Figure 66. Mass Erosion Rates of Particles Entrained Forward of the H-21 Helicopter, Test Condition I - Phillips Drop Zone, H = 17 Feet.
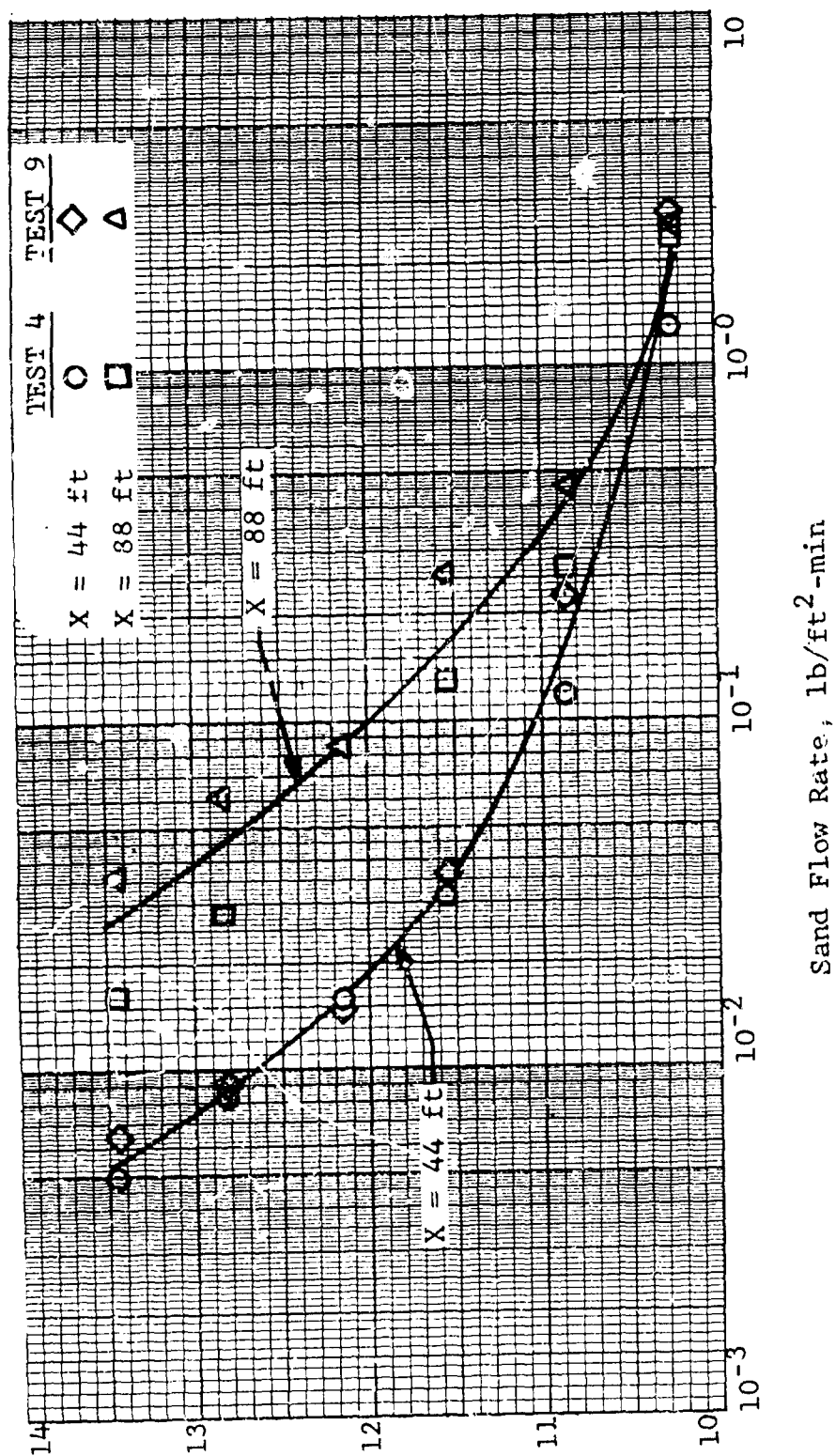
124

Figure 67. Mass Erosion Rates of Particles Entrained Outboard of the H-21 Helicopter, Test Condition II - Phillips Drop Zone, H = 17 Feet.
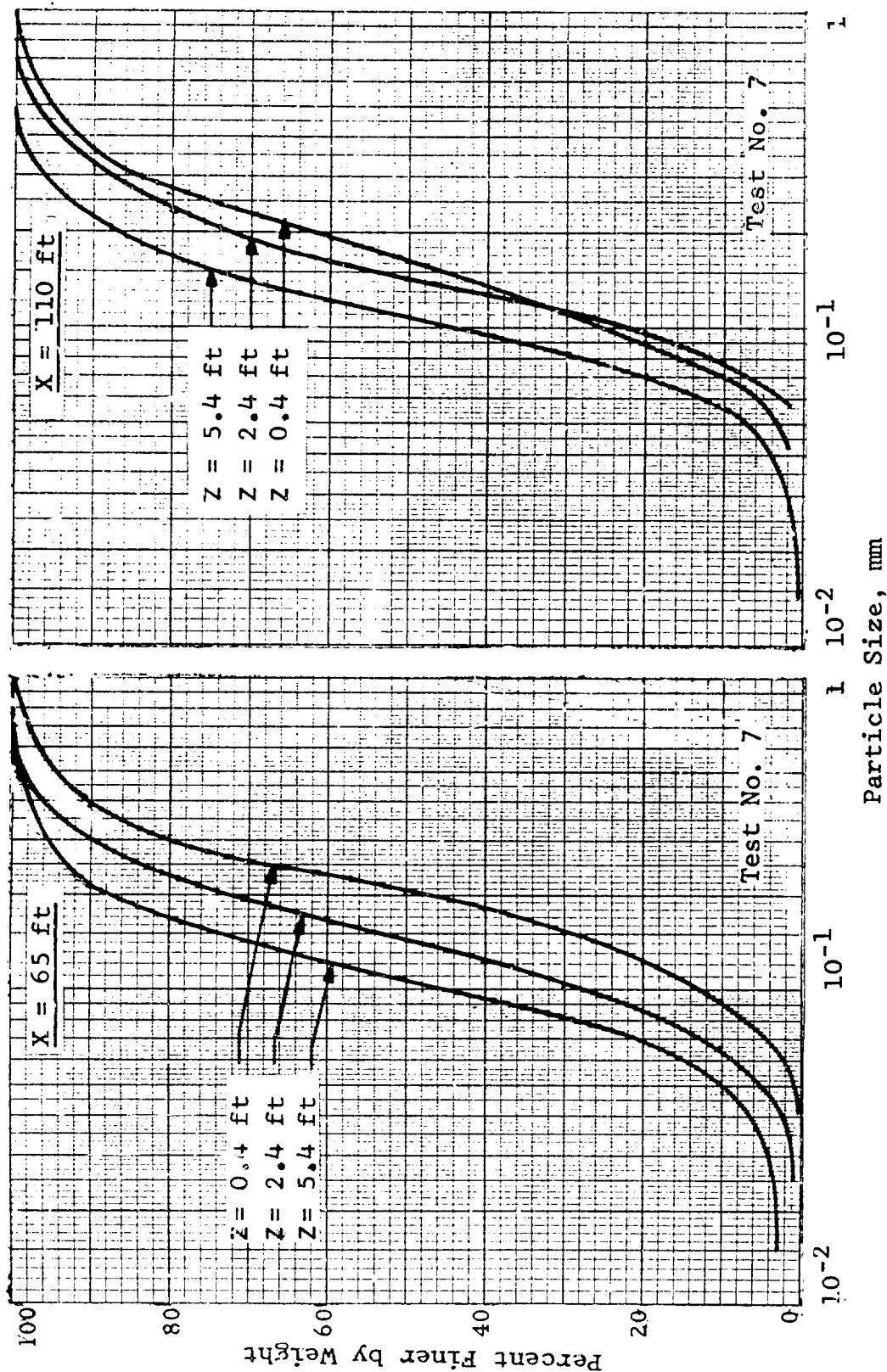
125

Figure 68. Particle Size Distribution Forward of the H-21 Helicopter, Test Condition I – Phillips Drop Zone, H = 17 Feet.
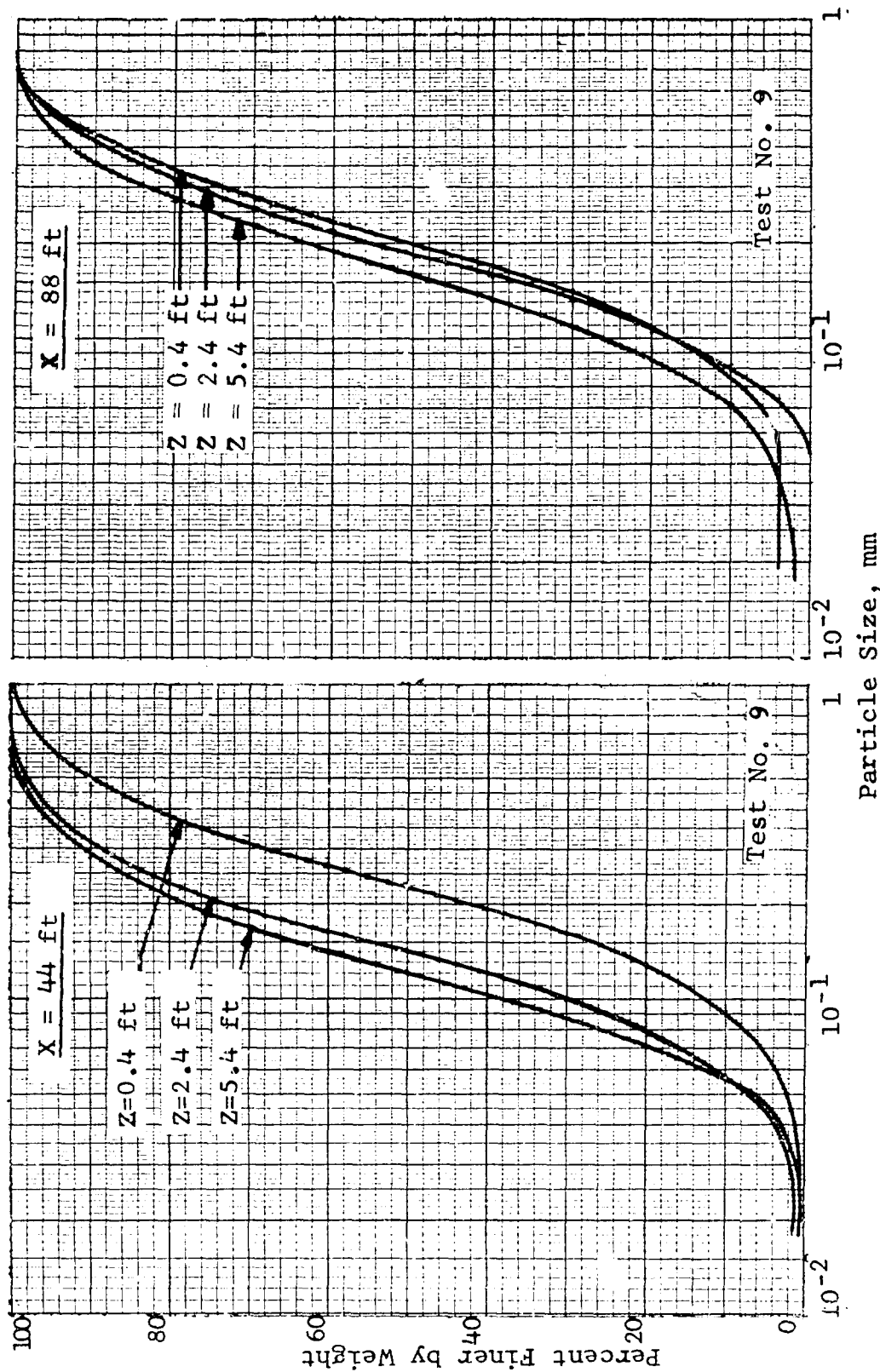
Figure 69. Particle Size Distribution Outboard of the H-21
Helicopter, Test Condition II - Phillips Drop Zone,
H = 17 Feet.

127

superimposed on Figure 66 for comparison. The observation
of the sand flow along the ground as reported by the pilot
confirms the results obtained during this program. According
to the pilot's observations, the entrained sand started to
erode just in front of the first row of samplers and billowed
upward to engulf the aft row of samplers completely. As a
result of this flow mechanism, a majority of the sand
particles were trapped very close to the ground by the first
row of samplers and at higher locations from the ground by
the second row. More data are required to define the point
where the cross-over of flow rate will occur.

The flow rates along the side of the helicopter were obtained
along a plane midway between the two rotors perpendicular to
the longitudinal axis of the aircraft (interaction plane).
These data are presented in Figure 67 as a function of height
above the ground for two radial stations. The flow rates as
shown in this figure are very similar to the data obtained
along the front of the aircraft both in magnitude and varia-
tion with height. It appears that the amount of eroded
particles does not significantly change due to the interaction
of the two rotors even though the particles are transported
further out radially.

The size distribution of particles collected in the samplers
has been obtained for the same test conditions as those
described previously. The results are presented in Figures
68 and 69 for the front and side of the helicopter, respec-
tively. From these figures, it can be seen that the particle
size reduces with an increase in both height above ground and
radial location.

128

DOCUMENT CONTROL DATA - R & D

(Security classification of title, body of abstract and indexing annotation must be entered when the overall report is classified)

1. ORIGINATING ACTIVITY (Corporate author)	2a. REPORT SECURITY CLASSIFICATION
Dynasciences Corporation Blue Bell, Pennsylvania 19422	Unclassified 2b. GROUP

3. REPORT TITLE

INVESTIGATION OF THE DOWNWASH ENVIRONMENT GENERATED BY V/STOL AIRCRAFT OPERATING IN GROUND EFFECT

4. DESCRIPTIVE NOTES (Type of report and inclusive dates)

Final Report

5. AUTHOR(S) (First name, middle initial, last name)

M. George
E. Kisielowski
D. S. Douglas

6. REPORT DATE	7a. TOTAL NO. OF PAGES	7b. NO. OF REFS
July 1968	149	27

8a. CONTRACT OR GRANT NO. DA 44-177-AMC-316(T) b. PROJECT NO. 1T021701A047 c. d.	9a. ORIGINATOR'S REPORT NUMBER(S) USAAVLABS Technical Report 68-52 9b. OTHER REPORT NO(S) (Any other numbers that may be assigned this report) Dynasciences Report No. DCR-275

10. DISTRIBUTION STATEMENT

This document has been approved for public release and sale;
its distribution is unlimited.

11. SUPPLEMENTARY NOTES	12. SPONSORING MILITARY ACTIVITY
	U. S. Army Aviation Materiel Laboratories, Ft. Eustis, Virginia

13. ABSTRACT

Analytical methods are developed for determining the downwash environment generated by multirotor/propeller V/STOL aircraft configurations operating in ground proximity.

These methods are utilized to compute rotor flow field and contaminant dust cloud characteristics (including particle density and size distributions) for the H-21, XC-142, X-22A, X-19A, and XV-5A aircraft. The effects of the contaminated atmosphere on pilot's visibility, ground equipment, and personnel are also determined for these aircraft.

The theoretically predicted results are generally in good agreement with the limited test data. Additional full-scale test data are required to verify further the assumptions inherent in the theory.

DD FORM 1473 REPLACES DD FORM 1473, 1 JAN 64, WHICH IS OBSOLETE FOR ARMY USE.

Unclassified
Security Classification

Unclass.fied

Security Classification

14. KEY WORDS	LINK A		LINK B		LINK C	
	ROLE	WT	ROLE	WT	ROLE	WT
Rotor Downwash						
Mass Flow Rate						
Particle Density						
Disc Loading						
Cloud Content						

Unclassified

Security Classification